A microbiota-modulated checkpoint directs immunosuppressive intestinal T cells into cancers

Marine Fidelle, Conrad Rauber, Carolina Alves Costa Silva, Ai-Ling Tian, Imran Lahmar, Anne-Laure Mallard de la Varende, Liwei Zhao, Cassandra Thélémaque, Isabelle Lebhar, Meriem Messaoudene, et al.

Microbiota -modulated checkpoint directs immunosuppressive intestinal T cells into cancer

Marine Fidelle[1,2,3]†, Conrad Rauber[1,2,3,4]*†, Carolina Alves Costa Silva[1,2,3]†, Ai-Ling Tian[1,2,5,6], Imran Lahmar[1,2,3], Anne-Laure Mallard de La Varende[1,2,3], Liwei Zhao[1,5,6], Cassandra Thélémaque[1,3], Isabelle Lebhar[1,3], Meriem Messaoudene[7], Eugenie Pizzato[1,3], Roxanne Birebent[1,2,3], Maxime Descartes Mbogning Fonkou[1,3], Silvia Zoppi[1,2,8], Anna Reni[1,2,9], Cécile Dalban[10], Marion Leduc[1,5,6], Gladys Ferrere[1,3,11], Sylvère Durand[1,5,6], Pierre Ly[1,3,12], Aymeric Silvin[1,3], Kevin Mulder[1,2,3], Charles-Antoine Dutertre[1,3], Florent Ginhoux[1,3], Satoru Yonekura[1,2,3], Maria Paula Roberti[1,3,13,14], Maryam Tidjani-Alou[1,3], Safae Terrisse[1,2,3], Jianzhou Chen[1,3], Oliver Kepp[1,5,6], Angela Schippers[15], Norbert Wagner[15], Javier Suárez Gosálvez[16], Sebastian Kobold[16,17], Jean-Eudes Fahrner[1,2,3], Corentin Richard[7], Jacques Bosq[18], Leonardo Lordello de Melo[1,3], Giacomo Vitali[19], Nathalie Galleron[19], Benoît Quinquis[19], Emmanuelle Le Chatelier[19], Lucas Blanchard[20], Jean-Philippe Girard[20], Anne Jarry[21], Nadine Gervois[21], Emmanuelle Godefroy[21], Nathalie Labarrière[21,22], Ronald Koschny[4], Romain Daillère[11], Benjamin Besse[1,2], Caroline Truntzer[23], François Ghiringhelli[23], Nicolas Coatnoan[24,25], Vanessa Mhanna[24,25], David Klatzmann[24,25], Damien Drubay[1,26,27], Laurence Albiges[1,2], Andrew Maltez Thomas[28], Nicola Segata[28,29], François-Xavier Danlos[1,2,3,12,30], Aurélien Marabelle[1,2,3,12,30], Bertrand Routy[7,31], Lisa Derosa[1,2,3,12]†, Guido Kroemer[5,6,32]*†, Laurence Zitvogel[1,2,3,12]*†

Affiliations:

[1]Gustave Roussy Cancer Campus, Villejuif Cedex, France
[2]Université Paris-Saclay, Faculté de Médecine, Le Kremlin-Bicêtre, France
[3]Institut National de la Santé Et de la Recherche Médicale (INSERM) U1015, Équipe Labellisée - Ligue Nationale contre le Cancer, Villejuif, France
[4]Department of Gastroenterology and Infectious Diseases, University Hospital Heidelberg, Heidelberg, Germany
[5]Centre de Recherche des Cordeliers, INSERM U1138, Équipe Labellisée - Ligue Nationale contre le Cancer, Université Paris Cité, Sorbonne Université, Paris, France.
[6]Metabolomics and Cell Biology Platforms, Gustave Roussy Cancer Campus, Villejuif, France.
[7]Centre de Recherche du Centre Hospitalier de l'Université de Montréal (CRCHUM), Montréal, QC, Canada
[8]Department of Medicine and Surgery, University of Parma, Parma, Italy.
[9]Section of Oncology, Department of Medicine, University of Verona School of Medicine and Verona University Hospital Trust, Verona, Italy
[10]Clinical Research Department, Centre Léon Bérard, Lyon, France
[11]EverImmune, Gustave Roussy Cancer Campus, Villejuif Cedex, France
[12] Center of Clinical Investigations in Biotherapies of Cancer (BIOTHERIS), Villejuif, France
[13]Clinical Cooperation Unit Applied Tumor Immunity, German Cancer Research Center (DKFZ), Heidelberg, Germany
[14]Department of Medical Oncology, National Center for Tumor Diseases (NCT), Heidelberg University Hospital (UKHD), Heidelberg, Germany
[15]Department of Pediatrics, University Hospital RWTH Aachen, Aachen, Germany
[16]Center of Integrated Protein Science Munich (CIPS-M) and Division of Clinical Pharmacology, Department of Medicine IV, Klinikum der Universität München, LMU Munich, Germany

[17]German Cancer Consortium (DKTK), partner site Munich, Munich, Germany
[18]JBO Consultant, Paris, France
[19]MetaGenoPolis, INRAe, Université Paris-Saclay, Jouy en Josas, France
[20]Institut de Pharmacologie et de Biologie Structurale, IPBS, Université de Toulouse, CNRS, UPS, Toulouse, France
[21]Nantes Université, Université d'Angers, INSERM, CNRS, Immunology and New Concepts in ImmunoTherapy, INCIT, UMR 1302/EMR6001, Nantes, France
[22]LabEx IGO, Université de Nantes, Nantes, France
[23]Université de Bourgogne Franche-Comté, Plateforme de Transfert de Biologie du Cancer, Centre Georges-François Leclerc, Equipe Labellisée Ligue Nationale Contre le Cancer, Centre de Recherche INSERM LNC-UMR1231, Institut Médical de Génétique et d'Immunologie, Dijon, France
[24]AP-HP, Hôpital Pitié-Salpêtrière, Clinical Investigation Center for Biotherapies (CIC-BTi) and Immunology-Inflammation-Infectiology and Dermatology Department (3iD), Paris, France.
[25]Sorbonne Université, INSERM, UMRS959 Immunology-Immunopathology-Immunotherapy Laboratory, Paris, France
[26]Gustave Roussy, Office of Biostatistics and Epidemiology, Université Paris-Saclay, Villejuif, France
[27]Inserm, Université Paris-Saclay, CESP U1018, Oncostat, labeled Ligue Contre le Cancer, Villejuif, France
[28]Department of Computational, Cellular and Integrative Biology, University of Trento, Trento, Italy
[29]Istituto Europeo di Oncologia (IEO), National Cancer Institute (IRCCS), Milan, Italy
[30]Drug Development Department, Gustave Roussy Cancer Campus, Villejuif Cedex, France

[31]Hematology-Oncology Division, Department of Medicine, Centre Hospitalier de l'Université de Montréal (CHUM), Montréal, QC, Canada
[32]Institut du Cancer Paris CARPEM, Department of Biology, Hôpital Européen Georges Pompidou, Assistance Publique – Hôpitaux de Paris (AP-HP), Paris, France

*Corresponding author. E-mail: laurence.zitvogel@gustaveroussy.fr (L.Zi.); kroemer@orange.fr (G.K); conrad.rauber@gmx.de (C.Ra.)
†These authors contributed equally to this work.

Abstract:
Antibiotics (ABX) compromise the efficacy of PD-1 blockade in cancer patients, but the mechanisms underlying their immunosuppressive effects remain unknown. By inducing the downregulation of mucosal addressin cell adhesion molecule-1 (MAdCAM-1) in the ileum, post-ABX gut recolonization by species from the genus *Enterocloster* provoked the emigration of enterotropic $\alpha4\beta7^{+}CD4^{+}$ T regulatory 17 (Tr17) cells to the tumor. These ABX effects were mimicked by oral gavage of *Enterocloster* spp., genetic deficiency of MAdCAM-1 and its receptor α4β7 integrin, or their antibody-mediated neutralization, while fecal microbiota transplantation or IL-17A neutralization prevented them. In independent cohorts of lung, kidney and bladder cancer patients, low serum levels of soluble MAdCAM-1 had a negative prognostic impact. Thus, the MAdCAM-1–α4β7 axis constitutes an actionable gut immune checkpoint in cancer immunosurveillance.

Immune checkpoint inhibitors (ICIs) targeting the immunosuppressive interaction between programmed cell death protein 1 (PD-1) and programmed death-ligand 1 (PD-L1) are used in the clinical management of many cancer types (*1*, *2*). Primary resistance to ICIs has been attributed to various molecular or cellular cues (*3*–*5*). In addition, several studies confirmed the deleterious effect of antibiotics (ABX) on clinical benefit in patients receiving ICIs (*6*–*8*). Meta-analyses have revealed that ABX uptake is more harmful on clinical outcome when administered prior to, rather than during ICI administration, suggesting that bacterial recolonization following an ABX course may be particularly deleterious (*9*–*11*). How these new bacterial compositions interfere with the reprograming of the tumor microenvironment (TME) remains a conundrum.

The α4 (CD49d) and β7 integrin subunits interact to form the α4β7 heterodimer. By interacting with its counter-receptor mucosal addressin cell adhesion molecule 1 (MAdCAM-1), α4β7 integrin mediates lymphocyte adhesion and diapedesis from the circulation across the vascular endothelial barrier into gut-associated secondary lymphoid tissue (GALT) or lamina propria (LP). MAdCAM-1 is constitutively expressed in LP venules, as well as in GALT high endothelial venules (HEV), and upregulated by inflammatory cytokines (*12*–*14*). By preventing the migration of inflammatory $\beta7^+$ T cells from the circulation to the gut, antibodies (Abs) targeting α4β7 or MAdCAM-1 reduce the severity of colitis in patients with inflammatory bowel disease (IBD) (*15*–*17*).

Intestinal microbiota plays a role in maintaining the homeostatic functions of gut regulatory T (Treg) and IL-17–producing T helper 17 (Th17) cells (*18*, *19*). Gut Th17 cells also control extraintestinal inflammation (*20*–*24*). Th17 cells and a lineage-related $FoxP3^+ROR\gamma t^+$ regulatory subset (Tr17 cells) blunt antitumor immunosurveillance during carcinogenesis (*25*). In humans and mice, the expression of the transcription factor RORγt is characteristic of a subpopulation of tumor-infiltrating Treg cells that are induced by gut commensals (*26*–*28*). Thus, we hypothesized that ABX-induced overgrowth of selected species (*11*, *29*) might affect the trafficking of Treg cells between the intestinal and tumoral compartments, thereby aggravating cancer immunosuppression and resistance to PD-1 blockade.

ABX downregulate MAdCAM-1 ileal expression in mice and patients

The use of a cocktail of broad-spectrum ABX (ampicillin, colistin, and streptomycin (ACS)) to sterilize the gastrointestinal tracts of mice attenuates the anticancer effects of PD-1 blockade (*7*). ACS reduced the expression of most ileal chemokines and *Madcam1* (**Fig. 1A and**

fig. S1A). These effects were specific for the ileum because they were not observed in the colon or in MCA205 fibrosarcomas (**Fig. 1A and fig. S1A**). Ileal *Madcam1* mRNA and protein levels were decreased as determined by RT-qPCR (**Fig. 1A**), immunohistochemistry (**Fig. 1B**), flow cytometry of ileal $CD45^-$ LP cells (**Fig. 1C and fig. S1B**), and ELISA of ileal tissue lysates (**Fig. 1D**). The integrity of the intestinal architecture and vasculature was notably preserved following ACS administration, without any alteration in the density of $CD31^+$ capillaries (**fig. S1C**). Levels of MAdCAM-1 began to decrease on day 3 of ACS administration and did not recover on day 4 (ACS+4d) or even on day 12 post-ACS cessation (**Fig. 1, C and D**). The ACS cocktail also downregulated *Madcam1* gene expression in Peyer's patches (PP) and in mesenteric lymph nodes (mLNs) (**fig. S1, D and E**). Other ABX regimens using β-lactams (ceftazidime and cefepime cephalosporins), aminoglycosides (streptomycin), polymyxins (colistin), and macrolides (erythromycin) also downregulated ileal *Madcam1* (**fig. S1, E and F**). By contrast, piperacillin plus tazobactam, rifaximin, and vancomycin had no effect on *Madcam1* expression in two distinct animal facilities located in France (**fig. S1E**) and Canada (**fig. S1F**). *Madcam1* (but not vascular cell adhesion protein (*Vcam1*)) mRNA levels were 10 times lower in tumor-draining LNs (tdLNs) than in mLNs (**fig. S1G**). Mass spectrometry of ileal bacteria cultured from animals treated with various ABX regimens under aerobic and anaerobic conditions identified several species (spp.) belonging to the genus *Enterocloster* (such as *Enterocloster clostridioformis* and *Enterocloster bolteae*) (*29*) that prevailed 4 or 7 days after ACS or erythromycin cessation but not in any other experimental condition (**table S1**). These *Enterocloster* spp. were previously identified in the stools of cancer patients resistant to PD-1 blockade (*10*, *11*), as well as in chronic inflammatory disorders (*30*), and mediate resistance to cancer immunotherapy with PD-1 blockade in mice (*31*). Whereas oral gavage of *E. clostridioformis* reduced ileal *Madcam1* mRNA (**Fig. 1E**), administration of immunostimulatory *Akkermansia* strain p2261 (*Akk.*) (*7*, *10*) or *Enterococcus hirae* (*32*) increased basal *Madcam1* expression in ileal tissues from eubiotic mice reared in specific-pathogen-free (SPF) conditions (**Fig. 1E**). Moreover, ACS-induced downregulation of ileal *Madcam1* mRNA correlated with a decrease in regulatory cytokines and transcription factors (e.g., *Foxp3*, *Il17a*, *Il22*, and *Rorc*) (**fig. S1, A, H, and I**). In accordance with this, ACS depleted mucosal Treg cells and Th17 cells from the ileal LP (**Fig. 1F and fig. S2A**). Finally, ACS phenocopied the ileal immunomodulatory effects of *Madcam1* knockout or antibody neutralization of MAdCAM-1 (**Fig. 1G**).

We confirmed the coordinated inhibitory effects of several class of ABX on the ileal (but not cecal nor colonic) expression of *MADCAM1* and *RORC* in 31 patients who were treated with ABX (n=10) compared with non-treated patients (n=21) while they underwent intestinal endoscopy and biopsies for various indications (**Fig. 2, A and B, and table S2**). As in mice, we found a correlation between *MADCAM1* and *IL17A* ileal mRNA levels (**Fig. 2C**). In clinical trials, fecal microbial transfer (FMT) from melanoma patients who benefited from PD-1 blockade circumvents primary resistance to ICIs in one third of metastatic melanoma recipients (*33*, *34*). Moreover, FMT from some human donors fails to improve ICIs responses (*7*, *35*). We tested whether random FMT from NSCLC patients to ABX-preconditioned mice would modulate ileal *Madcam1* gene expression. Three out of six FMTs downregulated *Madcam1* mRNA (**Fig. 2D and table S3**). Shotgun metagenomics-based analyses of these three human stools revealed an overrepresentation of *Enterocloster* spp., including *E. clostridioformis* as well as that of *Hungatella hathewayi*, which is phylogenetically close to *Enterocloster* spp. (*29*), in two out of three of these stools compared with the three other human fecal samples (**Fig. 2D**). Mice orally gavaged with stools that downregulated *Madcam1* expression exhibited a relative over-representation of *E. clostridioformis* (**Fig. 2D**). Finally, the longitudinal follow up of cancer patients more than 60 days post-ABX cessation revealed significant decreases of the abundance of *Enterocloster* and *Hungatella* spp. (**Fig. 2E**).

Thus, broad-spectrum ABX downregulate the expression of the ileal mucosal addressin MAdCAM-1, correlating with reduced ileal *Foxp3*, *Il17a*, and *Rorc*.

To further elucidate potential molecular cues explaining MAdCAM-1 loss following relative dominance of ileal *E. clostridioformis*, we performed mass spectrometric metabolomics of murine ileal contents 7 days post-gavage with this bacterium. There were significant changes in biliary acid (BA) levels (**fig. S3A**), in accordance with a previous report (*36*). We screened the effects of various BA (*37*, *38*) and bacteria on *Madcam1* expression in vitro using two murine endothelial cell lines (TSEC and bEnd.3) engineered to express green fluorescent protein (GFP) under the control of the *Madcam1* promoter (**fig. S3B**). Live *E. clostridioformis* directly reduced expression of GFP, whereas the immunogenic *Akk.* failed to do so (**fig. S3C**). Lithocholic acid (LCA) as well as two synthetic farnesoid X receptor (FXR) agonists significantly decreased GFP expression in TSEC and bEnd.3 exposed to IL-1β+TNF-α in a dose-dependent manner (**fig. S3D**). Distinct LCA isoforms reduced GFP expression levels at different dose levels (**fig. S3E**). RT-qPCR confirmed that LCA downregulated *Madcam1* mRNA expression levels in TSEC cells (**fig.**

S3F). Moreover, LCA (**fig. S3, G and H**) as well as UDCA (**fig. S3I**) dampened *Madcam1* gene expression levels in ileum and ileal PPs as well as in mLNs in vivo, in line with a prior report (*39*). Thus, one of the mechanisms by which *Enterocloster* spp. may downregulate MAdCAM-1 in GALT is via the accumulation of distinct BAs.

ABX induces the exodus of enterotropic α4β7$^+$ CD4$^+$ T cell subsets to tumor-draining lymph nodes

We hypothesized that the loss of ileal MAdCAM-1 might affect the trafficking of enterotropic T cells expressing the MAdCAM-1 receptor α4β7. We took advantage of Kaede mice, which express a fluorescent protein (*40*) that is photoconverted (PC) upon ultraviolet light (UV) illumination to study the exodus of intestinal cells (*20*, *22*, *23*). To track the fate of ileal, cecal, and mLNs cells (henceforth referred to as "intestine") 24 hours after photoconversion of tumor bearers, we analyzed PC leukocytes in various organs by flow cytometry (**fig. S4A**). Up to 22.8±2.6% of mLNs cells remained PC$^+$ and PC$^+$ cells became detectable in the spleen (5.1±0.5%) and tdLNs (4.0±0.3%) (**fig. S4A**). UV illumination of the ileum also enabled the visualization of gut leukocyte emigration to tdLNs or tumors, albeit to a lower extent than intestine illumination (**fig. S4B**). As a second method of cell tracking, we directly injected carboxyfluorescein succinimidyl ester (CFSE) into the mLNs (*41*) and then followed the emigration of CFSE-labeled cells to distant sites at 24 hours (**fig. S4C**). Up to 1.0±0.2% splenocytes, 0.8±0.1% tdLNs cells, and 0.2±0.02% of tumor-infiltrating leukocytes were replaced by mLNs-derived leukocytes (**fig. S4C**). Both methods revealed the selective enrichment of PC$^+$ or CFSE$^+$ α4β7$^+$ CD4$^+$ T cells in the spleen, tdLNs, and tumor at 24 hours (**Fig. 3, A and B, and fig. S4, D and E**). Ab-mediated inhibition of MAdCAM-1 in mice led to a more pronounced migration of PC$^+$ or CSFE-labeled cells from the mLNs to the tdLNs than in control animals (**fig. S4, F and G**). By contrast, the migration of mLNs cells to the contralateral LN (cLNs) was not affected (**fig. S4G**).

Bulk-RNA sequencing (RNA-Seq) of α4β7^{hi} CD4$^+$ T cells compared with α4β7$^-$ CD4$^+$ T cells purified from mLNs of tumor-bearing mice revealed that α4β7^{hi} CD4$^+$ T cells overexpressed not only the *Itga4* subunit of α4β7 but also genes involved in Treg cell functions and Th17 cell polarization. These cells downregulated *Tnfrsf9* however (**Fig. 3C and Data S1**).

We investigated how ACS-induced dysbiosis affected the exodus of CSFE-labeled mLNs cells to tdLNs (**Fig. 3D**). Transient ACS treatment for 14 days, followed by discontinuation of ACS for 4 days facilitated the mLNs to tdLNs migration of α4β7$^+$ Tr17 cells but not that of IL-

17A$^+$ α4β7$^+$ FoxP3$^-$ CD4$^+$ conventional T (Tconv) cells or α4β7$^-$ Treg cells (**Fig. 3E, fig. S5A**). ACS did not in fact increase the bona fide Treg cell pool of the tdLNs constituted by the locally expanded (extraintestinal, CFSE$^-$) cells (**fig. S5B**). Tr17 cells, which represent up to 40% of intestinal Treg cells, constituted the most mobile α4β7$^+$ CFSE$^+$ fraction, accounting for 0.2±0.1% of all CSFE$^+$ CD4$^+$ cells reaching the tdLNs 24 hours after injection of CSFE into mLNs, after cessation of ACS (**fig. S5B**). These originally enterotropic Tr17 cells did not only produce IL-17A but also IL-22 (**fig. S5B**). *Madcam1*$^{-/-}$ mice also manifested a similar mLNs to tdLNs (but not cLNs) migration of CFSE-labeled Treg cells (**Fig. 3F and fig. S5C**). Similarly, in Kaede-transgenic mice subjected to UV illumination of the intestine (**fig. S4A**), a neutralizing anti-MAdCAM-1 Ab promoted the gut to tdLNs migration of PC$^+$ CD25^{hi} α4β7$^+$ CD4$^+$ T cells (**Fig. 3G**). Since recolonization post-ACS is accompanied by the emergence of *Enterocloster* spp. (**table S1**) that downregulated ileal *Madcam1* (**Fig. 1E**), we determined whether oral gavage with *E. clostridioformis* would be sufficient to trigger this mLNs to tdLNs migration. Indeed, this bacterium facilitated the selective intestinal translocation of PC$^+$ (but not PC$^-$) CD25^{hi} (but not CD25$^-$) Th17 cells (CCR6$^+$CXCR3$^-$) (**Fig. 3H**). These findings suggest that the migrating enterotropic T cells do not use MAdCAM-1–expressing HEV to enter distal tissues. Instead, we observed a role for L/P-selectins in T cell homing to tumor beds during MAdCAM-1 downregulation (**fig. S6**), as previously described (*42*, *43*).

We next performed Rhapsody-based single-cell RNA-Seq of CFSE$^+$ CD4$^+$ T cells recovered from tdLNs at 24 hours post-CFSE injection into mLNs in mice treated with ACS and oral *E. clostridioformis* (**fig. S7, A and B**). Unsupervised clustering of the CFSE$^+$ CD4$^+$ T cells from tdLNs partitioned the data into four cellular clusters (**fig. S7C and Data S2**) (*44*). A small cluster featured the prototypic effector Treg cell phenotype (*26*) (**fig. S7D**). This Treg cell subset overexpressed genes (*Nrp1*, *Cd39*, and *Cd73*) involved in tumor immunosuppression (**fig. S7D**) and differed from all the other emigrating cells by the overexpression of genes associated with the Tr17 cell program (*26*) (**fig. S7D**). Another distinctive cluster harbored a follicular T helper/regulatory cell (TFH/TFR)-like transcriptional profile with proliferative/exhaustion hallmarks (*45*) (**fig. S7E**). Two other subsets were characterized by a type I IFN fingerprint (**fig. S7F**) and a CD8-like regulatory profile defined by immunosuppressive signaling pathways (*46–51*) (**fig. S7G and Data S2**).

Most of the mLNs emigrating cells to tdLNs were T cells although some B cells were also observed (**Fig. 4A**). To address the clonality of Treg cells that emigrated from the mLNs, we

performed single-cell and deep T cell receptor (TCR) sequencing of $CFSE^+$ T cells harvested from various locations at 24 hours post-mLNs CFSE injection. Unsupervised clustering of the $CFSE^+$ T cells partitioned the data into four cellular clusters, one composed of Treg cells, one of Tconv cells, and two of $CD8^+$ T cells (**Fig. 4B and fig. S8, A and B**). Based on TCR repertoire (*52*), tumor-infiltrating Treg but not Tconv cells exhibited higher clonal expansion in mice gavaged with *E. clostridioformis* compared to control mice (**Fig. 4C**). There was a 10-fold increase of TCRs from clusters composed of tumor/tdLNs TCRs in mice gavaged with *E. clostridioformis* compared with controls, with a concomitant decrease of TCRs from clusters restricted to mLNs (**Fig. 4D**). This recirculation affected preferentially Treg over Tconv cells (**Fig. 4C**). Similar clonal expansions were observed in the $CD8^+$ population (**fig. S8C**). The functional profile of mLNs Treg cells that reached the tumor differed from that of its origin, with an upregulation of genes involved in immunosuppression, cytolysis, and type-I IFN responses (**Fig. 4E** and **fig. S8A**). Oral gavage with *E. clostridioformis* significantly increased the proliferative potential of migratory Treg cells with the upregulation of genes implicated in cell cycle, chromatin silencing, and H3K27 trimethylation, as well as regulatory functions (*Il10*) within tumor beds (**Fig. 4, E and F**). The most striking commonality between mLNs emigrating $CD8^+$ and $CD4^+$ T cells reaching the sarcoma was the shutdown of the translation machinery, as previously reported in exhausted $CD8^+$ T cells in chronic infection and cancer (*53–56*) (**Fig. 4E, fig. S8, D and E, and Data S2**). Thus, the enterotropic $\alpha4\beta7^+$ $CD4^+$ T cells that translocate from the mLNs and PPs to the tdLNs comprise Treg and Tr17 cells that exhibit immunosuppressive functions. These immunosuppressive programs further increased when the cells reached the tumor bed, in conditions where the MAdCAM-1–α4β7 axis is compromised by neutralization or knockout of MAdCAM-1, recolonization post-ABX, or *E. clostridioformis*-induced dysbiosis.

The anticancer efficacy of PD-1 blockade relies on the MAdCAM-1–α4β7 axis

Given the immunosuppressive role of Tr17 cells during cancer immunosurveillance (*27*, *28*, *57*), disruption of the MAdCAM-1–α4β7 interaction may interfere with ICI-mediated anticancer effects. Loss of ileal *Madcam1* expression correlated with increased tumor size in tumor-bearing animals regardless of PD-1 blockade (**fig. S9A**). PD-1 blockade also reduced MCA205 fibrosarcoma growth in wild-type (WT) C57BL/6 mice, but failed to do so in *Madcam1*$^{-/-}$ mice and *Itgb7*$^{-/-}$ animals, which lack the β7 chain required for the formation of the α4β7 heterodimer

(**Fig. 5A**). Similarly, MCA205 fibrosarcoma, 4T1 breast and orthotopic TC-1 lung cancers normally reduced their growth in response to PD-1 blockade but failed to do so following injection of neutralizing anti-MAdCAM-1 or anti-α4β7 Abs (**Fig. 5B, C and D**). In *Madcam1*$^{-/-}$ mice, there was a constitutive increase of α4β7^{+} CD4^{+} T cells in the spleen and in the tumor where they represented approximately 3% of tumor-infiltrating lymphocytes (TILs) (**Fig. 5E**), as previously described (*58*). Injection of a neutralizing anti-MAdCAM-1 Ab during spontaneous tumor progression reshaped the TME and led to threefold increase in the intratumoral accumulation of Tr17 cells expressing intestinal T cell markers such as α4β7, CCR6, and CCR9 (**fig. S9, B and C**). Although only 17±0.9% of all MCA205 TILs were α4β7^{+}, 76±1.5% among Tr17 were α4β7^{+} (**fig. S9C**). In subcutaneous tumors (MCA205, 4T1), Treg cells represented 11.7±1.6% of α4β7^{+} CD4^{+} TILs and among these Treg cells, 44.5±5.3% were RORγt^{+} (**table S4**). Bacterial recolonization of the gut 4 days post-ACS phenocopied *Madcam1* gene deficiency, inducing a three-to-fivefold increase in the proportion of Tr17 cells in tumor beds (**Fig. 5, F and G**). The tumor-homing behavior of Tr17 cells was transient and no longer observed by 12 days post-ACS, except when anti-PD-1 Ab was coadministered (**Fig. 5H and fig. S9D**). Indeed, anti-PD-1 Abs facilitated the priming and/or the expansion of Tr17 cells in the mLNs in MCA205 tumor-bearing mice (**fig. S9E**) and contributed to the accumulation of Tr17 cells within tumors (**Fig. 5H, fig. S9, F and G**). In this context, intratumoral Treg represented 19.1±2.8% of α4β7^{+} CD4^{+} TIL, and among these Treg, 51.1±7.7% and 61.3±7% were RORγt^{+} and IL-17A^{+} respectively (**table S4**).

The recruitment of Tr17 cells promoted by PD-1 inhibition was further increased when *E. clostridioformis* (but not *Lactobacillus reuteri*) was supplemented by oral gavage after ACS discontinuation (**fig. S9H**). Blockade of the MAdCAM-1-α4β7 axis during PD-1-targeted immunotherapy impaired the infiltration of tumors by effector CCR5^{+} CD8^{+} cells (*59*, *60*) (**Fig. 5I**). Given that the antimicrobial and proinflammatory properties of IL-17, alone or with IL-22 (*61*, *62*), neutralizing these cytokines may circumvent the harmful effects of bacterial recolonization post-ABX during PD-1 inhibition. Indeed, neutralization of IL-17A (but not IL-22RA) counteracted the deleterious effects of ACS on PD-1 blockade (**Fig. 5J**). Thus, IL-17A plays a role in the immunosuppressive effects of ABX.

MAdCAM-1 liver expression reduced tumoral accumulation of enterotropic Treg cells

To strengthen the cause–effect relationship between MAdCAM-1 gut expression and emigration of enterotropic suppressive T cells to tumors, we enforced MAdCAM-1 expression in the liver by hydrodynamic injection of *Madcam1*-encoding cDNA inserted into a vector (*63*). Liver-specific overexpression of the transgene was verified by RT-qPCR and immunohistochemistry (IHC) (**Fig. 6, A and B**). Liver expression of MAdCAM-1 correlated with recirculation of the soluble form of MAdCAM-1 (sMAdCAM-1) (**fig. S9I**). There was a positive correlation between liver *Madcam-1* and *Foxp3* mRNA expression or the local presence of $FoxP3^+$ T cells (**Fig. 6C**). In ACS-treated mice, enforced hepatic MAdCAM-1 expression reduced the frequency of tumoral $\alpha4\beta7^+$ (but not $\alpha4\beta7^-$) Treg cells (**Fig. 6, D and E**). Moreover, high hepatic *Foxp*3 expression correlated with a reduction of tumor size (**Fig. 6F**). Anti-PD-1 Ab significantly increased liver *Rorc* expression, even more so upon ACS (**Fig. 6G**), with a positive correlation with liver *Madcam1* (**Fig. 6H**). Moreover, ACS-induced resistance to anti-PD-1 Abs could be circumvented when mice ectopically expressed *Madcam1* in the liver to locally retain Treg cells (**Fig. 6I**). There was a negative correlation between tumor size and liver *Madcam1* mRNA levels in these conditions (**Fig. 6J**). Thus, MAdCAM-1 acts as an immune checkpoint controlling the retention of Treg cells.

Soluble MAdCAM-1 is a strong prognostic factor of cancer patient responses

To investigate the clinical relevance of these findings, we first analyzed TIL infiltrates for the presence of enterotropic $\alpha4\beta7^+$ T cells in fresh human tumors and ex vivo propagated TILs. The $\alpha4\beta7^+$ fraction of Treg and $CD8^+$ T cells represented up to 8.3±2.1% and 24.5±6.9% respectively, expressed inhibitory receptors, and could electively produce IL-17 (**fig. S10, A and B**). $ROR\gamma t^+$ $FoxP3^{hi}$ cells represented 4.5±0.8% of $CD4^+$ cells in TILs in expansion and expressed the enterotropic marker $\alpha4\beta7^+$ (**fig. S10C**). Based on previous reports (*64*) and given the correlation between liver or ileal MADCAM-1 and circulating sMAdCAM-1 levels in mice (**fig. S9, I and J**), we analyzed the clinical significance of serum sMAdCAM-1 at diagnosis in two independent cohorts of 115 and 187 patients with advanced NSCLC treated with anti-PD-1/PD-L1 antibodies (**table S5**). Patients treated with ABX exhibited lower sMAdCAM-1 levels than ABX-free patients (**Fig. 7A**). Baseline serum sMAdCAM-1 was a strong independent prognostic factor of survival in NSCLC patients who did not take ABX and to a lesser extent in those who took ABX prior to ICIs (**Fig. 7B**), with high baseline levels associated with prolonged overall

survival (OS) and progression-free survival (PFS) (**Fig. 7C and fig. S10D**). Low sMAdCAM-1 levels identified the subset of PD-1 antibody-refractory patients within PD-L1^{hi} (≥50%) NSCLC tumors (**Fig. 7D and fig. S10E**). Using multivariate Cox regression analysis that took clinical variables into consideration revealed that sMAdCAM-1 is an independent prognostic factor in NSCLC patients (**table S5 and table S6**). Neither tumor mutational burden nor MER4 retrotransposon elements correlated with sMAdCAM-1 levels (65) (**fig. S10F**). We validated the clinical significance of serum sMAdCAM-1 as a biomarker of OS in 212 metastatic renal cell carcinoma (RCC) patients under second-line nivolumab (*66*) (**Fig. 7E and table S5**) and in 79 patients diagnosed with metastatic bladder cancer (BC) treated with durvalumab (anti-PD-L1) (*67*) (**Fig. 7F and table S5**).

To demonstrate the relationship between sMAdCAM-1 and gut dysbiosis in advanced NSCLC patients, we performed supervised hierarchical clustering of metagenomics species (MGS) defining the taxonomic composition of the intestinal microbiota using shotgun MG according to the median of sMAdCAM-1 serum levels (199 ng/ml) in 95 NSCLC patients (**table S7**). MGS richness and Shannon indices were reduced in sMAdCAM-1^{lo} (<median) compared to sMAdCAM-1^{hi} (≥median) patients (**Fig. 8A**). Moreover, the gut composition diverged between sMAdCAM-1^{lo} versus sMAdCAM-1^{hi} patients, as indicated by the ANCOM-based beta-diversity (**Fig. 8B**). Supervised MG analysis revealed two clusters of MGS that were significantly different in relative abundance between the two patient groups (**Fig. 8C**). Low circulating sMAdCAM-1 levels were associated with an increase in MGS from the genus *Enterocloster* (*E. clostridioformis)* which reduced ileal *Madcam1* expression in mice (**Fig. 1E**), and *E. bolteae*, which are both associated with chronic inflammatory disorders including cancer (*30*, *31*) and poor prognosis in patients treated with immunotherapy (*10*) (**Fig. 8D**). Thus, sMAdCAM-1 is a surrogate marker of intestinal dysbiosis and is associated with patient overall survival in advanced bladder, lung, and kidney cancer.

Discussion

To decipher the mechanisms involved in the immunosuppressive effects of ABX, we studied the emigration of T cells from the gut to distal tumors. We found that the relocation of enterotropic and immunosuppressive Tr17 cells to cancer-relevant compartments is at least partially controlled by the molecular interaction between MAdCAM-1 and α4β7. This

demonstration follows prior evidence that gut-derived Th17 cells control extraintestinal autoimmunity (*20–24*) and inflammation (*68*, *69*). Tr17 cells harbor an exacerbated immunosuppressive phenotype compared with conventional Treg cells (*26*). Recent intestinal Tr17 emigrants found in tdLNs exhibit gut-specific Treg cell features (*70*, *71*), Th17 cell-related gene expression patterns (*72*) as well as immunosuppressive traits such as *Dusp2*/PCA1 (*47*) and *Pik3ip1* (*73*). In tumors or tdLNs, gut T cell emigrants shut down protein translation and acquire features of exhaustion or lytic functions, perhaps reflecting chronic TCR stimulation (*56*). These data collected in tumor-bearing hosts may be interpreted in the context of IBD, in which the anti-α4β7 Ab vedolizumab increases the recirculation of extraintestinal α4β7$^+$ Treg cells and central memory Th17 cells (*74–76*). However, based on our results, α4β7 neutralization may have undesirable systemic immunosuppressive effects in the context of intestinal dysbiosis. Thus, prospective studies should monitor circulating sMAdCAM-1 and α4β7$^+$ Treg, Tr17, and Th17 cells in cancer patients treated with ICIs alone or in combination with FMT or vedolizumab in order to correlate these parameters with efficacy and toxicity.

Materials and Methods

Patient characteristics and clinical description.

Medical centers and regulatory approvals for translational research

For feces and serum collection, ancillary studies were conducted at Gustave Roussy (GRCC), France according to the ethical guidelines and approval of the local CCPPRB. The ONCOBIOTICS trial (NCT04567446, ID-RCB N°: 2017-A02010-53), a multicentric prospective observational study was designed to evaluate the impact of the microbiome composition in the clinical outcome of patients with advanced NSCLC treated with anti-PD-(L)1 (*10*). We enrolled patients across 12 academic centers in France and two centers in Canada. Adult patients with pathologically confirmed advanced non squamous or squamous NSCLC and an Eastern Cooperative Oncology Group (ECOG) performance-status score of 0-2, amenable to ICI as standard-of-care and compelling to provide a stool sample were eligible. Eligible patients received ICI following progression on platinum-based chemotherapy regimens, either with nivolumab or atezolizumab regardless of PD-L1 expression or with pembrolizumab if PD-L1 ≥ 1%. Given the subsequent approval of first-line ICI during the study accrual period, patients who received pembrolizumab monotherapy or in combination with platinum-based chemotherapy, depending on PD-L1 expression were also included. Standard-of-care treatment was continued until disease progression, unacceptable adverse effects, or completion as per protocol (2 years of ICI). Full eligibility criteria are listed in the trial protocol (available at NCT04567446). Baseline characteristics including a detailed listing of concurrent medications received the last 2 months prior to ICI initiation and the date of last follow-up were entered at each center in an electronic case report form. Feces were collected according to the International Human Microbiome Standards (IHMS) guidelines (SOP 03 V1) before the first injection. Serum samples were prospectively collected prior anti-PD(L)1 immunotherapy within the Gustave Roussy–sponsored PREMIS study (NCT03984318). Patients enrolled in PREMIS were ≥18 years , with histologically proven solid malignancy and at least one tumor evaluation by imaging after immunotherapy onset. The PREMIS study was approved by an ethical committee (Comité de Protection des Personnes Sud-Ouest et Outre Mer I; N°ID-RCB: 2018-A01257-48) and the institutional review board (CSET #2018/2728). All enrolled patients provided a signed informed consent. Furthermore, we disposed of one cohort of 45 patients with NSCLC receiving treatment with anti-programmed death 1 (PD-1/PD-L1) checkpoint inhibitors between 2014 and 2020. Patients were treated in the Georges François Leclerc Cancer center. For all patients, abundance of transcripts from RNA-seq data was

available, and for some patients, PD-L1 protein expression in tumor cells assessed using immunohistochemistry was also available, as well as tumor mutational burden (TMB) estimated from whole-exome sequencing. We had access to a cohort of patients with advanced renal cell carcinoma (RCC) treated with an anti-PD-1 enrolled in the NIVOREN trial (NCT03013335, N° EudraCT: 2015-004117-24). Finally, an additional cohort of patients with bladder cancer treated with an anti-PD-(L)1 alone or together with anti-CTLA-4 and enrolled in the IOPREDI study (EudraCT Number: 2016-005068-33) was studied. For tumor flow cytometric analyses of fresh or cultivated TILs, all tumor tissues were processed according to the Helsinki Declaration and the guidelines of the French ethics committee for research on human tissues. Tissue biocollection was registered with the French Ministry for Higher Education and Research (DC-2014-2206) with approval from the ethics committee (CPP Ouest IV, Nantes). Each patient included in this study signed an informed consent form. For the four fresh NSCLC tumors examined by flow cytometry, ≥18 year-old patients from Gustave Roussy Cancer Campus, Marie Lannelongue, Cochin, Tenon, Foch, Kremlin-Bicêtre, and Saint Joseph hospitals, with primary resectable tumors provided written informed consent according with protocols reviewed and approved by institutional ethics committee including the investigator-sponsored, study "mAb in sitro test", N°ID-RCB: 2016-A00732-49. The experiments conformed to the principles set out in the WMA Declaration of Helsinki and the Department of Health and Human Services Belmont Report. For collection of endoscopic and blood samples, a clinical study "Einfluss von Antibiotika auf das Darm-Chemokinnetzwerk bei Patienten mit soliden Tumoren" was conducted at University Clinics Heidelberg, Germany according to the ethical guidelines and approval of the Regierungspräsisium Karlsruhe.

Collection of endoscopic samples and blood samples

Eligible patients underwent ileocolonoscopy according to clinical standard protocols for non-study related indications (**table S2**) between July 2018 and November 2019. When feasible, endoscopic biopsies of the mucous membranes of the terminal ileum, caecum, and right and left colons were performed in each patient. Tissue samples were either snap frozen in liquid nitrogen and stored at −80°C or immersed into 2% PFA for histology. In addition, two blood samples (10 ml in EDTA tubes) were collected before ileocolonoscopy. All included patients responded to a questionnaire to assess dietary history and baseline clinical data were retrieved from the local clinical information system.

Metagenomic analysis of patient stools

Fecal samples were prospectively collected at different time points (V1: pre-ICI, V2: before the second ICI injection, V3: at 3 months post-ICI and V4: at 6 months post-ICI) at each center following the International Human Microbiome Standards (IHMS) guidelines, but only the baseline V1 sample was considered for this analysis. For metagenomic analysis, the stools were processed for total DNA extraction and sequencing with Ion Torrent technology following MetaGenoPolis (INRAE) France, as previously reported (*7*, *10*, *11*). The gene abundance table was processed using the MetaOMineR (momr R) package. We conducted PERMANOVA using the function adonis from the vegan R package (v2.5-7) with the Atchinson distance on centered log ratios using species-level abundances and 1000 permutations. We employed an ensemble of univariate and multivariate differential abundance methods that included age, gender and cohort in the models, using either species-level relative abundances or count data, where absolute raw counts were estimated from species-level relative abundances by multiplying these values by the total number of reads for each sample. These differential abundance methods included; DESeq2 (v.1.30.0) (*77*) with the poscounts estimator (DESeq2_poscounts); DESeq2 with the poscounts estimator and a zero-inflated negative binomial model (DESeq2_poscounts_zb); DESeq2 with trimmed mean of M values (TMM; DESeq2_TMM); limma (v3.46.0) (*78*) with TMM values (limma_voom_TMM); limma with TMM values and a zero-inflated negative binomial model (limma_voom_TMM_zb); ANCOM-BC (v.1.0.1) (*79*); Maaslin2 (v.1.4.0) (*80*) and LeFsE (*81*).

Soluble MAdCAM-1 quantification in patients

sMAdCAM-1 was quantified in patient sera with Bio-Plex 200 systems (Bio-Rad) and sMAdCAM-1 kit from R&D system (Human Luminex Discovery Assay LXSAHM).

Cell culture, reagents, and tumor cell lines

MCA-205 fibrosarcoma cells (syngeneic from C57BL/6 mice) and 4T1 WT and 4T1-*Il22ra1*$^{-/-}$ breast cancer cell lines (syngeneic from BALB/c, kindly provided by Dr. S. Kobold (*62*), LMU Klinikum, Germany) were cultured at 37°C in the presence of 5% CO_2 in RPMI 1640 containing 10% FCS, 2 mM L-glutamine, 100 IU/ml of penicillin–streptomycin, 1 mM sodium pyruvate, and MEM non-essential amino acids (henceforth referred to as complete RPMI 1640). Luciferase-transfected TC-1 cell lines (syngeneic for C57BL/6 mice, kindly provided by Prof. E. Deutsch

(Gustave Roussy Cancer Campus (GRCC)), France) were cultured at 37°C in the presence of 5% CO_2 in complete RPMI 1640 and 1 mM HEPES buffer. Cell lines were regularly tested for mycoplasma contamination and were not used after more than 10 passages.

Mice

All animal experiments were carried out in compliance with French and European laws and regulations. The local institutional animal ethics board and French Ministère de la Recherche approved all mouse experiments (permission numbers: 2016-049-4646, 2017_049_99741, 2019_036_21124, 2022_064_40164). Experiments were performed in accordance with Government and institutional guidelines and regulations. Female C57BL/6 and BALB/c were purchased from Harlan or Envigo (France). Mice were used between 7 and 12 weeks of age. *Madcam1*$^{-/-}$ and *Itgb7*$^{-/-}$ mice were a kind gift from A. Schippers (University hospital Aachen, Aachen, Germany). *Madcam1*$^{-/-}$ and *Itgb7*$^{-/-}$ mice and control littermates were backcrossed on the C57BL/6 background and were obtained from an in-house breeding at the local animal care facility at the University Hospital Aachen. The Kaede mice were a kind gift from M. Tomura (Kyoto University, Kyoto, Japan) and were backcrossed and maintained on the C57BL/6 background. All mouse experiments were performed at the animal facility in GRCC where animals were housed in specific pathogen-free conditions.

Antibiotic treatments

If not otherwise indicated, mice were treated with a broad-spectrum antibiotic (ABX) solution containing ampicillin (1 mg/ml), streptomycin (5 mg/ml), and colistin (1 mg/ml) (Sigma-Aldrich) (ACS) added to sterile drinking water. In experiments where single antibiotics were used, the concentrations were identical as stipulated above for ampicillin (A), colistin (C), or streptomycin (S), and were 1 mg/ml for erythromycin, 0.25 mg/ml for vancomycin, 6.15 mg/ml for ceftazidime, 4.1 mg/ml for cefepime, 16.4/2.05 mg/ml for piperacillin/tazobactam, and 1.13 mg/ml for rifaximin. Solutions and bottles were changed three times weekly. Antibiotic activity, in the experiments where the antibiotic mix was used, was confirmed by cultivating fecal pellets for 48 hours at 37°C in aerobic and anaerobic conditions. To evaluate the impact of antibiotics on MAdCAM-1 expression in the intestine, ACS were administered during 7 to 14 days and discontinued for 4 days (ACS+4d) or for 12 days (ACS+12d) or continued until the end of the experiment in drinking water of naive or MCA-205 tumor-bearing mice.

FMT experiments

In fecal microbial transplantation (FMT) experiments, mice received 3 to 7 days of ACS before undergoing FMT the next day by oral gavage. Fecal microbiota transfer (FMT) was performed by thawing fecal material. Mice were placed in a new cage. Two hundred microliters of the suspension was then transferred by oral gavage into each ATB pre-treated recipient using animal feeding needles. In addition, another 100 µl was applied to the fur of each animal.

Oral bacterial gavage with commensal species

Akkermansia p2261 was provided by everImmune, Villejuif, France. *Enterococcus hirae* 13144 isolates were originally isolated from spleens or mesenteric lymph nodes of SPF mice treated with cyclophosphamide at GRCC, Villejuif, France. *Enterocloster clostridioformis* was isolated from the ileum of mice that received ACS in drinking water for 7 days followed by 4 days ABX-free at GRCC, Villejuif, France. *Akkermansia* p2261, *E. clostridioformis* and *Lactobacillus reuteri* were grown on COS plates in an anaerobic atmosphere created using three anaerobic generators (Biomerieux) at 37°C for at least 72 hours. *E. hirae* 13144 was grown in 5% sheep blood enriched Columbia agar for 24 hours at 37°C in aerobic conditions. Colonization of specific-free pathogens (SPF) C57BL/6 mice was performed by oral gavage with 100 µl of suspension containing 1×10^8 to 1×10^9 bacteria. Bacteria concentrations were calculated using a fluorescence spectrophotometer (Eppendorf) at an optical density of 600 nm in NaCl 0.9%. Mice were gavaged one to four times. In applicable experiments, oral gavages were performed concomitantly with anti-PD-1 Ab treatment four times. The identification of specific bacteria was accomplished using a matrix-assisted laser desorption/ ionization coupled with time-of-flight mass spectrometry (MALDI-TOF) (BRUCKER, France).

Oral gavage with biliary acids

Mice were gavaged four times, every 2 days with 120 mg per kilogram of body weight with lithocholic acid (LCA, ThermoFisher ref. 229090050) or ursodeoxycholic acid (UDCA, DELURSAN® Teva Santé) diluted in corn oil.

Subcutaneous cancer mouse models

MCA205 sarcoma and 4T1 WT and Il22ra1$^{-/-}$ breast cancer

Syngeneic C57BL/6 mice were implanted with 0.8×10^6 MCA-205 sarcoma cells subcutaneously and treated intraperitoneally (i.p.) when tumors reached 20 to 40 mm² in size with anti-PD-1 mAb (250 µg/mouse; clone RMP1-14) or isotype control (clone 2A3). Syngeneic BALB/c mice were implanted with 0.5×10^5 4T1 WT or *Il22ra1*$^{-/-}$ breast cancer cells subcutaneously and treated i.p. with anti-PD-1 or isotype control mAbs. Mice were injected four times at 3-day intervals with anti-PD-1 (Bio X Cell, clone RPMI-14, 250µg/mouse) or isotype control (Bio X Cell, clone 2A3, 250µg/mouse) mAbs. Tumor length and width were routinely monitored three times a week by means of a caliper. In experiments using anti-α4β7 mAb (DATK32, 200 µg per mouse) or anti-MAdCAM-1 mAb (MECA-367, 200 µg per mouse), or their isotype controls (clone 2A3 in both cases), monoclonal Abs were injected i.p. every 3 days starting from day 0 until the final anti-PD-1 injection. In the experiment using anti-IL-17A mAb (clone IL-17F, 100 µg per mouse), mice were injected i.p. concomitantly with anti-PD-1 treatment. All antibodies were purchased from Bio X Cell, NH, USA. In the experiment using anti-CD62L or anti-PSGL-1 mAbs (clones Mel-14 and 4RA10, respectively, 100 µg per mouse), mice were injected i.p. concomitantly with anti-MAdCAM-1 treatment.

Orthotopic luciferase engineered-TC-1

C57BL/6 mice were anesthetized with isoflurane. Under sterile conditions, a lateral incision was made on the chest wall of each mouse and 6×10^5 TC-1-Luc cells in 10 µl of Matrigel (Corning) were injected into the lung. The skin incision was closed with a surgical skin clip. To monitor tumor growth twice weekly, mice received a percutaneous injection of luciferase substrate (beetle luciferin, potassium salt, Promega) at a dose of 150 mg per kilogram of body weight. Eight minutes post-luciferin inoculation, photons were acquired on a Xenogen IVIS 50 bioluminescence in vivo imaging system (Caliper Life Sciences Inc., Hopkinton, MA, USA).

Construction of liver-specific overexpression vector

The plasmid pLIVE vector was purchased from Mirus (Cat. #MIR 5420, Madison, WI, USA), and Madcam1 (NM_013591) mouse-tagged ORF clone from OriGene (Cat. #MR226268, Rockville, MD, USA). pLIVE vector, which is designed for liver-specific expression and utilizes a chimeric promoter composed of the mouse minimal albumin promoter and the mouse alpha fetoprotein enhancer II, was selected to construct the liver-specific Madcam1 overexpression vector.

The gene encoding mouse Madcam1 was amplified from Madcam1 (NM_013591) mouse tagged ORF clone (pCMV6-Entry-Madcam1) with primers listed below by RT-PCR with OneTaq hot start DNA polymerase (Cat. #M0481, NEB, Ipswich, MA, USA). For more effective expression of Madcam1, Kozak sequence (underlined) were selected and added in forward primer (Madcam1-F-Kozak: 5′-GGCGCGCCGCCACCATGGAATCCATCCTGGCC-3′; Madcam1-R:5′-CTCGAGTCATAGGTGTGT ACATGAGC-3′). The Madcam1 cDNA was then cloned into the AscI and Xho I sites of the pLIVE vector, yielding the pLIVE-Madcam1 plasmid. The large amount of vector DNAs were prepared by an PureLink™ expi endotoxin-free maxi plasmid purification kit (Cat. #A31231, Invitrogen, Carlsbad, CA, USA) for further hydrodynamic tail vein injection.

Generation of a liver-specific overexpression mouse model

Six-week-old female wild-type C57BL/6 mice were purchased from Envigo, France (Envigo, Huntingdon, UK). All mice were maintained in a temperature-controlled and pathogen-free environment with 12-hour light–dark cycles with food and water ad libitum. The constructs of pLIVE as a control and pLIVE-Madcam1 vector DNA (250 μg per mouse) were delivered to the mouse liver using the hydrodynamic tail vein injection procedure by using the TransIT®-QR hydrodynamic delivery solution (Cat. #MIR 5240, Mirus, Madison, WI, USA) according to the manufacturer's instructions.

Flow cytometry

Mouse

Tumors, mesenteric lymph nodes (mLNs), draining lymph nodes (tdLNs), contralateral lymph nodes (cLNs), ilea, and spleens were harvested at different time points as indicated in the individual experiments. Excised tumors were cut into small pieces and digested in RPMI medium containing Liberase^{TM} at 25 μg/ml (Roche) and DNase1 at 150 IU/ml (Roche) for 30 min at 37°C and then crushed and filtered twice using 100-μm and 70-μm cell strainers (Becton & Dickinson). Lymph nodes and spleen were crushed in RPMI medium and subsequently filtered twice through a 100-μm cell strainer. Ilea were collected and fat tissue, Peyer's patches, and feces were removed. Intestines were cut longitudinally and then cut transversally into small pieces into a tube. Pieces were transferred into a new 50-ml tube with 20 ml of IEC washing medium (PBS, 5% FCS, 5 mM EDTA, and 1 mM DTT), vortexed and shaken at 37°C for 20 min. Tissue and cell suspension were

filtered with a cell strainer (100 µm). The filtered cell suspension was discarded. The remaining tissue was incubated for 30 min in LPC medium (RPMI, 5% FCS, 0.25 mg/ml collagenase VIII, and 10 U/ml of DNAse I) and then dissociated through a 100-µm cell strainer. The cells obtained from the lamina propria in cell suspension were washed twice with PBS and kept on ice for subsequent analysis. Four million cells from each sample were preincubated with purified anti-mouse CD16/CD32 (clone 93; eBioscience) for 30 min at 4°C, before membrane staining. For intracellular staining, the FoxP3 staining kit (eBioscience) was used. Dead cells were excluded using the Live/Dead Fixable Yellow dead cell stain kit (Life Technologies) or LIVE/DEAD™ Fixable Aqua Dead Cell Stain Kit (Biolegend). For IL-17 and IL-22 staining, cells were stimulated at 37°C during 4 hours with PMA/Ionomycine and Golgi stop cocktail. The list of antibodies (clones, sources and concentrations) used to stain murine cells is in **table S8**. Stained samples were acquired on CytoFLEX S 13 colors (Beckman Coulter) and analyses were performed with Kaluza software 2.1 (Beckmann Coulter). Th17 cell gating depended on the mouse model that was used. The Kaede fluorochrome could not retain its photoconverted state upon fixation with PFA. For Kaede mice, Th17 cells were identified as $CXCR3^{-}$ and $CCR6^{+}$ $CD4^{+}$ T cells and Tregs as $CD127^{-}CD25^{hi}$ $CD4^{+}$ T cells. In other mouse models, Th17 and Tr17 cells were defined after gating on $ROR\gamma t^{+}$ $CD4^{+}$ or $ROR\gamma t^{+}$ and/or $IL\text{-}17A^{+}$ $CD25^{+}$ $FoxP3^{+}$ $CD4^{+}$ cells, respectively.

Human

The list of antibodies (clones, sources and concentrations) used to stain human cells is in **table S9.** For IL-17 and IL-22 staining, cells were stimulated at 37°C during 4 hours with PMA ionomycin and brefeldin A (Invitrogen Cat#00-4975). Dead cells were excluded using the LIVE/DEAD™ Fixable Aqua Dead Cell Stain Kit (Biolegend). Stained samples were acquired on BD LSRFortessa™ X-20 Cell Analyzer and analyzed with FlowJo v10.8.1 software.

Immunohistochemistry and quantification of MAdCAM-1 in ilea

Mice ilea “Swiss rolls” were prepared from the experiments and fixed in buffered formalin for 24-48 hours and then sent to conventional histological processing. For morphological analysis, hematoxylin, eosin, & saffron staining (HES) slides were generated. Bond Leica automated immunostainer instruments were used to perform immunohistochemistry. Three micrometer thick paraffin sections were processed for heat-induced antigen retrieval (ER2 corresponding EDTA buffer pH9) for 20 min at 100°C. Slides were incubated with the antibody for 1 hour at room temperature. For MAdCAM-1 staining, slides were incubated with MAdCAM-1 antibody

(Abcam, AP-MAB0842, rat, 1:100) for 1 hour at room temperature. Slides were incubated with a polink rat kit as secondary antibodies and revealed with DAB. (Thermofisher, ready for use solution, 1ml), after incubation for 5 minutes at room temperature.

For image analysis and MAdCAM-1 quantification, QuPath software was used (*82*). ROIs were defined firstly by "simple tissue detection" function and modified by hand in each whole slide image (WSI). To quantify the cell density of biomarker-positive cells, "Positive cell detection" was used.

Histological processing of MAdCAM-1 expressing-liver

Murine livers were obtained from the experiments and fixed in buffered formalin for 24-48 hours and then cut vertically in parallel sections, which were sent for conventional histological processing. For morphological analysis, hematoxylin, eosin, & saffron staining (HES) slides were generated. Bond Leica automated immunostainer instruments were used to perform immunohistochemistry. Three micrometer thick paraffin sections were processed for heat-induced antigen retrieval (ER2 corresponding EDTA buffer pH9) for 20 min at 100°C. Slides were incubated with the antibody for 1 hour at room temperature. The following antibodies were used: anti-FoxP3 (Cell Signaling, D608R, rabbit, 1:200, ER2) and anti-RORγt (Abcam, EPR20006, rabbit, 1:3000, ER2). The antibodies were detected with di-amino-benzidine-peroxidase (DAB) (Thermofisher, ready for use solution, 1ml), after incubation for 5 minutes at room temperature. Finally, the sections were counterstained by hematoxylin (Leica Biosystems).

Quantification of FoxP3 and MAdCAM-1 in MAdCAM-1 expressing-liver

Images for analysis were acquired as WSI with a slide scanner Zeiss Axio Scan.Z1 and Olympus VS120 whole-slide imaging system. Image analysis was performed using QuPath, version 0.3.2 (*102*). WSI for FoxP3 were evaluated through multiple steps: (1) simple tissue detection was performed (threshold 220, requested pixel size 20 µm, minimum area 100,000 μm^2, max fill area 100,0000 μm^2, smooth image, cleanup with median filter, smooth coordinates, single annotation); (2) fast cell counts (cell detection channel DAB, Gaussian sigma 1.5 µm, background radius 15 µm, use difference of Gaussians, cell detection threshold 0.5, DAB threshold 0.5); (3) exclusion of detections corresponding to artifacts (folded tissue, dark pigment sedimented, hemorrhage, intravascular lymphocytes) was performed by a pathologist (LL); (4) create density map; (5) select the region of interest (ROI) with 1 mm^2, representing the highest density in the tissue (hotspot).

Hot-spot density was then normalized for each experiment based on the control group, then pooled (n=2). WSIs for RORγt were evaluated for hotspot in comparison to the same ROI as indicated for FoxP3. The RORγt positive nuclei were then counted manually, based on morphology, as many nuclei from hepatocytes were also stained in some of the evaluated conditions.

Tracing migration of leukocytes from the gut to the TME

Kaede experiments

Kaede transgenic mice were anesthetized with 2 to 2.5% isoflurane and administered buprenorphine (0.01 mg per kilogram of body weight) i.p. for analgesia. For photoconversion of ilea, abdominal skin and peritoneum were cut at the midline to access the intraperitoneal terminal ileum. For photoconversion of the caecum, ileum, and mesenteric lymph nodes, the cecal pole was first identified. Then the cecal pole including the terminal ileum, the mesenteric lymph nodes, and the proximal colon were gently mobilized through the midabdominal incision onto a sterile plastic-coated surgical drape. Non-target structures were covered with aluminum foil. The ventral and dorsal parts of the targeted structures were exposed to ultraviolet light emitted from a 395 nm wave length emitting Diode (Winzwon) light for 30 s each. After illumination, the tissue was moistened with sterile isotonic sodium chloride and gently repositioned into the peritoneal cavity. The peritoneal membrane was closed by continuous stitch with a 5-0 monofil nylon suture (Ethicon). The skin was closed with two 9-mm wound clips (EZ Clip Kit). ***CFSE staining of mesenteric LN cells up to TME or tumor draining lymph nodes.*** C57BL/6 mice were anesthetized with 2 to 2.5% isoflurane and administered buprenorphine (0.01 mg per kilogram of body weight) i.p. for analgesia. Abdominal skin and peritoneum were cut at the midline to access the mesenteric lymph nodes. The mesenteric lymph nodes were gently mobilized through the midabdominal incision onto a sterile plastic-coated surgical drape. Ileum draining mesenteric lymph nodes were visually identified according to their vasculature. The two most prominent mesenteric lymph nodes were injected with 100 µM CFSE diluted in 5 µl of PBS using a 30G insulin syringe. After repositioning the mesenteric lymph nodes, the peritoneal membrane was closed by continuous stitch with a 5-0 monofil nylon suture (Ethicon).

RNA extraction and RT-qPCR

Lysis and extraction protocols were identical for human and mouse samples. Tumor or intestinal samples were snap-frozen in liquid nitrogen in RLT Plus buffer containing 0.1% beta

mercaptoethanol. On the day of extraction, samples were thawed at 4°C and homogenized in a microtube homogenizer (Benchmark Scientific) in RNA-free glass bead tubes (Dutscher). Total RNA extraction and genomic DNA removal were performed with the RNeasy Mini kit (Qiagen), following the manufacturer's recommendations. A maximum of 1 µg of RNA, measured using a NanoDrop™ Spectrophotometer (Thermo Fischer Scientific), was reverse-transcribed into cDNA with a mix composed of SuperScript III Reverse Transcriptase (Life Technologies), RNaseOUT™ Recombinant Ribonuclease Inhibitor (Life Technologies), random primers (Promega), and Deoxynucleoside Triphosphate Set, PCR grade (Roche Diagnostics).

Quantitative gene expression assay

The expression of mouse and human *B2M*, *FOXP3*, *IFNG*, *IL10*, *IL17A*, *IL22*, *MADCAM1*, *VCAM1*, *PPIA*, *RORC*, *IL18*, AND *TBX21* genes (all from Life Technologies) was analyzed with the TaqMan® Gene Expression Assay using the Universal Master Mix II on a StepOnePlus™ Real-Time PCR System (Life Technologies). Amplifications were performed using the following ramping profile: one cycle at 95°C for 10 min, followed by 45 cycles of 95°C for 30 s, and 60°C for 1 min. Quantitative RT-PCR data were normalized to the expression levels of the housekeeping genes *B2M* or *Ppia,* as indicated in each figure, by means of the $2^{-\Delta Ct}$ method multiplied by 10^6.

Tissue lysis and chemokine analyses

Intestinal and tumoral samples were snap-frozen in liquid nitrogen in a nondenaturing cell lysis buffer containing 50 mM Tris HCL pH 7.4, 150 mM NaCl, 300 mM sucrose, 10 mM EDTA, 0.1% Triton 100X, and Complete™, Mini, EDTA-free Protease Inhibitor Cocktail (Roche). For subsequent lysis, samples were thawed at 4°C and lysed on a tube homogenizer (Precellys) in ceramic beads lysis tubes (Precellys). Tissue homogenate was centrifuged at 4000*g* for 5 min. The supernatant was used for subsequent analysis. Chemokine concentrations in the tissue lysate were determined according to the manufacturer's recommendation using CCL2, CCL3, CCL4, CCL5, CCL25, and MAdCAM-1 Duoset ELISA kits (R&D) or using Legendplex Mouse proinflammatory chemokine panel (Biolegend) with cytometric analysis performed on a CytoFLEX S (Beckmann coulter).

Ileal tissue sample preparation and bile acid detection by UHPLC-MS

Approximately 30 mg of collected tissue was weighed and placed in a 2-ml homogenizer tube with ceramic beads (Precellys, Bertin Technologies, France) with 1 ml of ice-cold extraction mixture (9:1 methanol–water, −20°C, with labeled ^{13}C-glycocholic acid as internal standard). To facilitate the extraction of endogenous metabolites, samples were then completely homogenized (3 cycles of 20 s/ 2380*g*; Precellys 24, Bertin Technologies, Montigny-le-Bretonneux, France) and centrifuged (10 min at 15,000*g*, 4°C). In order to detect bile acids, 300 µl of supernatant was collected and treated following a previously described protocol (*83*). Bile acids were analyzed by LC-MRM (Multiple Reaction Monitoring) with a 1290 UHPLC (Ultra-High Performance Liquid Chromatography, Agilent Technologies) coupled to a mass spectrometer 6470 TQ (Triple Quadrupole, Agilent Technologies), as previously described (*84*). Targeted data were cleaned with a R (version 4.0) dedicated package (@Github/Kroemerlab/GRMeta).

Bulk RNA sequencing of α4β7$^{+/-}$ CD4^{+} mesenteric T cells

α4β7^{+} and α4β7^{-} CD4^{+} T cells were isolated from mLNs by flow cytometry. Preparation of mRNA-Seq libraries and nextseq 75SE run deep sequencing were performed at GeneCore EMBL (Heidelberg, Germany).

Single-cell RNA sequencing by BD Rhapsody

After isolation of CFSE^{+} CD4^{+} T cells by flow cytometry, 10,000 cells were washed in cold PBS and loaded onto a BD Rhapsody™ cartridge and processed according to the manufacturer's instructions for targeted single-cell RNA-seq using the predesigned Immune Response Panel (Mouse). The library was clustered at 1.75 pM on a NextSeq500 system (Illumina) to generate ~40,000 paired-end reads per cell using High Output v2 chemistry. Sequenced single-cell data was demultiplexed using bcl2fastq2 v2.20.

Single-cell TCR and RNA library construction and sequencing by 10X Genomics Chromium

After isolation of CFSE^{+}CD4^{+} and CD8^{+} T cell by flow cytometry from mLNs, cLNs, tdLNs, and tumors, single-cell-library construction was performed using Chromium Next GEM Single Cell 5' Kit v2 (PN-1000263), Chromium Next GEM Chip K Single Cell Kit (PN-1000287), Single Cell VDJ 5′ Gel Bead, Chromium Single Cell Mouse TCR Amplification Kit, 16 rxns (reactions) (PN-

1000254) , Library Construction Kit (16 rxns) (PN-1000190), and Dual Index Kit TT Set A (96 rxns) (PN-1000215) kits according to the manufacturer's protocol. Briefly, single-cell suspensions from a total of 500 to 20,000 cells with barcoded gel beads and partitioning oil were loaded to Chromium Next GEM Chip K to generate single-cell gel bead-in-emulsion. Full-length cDNA along with cell barcode identifiers were PCR-amplified to generate 5′Gene Expression (GEX) libraries and V(D)J libraries. Libraries were sequenced using a NovaSeq 6000 (Illumina) to achieve a minimum of 23,000 paired-end reads per cell for GEX and 7000 paired-end reads per cell for V(D)J. Reads were aligned using Cell Ranger v6.1.1 to the GRCm38 mouse references.

Repertoire clonality

TCR sequencing data were processed using the "immunarch" R package.

Clonotypes within each population and compartments were then divided into fractions with an occurrence of 1 or >1. The cumulative frequency of each fraction was calculated within the repertoire of each sample.

Sequence similarity analysis

DeepTCR was used to cluster paired TRA-TRB clonotypes based on sequence similarity, using a train Variational Autoencoder (VAE). This generates clusters composed of sequences with a likelihood of shared specificities. The clusters were assigned as being mLNs, tumor/dLN or shared based on the percentage of clonotypes composing them. A cluster was considered as specific to a compartment if the log2FC was equal to or higher than 1.5. Otherwise, clusters were considered as shared between the compartments (*52*).

Single cell RNA-seq analysis

Expression matrices were analyzed using the R environment (version 4.2.1) with the Seurat package (v4.2.1). High-quality cells characterized by fewer than 10% of mitochondrial genes more than 200 UMI features and less than 15,000 unique UMI were selected for further analysis. Count matrix was normalized with regularized negative binomial regression based on the 3000 most variable genes using the SCTransform function. Principal component analysis was used for dimensionality reduction using the RunPCA on the 3000 most variable genes. Contributive components were identified visually using an elbow plot. Nearest neighbors were determined with the FindNeigbhors function using contributive PCA components and cells were clustered using

the louvain clustering algorithm with the FindClusters function. Resolution of the clustering algorithm was chose based on a bootstrapping procedure, the resolution giving rise to the maximum number of clusters with co-assignments probabilities superior to 5% was chosen. Differential gene expression (DGE) analysis was performed using the FindMarkers function and p-value were corrected using the p.adj base function with the false discovery rate procedure. Volcano plot visualization was performed using the ggplot2(v3.4.0) R package, Heatmap visualization was performed using the ComplexHeatmap (v2.14.0) R package and Venn Diagram visualization was performed using the ggven R package (v0.1.9).

Cell lines and treatment

Culture media and supplements for cell culture were obtained from Life Technologies (Carlsbad, California, USA) and plastic material was obtained from Greiner BioOne (Kremsmünster, Austria) and Corning (Corning, New York, USA). Mouse transformed endothelial sinusoidal cells (TSECs) were a generous gift from Professor B.P. Fennimore (University of Colorado Anschutz Medical Campus, Aurora, CO, USA) and brain endothelial cells (bEnd.3) were purchased from ATCC. TSECs were cultured in DMEM/F-12 (Dulbecco's Modified Eagle Medium/Nutrient Mixture F-12) plus endothelial growth supplement (Cat. #1052, ScienCell, Carlsbad, CA, USA), supplemented with 10% fetal bovine serum (FBS), 10 U/ml of penicillin sodium and 10 µg/ml of streptomycin sulfate. bEnd.3 cells were cultured in DMEM with 2.5 mM L-glutamine, supplemented with 10% FBS, 10 U/ ml of penicillin sodium and 10 µg/ml of streptomycin sulfate. Both cell lines were cultured in the presence of 5% CO_2 at 37°C. Transfected TSEC (TSEC::MAdCAM-1-GFP) and bEnd.3 cells (bEnd.3::MAdCAM-1-GFP) were selected with 500 µg/ml of G418 sulfate (50 mg/ml, Cat. #10131027, Gibco) and stable transformants were maintained under G418 selection pressure. Recombinant murine TNF-α (Cat. #315-01A, PeproTech) and IL-1β (Cat. #211-11B, PeproTech) were diluted in culture media from a stock of 40 µg/ml at the time of treatment. Bile acids (lithocholic acid (LCA) (#700218P-10MG, Sigma-Aldrich), dehydrolithocholic acid (3-oxo-LCA) (#700217P-10MG, Sigma-Aldrich), allolithocholic acid (allo-LCA) (#700330P-5MG, Sigma-Aldrich), isoallo-LCA (#R203424-1MG, Sigma-Aldrich), taurolithocholic acid sodium salt (Tauro-LCA) (#700252P-10MG, Sigma-Aldrich), sodium chenodeoxycholate (CDCA) (#C8261-1G, Sigma-Aldrich), sodium taurochenodeoxycholate (TCDCA) (#T6260-100MG, Sigma-Aldrich), deoxycholic acid (DCA) (#30960-25G, Sigma-Aldrich), ursodeoxycholic acid (UDCA) (#208590250, Thermoscientific),

tauroursodeoxycholic acid (TUDCA) (#580549-1GM, Millipore), glycoursodeoxycholic acid (GUDCA) (#06863-1G, Sigma-Aldrich), taurodeoxycholic acid (TDCA) (#580221-5GM, Millipore)) and FXR agonists/antagonists (GW4064 (#G5172-5MG, Sigma-Aldrich), cilofexor (#HY-109083, MCE), tropifexor (#HY-107418, MedChemExpress (MCE)), and (Z)-guggulsterone (#G5168-25MG, Sigma-Aldrich)) dissolved in DMSO were diluted 1:1000, 1:10,000, and 1:100,000 in culture media to a final concentration of 100 μM, 10 μM, and 1 μM. Bacteria were cultured (and in some instances pasteurized) before being diluted in culture media to a working concentration with an optical density (OD) of 0.5, 0.25, and 0.1 (*Akkermansia p2261* everImmune strain, *E. clostridioformis*).

Construction of MAdCAM-1 promoter plasmid

The MAdCAM-1 promoter construct is a PCR product from mouse genomic DNA amplified using 5′-GGAATTCTACCCCCACAGGCCTGCC-3′ as forward primer (EcoRI site is underlined, Eurofins, Nantes, France) and 5′-AGGCCGCGGGGGCCGGCAGCTTCCTAC-3′ as the reverse primer (SacII site is underlined, Eurofins). After digestion by EcoRI-HF and SacII (NEB, Ipswich, MA, USA), the MAdCAM-1 promoter DNA fragment was extracted using a Monarch® DNA gel extraction kit (NEB, Ipswich, MA, USA). The purified fragments were subcloned into the promoterless pAcGFP1-1 vector (Clontech, Mountain View, CA, USA).

Establishment of MAdCAM-1 promoter reporter cell lines

TSEC and bEnd.3 cells were transfected with the recombinant expression vector pAcGFP1-1-MAdCAM-1 using FuGENE® HD transfection reagent (Cat. # E2312, Promega). Twenty-four hours post-transfection, stable transfectants were isolated by selection with 500 μg/ml of G418. The transfectants (namely TSEC::MAdCAM-1-GFP and bEnd.3::MAdCAM-1-GFP) were maintained in culture medium containing 500 μg/ml of G418 for 2 weeks. The G418-resistant cells were selected and single cell clones were isolated to establish TSEC::MAdCAM-1-GFP and bEnd.3::MAdCAM-1-GFP stable cell lines expressing GFP under the control of the MAdCAM-1 promoter.

High-content microscopy

TSEC::MAdCAM-1-GFP and bEnd.3::MAdCAM-1-GFP were seeded in 384-well/96-well μclear imaging plates (Greiner BioOne) and allowed to adapt overnight. Cells were treated with the

indicated agents, then fixed with 3.7% paraformaldehyde (PFA, w/v in PBS) (Cat. #F8775, Sigma-Aldrich) containing 2 µg/ml of Hoechst 33342 at 4°C overnight. Subsequently, the fixative was exchanged with PBS and the plates were analyzed by automated microscopy. Image acquisition was performed using an ImageXpress Micro C automated confocal microscope (Molecular Devices, Sunnyvale, California, USA) equipped with a 20X PlanApo objective (Nikon, Tokyo, Japan), followed by automated image processing with the R software, using the EBImage package (available from the Bioconductor repository https://www.bioconductor.org) and the MorphR package (available from the GitHub repository https://github.com/kroemerlab/MorphR) In short, cytoplasm and nucleus, were segmented and fluorescence intensities were assessed. After exclusion of cellular debris and dead cells, data was normalized, statistically evaluated, and graphically depicted. Images were also extracted and pixel intensities scaled (to the same extent for all images of a given experiment) using R software,. At least four view fields were analyzed per well and each experiment was assessed at least four times.

Statistics

In vitro and in vivo

Data analyses were performed either with the statistical environment R (http://www.R-project.org/) or Prism 6 (GraphPad, San Diego, CA, USA). The standardization of each marker was performed using the *z*-score (difference of each sample value from the mean/standard deviation). When a control group was available, the data was standardized by dividing the value by the mean of the control group. The non-parametric Mann–Whitney *U* test was used for comparison of two unpaired groups. The Wilcoxon matched-pairs signed-rank test was used to compare two groups of paired samples. For the comparison of more groups, we used the Kruskal–Wallis *H* test, correcting the statistical significance for multiple comparison and false discovery rate (FDR) using the two-stage step-up method of Benjamini, Krieger, and Yekutieli. All reported tests are two-tailed and were considered significant at $P<0.05$.

Patients

sMAdCAM-1 as a prognostic factor of the patient response in NSCLC, RCC and bladder cancer patients. For each cohort, two groups of patients were defined by the sMAdCAM-1 median. Overall survival and progression-free survival analyses were performed using Kaplan–Meier estimator and the patient groups were compared using the log-rank (Mantel–Cox) test.

References

1. C. Robert, L. Thomas, I. Bondarenko, S. O'Day, J. Weber, C. Garbe, C. Lebbe, J.-F. Baurain, A. Testori, J.-J. Grob, N. Davidson, J. Richards, M. Maio, A. Hauschild, W. H. Miller, P. Gascon, M. Lotem, K. Harmankaya, R. Ibrahim, S. Francis, T.-T. Chen, R. Humphrey, A. Hoos, J. D. Wolchok, Ipilimumab plus dacarbazine for previously untreated metastatic melanoma. *N. Engl. J. Med.* **364**, 2517–2526 (2011).

2. J. Brahmer, K. L. Reckamp, P. Baas, L. Crinò, W. E. E. Eberhardt, E. Poddubskaya, S. Antonia, A. Pluzanski, E. E. Vokes, E. Holgado, D. Waterhouse, N. Ready, J. Gainor, O. Arén Frontera, L. Havel, M. Steins, M. C. Garassino, J. G. Aerts, M. Domine, L. Paz-Ares, M. Reck, C. Baudelet, C. T. Harbison, B. Lestini, D. R. Spigel, Nivolumab versus Docetaxel in Advanced Squamous-Cell Non-Small-Cell Lung Cancer. *N. Engl. J. Med.* **373**, 123–135 (2015).

3. S. Spranger, R. Bao, T. F. Gajewski, Melanoma-intrinsic β-catenin signalling prevents anti-tumour immunity. *Nature*. **523**, 231–235 (2015).

4. J. Gao, L. Z. Shi, H. Zhao, J. Chen, L. Xiong, Q. He, T. Chen, J. Roszik, C. Bernatchez, S. E. Woodman, P.-L. Chen, P. Hwu, J. P. Allison, A. Futreal, J. A. Wargo, P. Sharma, Loss of IFN-γ Pathway Genes in Tumor Cells as a Mechanism of Resistance to Anti-CTLA-4 Therapy. *Cell*. **167**, 397-404.e9 (2016).

5. N. J. Neubert, M. Schmittnaegel, N. Bordry, S. Nassiri, N. Wald, C. Martignier, L. Tillé, K. Homicsko, W. Damsky, H. Maby-El Hajjami, I. Klaman, E. Danenberg, K. Ioannidou, L. Kandalaft, G. Coukos, S. Hoves, C. H. Ries, S. A. Fuertes Marraco, P. G. Foukas, M. De Palma, D. E. Speiser, T cell–induced CSF1 promotes melanoma resistance to PD1 blockade. *Science Translational Medicine*. **10**, eaan3311 (2018).

6. A. Elkrief, L. Derosa, G. Kroemer, L. Zitvogel, B. Routy, The negative impact of antibiotics on outcomes in cancer patients treated with immunotherapy: a new independent prognostic factor? *Ann. Oncol.* (2019), doi:10.1093/annonc/mdz206.

7. B. Routy, E. Le Chatelier, L. Derosa, C. P. M. Duong, M. T. Alou, R. Daillère, A. Fluckiger, M. Messaoudene, C. Rauber, M. P. Roberti, M. Fidelle, C. Flament, V. Poirier-Colame, P. Opolon, C. Klein, K. Iribarren, L. Mondragón, N. Jacquelot, B. Qu, G. Ferrere, C. Clémenson, L. Mezquita, J. R. Masip, C. Naltet, S. Brosseau, C. Kaderbhai, C. Richard, H. Rizvi, F. Levenez, N. Galleron, B. Quinquis, N. Pons, B. Ryffel, V. Minard-Colin, P. Gonin, J.-C. Soria, E. Deutsch, Y. Loriot, F. Ghiringhelli, G. Zalcman, F. Goldwasser, B. Escudier, M. D. Hellmann, A. Eggermont, D. Raoult, L. Albiges, G. Kroemer, L. Zitvogel, Gut microbiome influences efficacy of PD-1-based immunotherapy against epithelial tumors. *Science*. **359**, 91–97 (2018).

8. J. J. Mohiuddin, B. Chu, A. Facciabene, K. Poirier, X. Wang, A. Doucette, C. Zheng, W. Xu, E. J. Anstadt, R. K. Amaravadi, G. C. Karakousis, T. C. Mitchell, A. C. Huang, J. E. Shabason, A. Lin, S. Swisher-McClure, A. Maity, L. M. Schuchter, J. N. Lukens, Association of Antibiotic Exposure With Survival and Toxicity in Patients With Melanoma Receiving Immunotherapy. *JNCI: Journal of the National Cancer Institute*. **113**, 162–170 (2021).

9. L. Derosa, B. Routy, A. Desilets, R. Daillère, S. Terrisse, G. Kroemer, L. Zitvogel, Microbiota-Centered Interventions: The Next Breakthrough in Immuno-Oncology? *Cancer Discov*. **11**, 2396–2412 (2021).

10. L. Derosa, B. Routy, A. M. Thomas, V. Iebba, G. Zalcman, S. Friard, J. Mazieres, C. Audigier-Valette, D. Moro-Sibilot, F. Goldwasser, C. A. C. Silva, S. Terrisse, M. Bonvalet, A. Scherpereel, H. Pegliasco, C. Richard, F. Ghiringhelli, A. Elkrief, A. Desilets, F. Blanc-Durand, F. Cumbo, A. Blanco, R. Boidot, S. Chevrier, R. Daillère, G. Kroemer, L. Alla, N. Pons, E. L. Chatelier, N. Galleron, H. Roume, A. Dubuisson, N. Bouchard, M. Messaoudene, D. Drubay, E. Deutsch, F. Barlesi, D. Planchard, N. Segata, S. Martinez, L. Zitvogel, J.-C. Soria, B. Besse, Intestinal Akkermansia muciniphila predicts clinical response to PD-1 blockade in advanced non-small cell lung cancer patients. *Nat Med*. **28**, 315–324 (2022).

11. L. Derosa, B. Routy, M. Fidelle, V. Iebba, L. Alla, E. Pasolli, N. Segata, A. Desnoyer, F. Pietrantonio, G. Ferrere, J.-E. Fahrner, E. Le Chatellier, N. Pons, N. Galleron, H. Roume, C. P. M. Duong, L. Mondragón, K.

Iribarren, M. Bonvalet, S. Terrisse, C. Rauber, A.-G. Goubet, R. Daillère, F. Lemaitre, A. Reni, B. Casu, M. T. Alou, C. Alves Costa Silva, D. Raoult, K. Fizazi, B. Escudier, G. Kroemer, L. Albiges, L. Zitvogel, Gut Bacteria Composition Drives Primary Resistance to Cancer Immunotherapy in Renal Cell Carcinoma Patients. *Eur Urol*. **78**, 195–206 (2020).

12. G. Gorfu, J. Rivera-Nieves, K. Ley, Role of beta7 integrins in intestinal lymphocyte homing and retention. *Curr. Mol. Med.* **9**, 836–850 (2009).

13. M. Briskin, D. Winsor-Hines, A. Shyjan, N. Cochran, S. Bloom, J. Wilson, L. M. McEvoy, E. C. Butcher, N. Kassam, C. R. Mackay, W. Newman, D. J. Ringler, Human mucosal addressin cell adhesion molecule-1 is preferentially expressed in intestinal tract and associated lymphoid tissue. *Am. J. Pathol.* **151**, 97–110 (1997).

14. H. Ogawa, D. G. Binion, J. Heidemann, M. Theriot, P. J. Fisher, N. A. Johnson, M. F. Otterson, P. Rafiee, Mechanisms of MAdCAM-1 gene expression in human intestinal microvascular endothelial cells. *Am. J. Physiol., Cell Physiol.* **288**, C272-281 (2005).

15. B. G. Feagan, P. Rutgeerts, B. E. Sands, S. Hanauer, J.-F. Colombel, W. J. Sandborn, G. Van Assche, J. Axler, H.-J. Kim, S. Danese, I. Fox, C. Milch, S. Sankoh, T. Wyant, J. Xu, A. Parikh, Vedolizumab as Induction and Maintenance Therapy for Ulcerative Colitis. *New England Journal of Medicine*. **369**, 699–710 (2013).

16. M. Hassan-Zahraee, A. Banerjee, J. B. Cheng, W. Zhang, A. Ahmad, K. Page, D. von Schack, B. Zhang, S. W. Martin, S. Nayak, P. Reddy, L. Xi, H. Neubert, M. Fernandez Ocana, K. Gorelick, R. Clare, M. Vincent, F. Cataldi, K. Hung, Anti-MAdCAM Antibody Increases ß7+ T Cells and CCR9 Gene Expression in the Peripheral Blood of Patients With Crohn's Disease. *J Crohns Colitis*. **12**, 77–86 (2018).

17. W. Reinisch, W. J. Sandborn, S. Danese, X. Hébuterne, M. Kłopocka, D. Tarabar, T. Vaňásek, M. Greguš, P. A. Hellstern, J. S. Kim, M. P. Sparrow, K. J. Gorelick, M. Hoy, M. Goetsch, C. Bliss, C. Gupta, F. Cataldi, S. Vermeire, Long-term Safety and Efficacy of the Anti-MAdCAM-1 Monoclonal Antibody Ontamalimab [SHP647] for the Treatment of Ulcerative Colitis: The Open-label Study TURANDOT II. *J Crohns Colitis*. **15**, 938–949 (2021).

18. D. R. Littman, A. Y. Rudensky, Th17 and regulatory T cells in mediating and restraining inflammation. *Cell*. **140**, 845–858 (2010).

19. P. Pandiyan, N. Bhaskaran, M. Zou, E. Schneider, S. Jayaraman, J. Huehn, Microbiome Dependent Regulation of Tregs and Th17 Cells in Mucosa. *Front Immunol*. **10**, 426 (2019).

20. C. F. Krebs, H.-J. Paust, S. Krohn, T. Koyro, S. R. Brix, J.-H. Riedel, P. Bartsch, T. Wiech, C. Meyer-Schwesinger, J. Huang, N. Fischer, P. Busch, H.-W. Mittrücker, U. Steinhoff, B. Stockinger, L. G. Perez, U. O. Wenzel, M. Janneck, O. M. Steinmetz, N. Gagliani, R. A. K. Stahl, S. Huber, J.-E. Turner, U. Panzer, Autoimmune Renal Disease Is Exacerbated by S1P-Receptor-1-Dependent Intestinal Th17 Cell Migration to the Kidney. *Immunity*. **45**, 1078–1092 (2016).

21. Y. K. Lee, J. S. Menezes, Y. Umesaki, S. K. Mazmanian, Proinflammatory T-cell responses to gut microbiota promote experimental autoimmune encephalomyelitis. *Proc Natl Acad Sci U S A*. **108 Suppl 1**, 4615–4622 (2011).

22. A. M. Magnuson, G. M. Thurber, R. H. Kohler, R. Weissleder, D. Mathis, C. Benoist, Population dynamics of islet-infiltrating cells in autoimmune diabetes. *Proc. Natl. Acad. Sci. U.S.A.* **112**, 1511–1516 (2015).

23. A. M. Morton, E. Sefik, R. Upadhyay, R. Weissleder, C. Benoist, D. Mathis, Endoscopic photoconversion reveals unexpectedly broad leukocyte trafficking to and from the gut. *Proc. Natl. Acad. Sci. U.S.A.* **111**, 6696–6701 (2014).

24. H.-J. Wu, I. I. Ivanov, J. Darce, K. Hattori, T. Shima, Y. Umesaki, D. R. Littman, C. Benoist, D. Mathis, Gut-residing segmented filamentous bacteria drive autoimmune arthritis via T helper 17 cells. *Immunity*. **32**, 815–827 (2010).

25. M. R. I. Young, Th17 Cells in Protection from Tumor or Promotion of Tumor Progression. *J Clin Cell Immunol*. **7**, 431 (2016).

26. E. Sefik, N. Geva-Zatorsky, S. Oh, L. Konnikova, D. Zemmour, A. M. McGuire, D. Burzyn, A. Ortiz-Lopez, M. Lobera, J. Yang, S. Ghosh, A. Earl, S. B. Snapper, R. Jupp, D. Kasper, D. Mathis, C. Benoist, Individual intestinal symbionts induce a distinct population of RORγ+ regulatory T cells. *Science*. **349**, 993–997 (2015).

27. N. R. Blatner, M. F. Mulcahy, K. L. Dennis, D. Scholtens, D. J. Bentrem, J. D. Phillips, S. Ham, B. P. Sandall, M. W. Khan, D. M. Mahvi, A. L. Halverson, S. J. Stryker, A.-M. Boller, A. Singal, R. K. Sneed, B. Sarraj, M. J. Ansari, M. Oft, Y. Iwakura, L. Zhou, A. Bonertz, P. Beckhove, F. Gounari, K. Khazaie, Expression of RORγt Marks a Pathogenic Regulatory T Cell Subset in Human Colon Cancer. *Science Translational Medicine*. **4**, 164ra159-164ra159 (2012).

28. A. Rizzo, M. Di Giovangiulio, C. Stolfi, E. Franzè, H.-J. Fehling, R. Carsetti, E. Giorda, A. Colantoni, A. Ortenzi, M. Rugge, C. Mescoli, G. Monteleone, M. C. Fantini, RORγt-Expressing Tregs Drive the Growth of Colitis-Associated Colorectal Cancer by Controlling IL6 in Dendritic Cells. *Cancer Immunol Res*. **6**, 1082–1092 (2018).

29. K. N. Haas, J. L. Blanchard, Reclassification of the Clostridium clostridioforme and Clostridium sphenoides clades as Enterocloster gen. nov. and Lacrimispora gen. nov., including reclassification of 15 taxa. *Int J Syst Evol Microbiol*. **70**, 23–34 (2020).

30. R. Gacesa, A. Kurilshikov, A. Vich Vila, T. Sinha, M. a. Y. Klaassen, L. A. Bolte, S. Andreu-Sánchez, L. Chen, V. Collij, S. Hu, J. a. M. Dekens, V. C. Lenters, J. R. Björk, J. C. Swarte, M. A. Swertz, B. H. Jansen, J. Gelderloos-Arends, S. Jankipersadsing, M. Hofker, R. C. H. Vermeulen, S. Sanna, H. J. M. Harmsen, C. Wijmenga, J. Fu, A. Zhernakova, R. K. Weersma, Environmental factors shaping the gut microbiome in a Dutch population. *Nature*. **604**, 732–739 (2022).

31. S. Yonekura, S. Terrisse, C. Alves Costa Silva, A. Lafarge, V. Iebba, G. Ferrere, A.-G. Goubet, J.-E. Fahrner, I. Lahmar, K. Ueda, G. Mansouri, E. Pizzato, P. Ly, M. Mazzenga, C. Thelemaque, M. Fidelle, F. Jaulin, J. Cartry, M. Deloger, M. Aglave, N. Droin, P. Opolon, A. Puget, F. Mann, M. Neunlist, A. Bessard, L. Aymeric, T. Matysiak-Budnik, J. Bosq, P. Hofman, C. P. M. Duong, S. Ugolini, V. Quiniou, S. Berrard, B. Ryffel, O. Kepp, G. Kroemer, B. Routy, L. Lordello, M.-A. Bani, N. Segata, F. Y. Yengej, H. Clevers, J.-Y. Scoazec, E. Pasolli, L. Derosa, L. Zitvogel, Cancer Induces a Stress Ileopathy Depending on β-Adrenergic Receptors and Promoting Dysbiosis that Contributes to Carcinogenesis. *Cancer Discovery*. **12**, 1128–1151 (2022).

32. A.-G. Goubet, R. Wheeler, A. Fluckiger, B. Qu, F. Lemaître, K. Iribarren, L. Mondragón, M. Tidjani Alou, E. Pizzato, S. Durand, L. Derosa, F. Aprahamian, N. Bossut, M. Moya-Nilges, D. Derrien, G. Chen, M. Leduc, A. Joseph, N. Pons, E. Le Chatelier, N. Segata, S. Yonekura, V. Iebba, O. Kepp, D. Raoult, F. André, G. Kroemer, I. G. Boneca, L. Zitvogel, R. Daillère, Multifaceted modes of action of the anticancer probiotic Enterococcus hirae. *Cell Death Differ*. **28**, 2276–2295 (2021).

33. E. N. Baruch, I. Youngster, G. Ben-Betzalel, R. Ortenberg, A. Lahat, L. Katz, K. Adler, D. Dick-Necula, S. Raskin, N. Bloch, D. Rotin, L. Anafi, C. Avivi, J. Melnichenko, Y. Steinberg-Silman, R. Mamtani, H. Harati, N. Asher, R. Shapira-Frommer, T. Brosh-Nissimov, Y. Eshet, S. Ben-Simon, O. Ziv, M. A. W. Khan, M. Amit, N. J. Ajami, I. Barshack, J. Schachter, J. A. Wargo, O. Koren, G. Markel, B. Boursi, Fecal microbiota transplant promotes response in immunotherapy-refractory melanoma patients. *Science*. **371**, 602–609 (2021).

34. D. Davar, A. K. Dzutsev, J. A. McCulloch, R. R. Rodrigues, J.-M. Chauvin, R. M. Morrison, R. N. Deblasio, C. Menna, Q. Ding, O. Pagliano, B. Zidi, S. Zhang, J. H. Badger, M. Vetizou, A. M. Cole, M. R. Fernandes,

S. Prescott, R. G. F. Costa, A. K. Balaji, A. Morgun, I. Vujkovic-Cvijin, H. Wang, A. A. Borhani, M. B. Schwartz, H. M. Dubner, S. J. Ernst, A. Rose, Y. G. Najjar, Y. Belkaid, J. M. Kirkwood, G. Trinchieri, H. M. Zarour, Fecal microbiota transplant overcomes resistance to anti–PD-1 therapy in melanoma patients. *Science*. **371**, 595–602 (2021).

35. B. Routy, V. Gopalakrishnan, R. Daillère, L. Zitvogel, J. A. Wargo, G. Kroemer, The gut microbiota influences anticancer immunosurveillance and general health. *Nat Rev Clin Oncol*. **15**, 382–396 (2018).

36. R. Y. Gao, C. T. Shearn, D. J. Orlicky, K. D. Battista, E. E. Alexeev, I. M. Cartwright, J. M. Lanis, R. E. Kostelecky, C. Ju, S. P. Colgan, B. P. Fennimore, Bile acids modulate colonic MAdCAM-1 expression in a murine model of combined cholestasis and colitis. *Mucosal Immunol*. **14**, 479–490 (2021).

37. D. V. Guzior, R. A. Quinn, Review: microbial transformations of human bile acids. *Microbiome*. **9**, 140 (2021).

38. Y. Sato, K. Atarashi, D. R. Plichta, Y. Arai, S. Sasajima, S. M. Kearney, W. Suda, K. Takeshita, T. Sasaki, S. Okamoto, A. N. Skelly, Y. Okamura, H. Vlamakis, Y. Li, T. Tanoue, H. Takei, H. Nittono, S. Narushima, J. Irie, H. Itoh, K. Moriya, Y. Sugiura, M. Suematsu, N. Moritoki, S. Shibata, D. R. Littman, M. A. Fischbach, Y. Uwamino, T. Inoue, A. Honda, M. Hattori, T. Murai, R. J. Xavier, N. Hirose, K. Honda, Novel bile acid biosynthetic pathways are enriched in the microbiome of centenarians. *Nature*. **599**, 458–464 (2021).

39. J. B. J. Ward, N. K. Lajczak, O. B. Kelly, A. M. O'Dwyer, A. K. Giddam, J. Ní Gabhann, P. Franco, M. M. Tambuwala, C. A. Jefferies, S. Keely, A. Roda, S. J. Keely, Ursodeoxycholic acid and lithocholic acid exert anti-inflammatory actions in the colon. *Am J Physiol Gastrointest Liver Physiol*. **312**, G550–G558 (2017).

40. M. Tomura, N. Yoshida, J. Tanaka, S. Karasawa, Y. Miwa, A. Miyawaki, O. Kanagawa, Monitoring cellular movement in vivo with photoconvertible fluorescence protein "Kaede" transgenic mice. *Proc. Natl. Acad. Sci. U.S.A.* **105**, 10871–10876 (2008).

41. V. Singh, S. Roth, G. Llovera, R. Sadler, D. Garzetti, B. Stecher, M. Dichgans, A. Liesz, Microbiota Dysbiosis Controls the Neuroinflammatory Response after Stroke. *J. Neurosci.* **36**, 7428–7440 (2016).

42. C. M'Rini, G. Cheng, C. Schweitzer, L. L. Cavanagh, R. T. Palframan, T. R. Mempel, R. A. Warnock, J. B. Lowe, E. J. Quackenbush, U. H. von Andrian, A novel endothelial L-selectin ligand activity in lymph node medulla that is regulated by alpha(1,3)-fucosyltransferase-IV. *J Exp Med.* **198**, 1301–1312 (2003).

43. J. Mitoma, X. Bao, B. Petryanik, P. Schaerli, J.-M. Gauguet, S.-Y. Yu, H. Kawashima, H. Saito, K. Ohtsubo, J. D. Marth, K.-H. Khoo, U. H. von Andrian, J. B. Lowe, M. Fukuda, Critical functions of N-glycans in L-selectin-mediated lymphocyte homing and recruitment. *Nat Immunol*. **8**, 409–418 (2007).

44. E. Cano-Gamez, B. Soskic, T. I. Roumeliotis, E. So, D. J. Smyth, M. Baldrighi, D. Willé, N. Nakic, J. Esparza-Gordillo, C. G. C. Larminie, P. G. Bronson, D. F. Tough, W. C. Rowan, J. S. Choudhary, G. Trynka, Single-cell transcriptomics identifies an effectorness gradient shaping the response of CD4+ T cells to cytokines. *Nat Commun*. **11**, 1801 (2020).

45. Z. T. Freeman, T. R. Nirschl, D. H. Hovelson, R. J. Johnston, J. J. Engelhardt, M. J. Selby, C. M. Kochel, R. Y. Lan, J. Zhai, A. Ghasemzadeh, A. Gupta, A. M. Skaist, S. J. Wheelan, H. Jiang, A. T. Pearson, L. A. Snyder, A. J. Korman, S. A. Tomlins, S. Yegnasubramanian, C. G. Drake, A conserved intratumoral regulatory T cell signature identifies 4-1BB as a pan-cancer target. *J Clin Invest*. **130**, 1405–1416 (2020).

46. Y. Gao, K. Deason, A. Jain, R. A. Irizarry-Caro, I. Dozmorov, L. A. Coughlin, I. Rauch, B. M. Evers, A. Y. Koh, E. K. Wakeland, C. Pasare, Transcriptional profiling identifies caspase-1 as a T cell–intrinsic regulator of Th17 differentiation. *Journal of Experimental Medicine*. **217**, e20190476 (2020).

47. Dan Lu, L. Liu, Y. Sun, J. Song, Q. Yin, G. Zhang, F. Qi, Z. Hu, Z. Yang, Z. Zhou, Y. Hu, L. Zhang, J. Ji, X. Zhao, Y. Jin, M. A. McNutt, Y. Yin, The phosphatase PAC1 acts as a T cell suppressor and attenuates host antitumor immunity. *Nat Immunol*. **21**, 287–297 (2020).

48. J.-H. Kim, J. Hwang, J. H. Jung, H.-J. Lee, D. Y. Lee, S.-H. Kim, Molecular networks of FOXP family: dual biologic functions, interplay with other molecules and clinical implications in cancer progression. *Molecular Cancer*. **18**, 180 (2019).

49. L. Li, N. Patsoukis, V. Petkova, V. A. Boussiotis, Runx1 and Runx3 are involved in the generation and function of highly suppressive IL-17-producing T regulatory cells. *PLoS One*. **7**, e45115 (2012).

50. L. Belarif, R. Danger, L. Kermarrec, V. Nerrière-Daguin, S. Pengam, T. Durand, C. Mary, E. Kerdreux, V. Gauttier, A. Kucik, V. Thepenier, J. C. Martin, C. Chang, A. Rahman, N. S.-L. Guen, C. Braudeau, A. Abidi, G. David, F. Malard, C. Takoudju, B. Martinet, N. Gérard, I. Neveu, M. Neunlist, E. Coron, T. T. MacDonald, P. Desreumaux, H.-L. Mai, S. Le Bas-Bernardet, J.-F. Mosnier, M. Merad, R. Josien, S. Brouard, J.-P. Soulillou, G. Blancho, A. Bourreille, P. Naveilhan, B. Vanhove, N. Poirier, IL-7 receptor influences anti-TNF responsiveness and T cell gut homing in inflammatory bowel disease. *J Clin Invest*. **129**, 1910–1925 (2019).

51. Y. Chen, J. Wang, X. Wang, X. Li, J. Song, J. Fang, X. Liu, T. Liu, D. Wang, Q. Li, S. Wen, D. Ma, J. Xia, L. Luo, S. G. Zheng, J. Cui, G. Zeng, L. Chen, B. Cheng, Z. Wang, Pik3ip1 Is a Negative Immune Regulator that Inhibits Antitumor T-Cell Immunity. *Clin Cancer Res*. **25**, 6180–6194 (2019).

52. J.-W. Sidhom, H. B. Larman, D. M. Pardoll, A. S. Baras, DeepTCR is a deep learning framework for revealing sequence concepts within T-cell repertoires. *Nat Commun*. **12**, 2309 (2021).

53. T. C. Wirth, H.-H. Xue, D. Rai, J. T. Sabel, T. Bair, J. T. Harty, V. P. Badovinac, Repetitive antigen stimulation induces stepwise transcriptome diversification but preserves a core signature of memory CD8(+) T cell differentiation. *Immunity*. **33**, 128–140 (2010).

54. T. Wu, Y. Ji, E. A. Moseman, H. C. Xu, M. Manglani, M. Kirby, S. M. Anderson, R. Handon, E. Kenyon, A. Elkahloun, W. Wu, P. A. Lang, L. Gattinoni, D. B. McGavern, P. L. Schwartzberg, The TCF1-Bcl6 axis counteracts type I interferon to repress exhaustion and maintain T cell stemness. *Science Immunology*. **1**, eaai8593 (2016).

55. E. J. Wherry, S.-J. Ha, S. M. Kaech, W. N. Haining, S. Sarkar, V. Kalia, S. Subramaniam, J. N. Blattman, D. L. Barber, R. Ahmed, Molecular Signature of CD8+ T Cell Exhaustion during Chronic Viral Infection. *Immunity*. **27**, 670–684 (2007).

56. K. Araki, M. Morita, A. G. Bederman, B. T. Konieczny, H. T. Kissick, N. Sonenberg, R. Ahmed, Translation is actively regulated during the differentiation of CD8+ effector T cells. *Nat Immunol*. **18**, 1046–1057 (2017).

57. C. Voigt, P. May, A. Gottschlich, A. Markota, D. Wenk, I. Gerlach, S. Voigt, G. T. Stathopoulos, K. A. M. Arendt, C. Heise, F. Rataj, K.-P. Janssen, M. Königshoff, H. Winter, I. Himsl, W. E. Thasler, M. Schnurr, S. Rothenfußer, S. Endres, S. Kobold, Cancer cells induce interleukin-22 production from memory CD4+ T cells via interleukin-1 to promote tumor growth. *PNAS*. **114**, 12994–12999 (2017).

58. T. L. Denning, G. Kim, M. Kronenberg, Cutting edge: CD4+CD25+ regulatory T cells impaired for intestinal homing can prevent colitis. *J. Immunol.* **174**, 7487–7491 (2005).

59. D. Dangaj, M. Bruand, A. J. Grimm, C. Ronet, D. Barras, P. A. Duttagupta, E. Lanitis, J. Duraiswamy, J. L. Tanyi, F. Benencia, J. Conejo-Garcia, H. R. Ramay, K. T. Montone, D. J. Powell, P. A. Gimotty, A. Facciabene, D. G. Jackson, J. S. Weber, S. J. Rodig, S. F. Hodi, L. E. Kandalaft, M. Irving, L. Zhang, P. Foukas, S. Rusakiewicz, M. Delorenzi, G. Coukos, Cooperation between Constitutive and Inducible Chemokines Enables T Cell Engraftment and Immune Attack in Solid Tumors. *Cancer Cell*. **35**, 885-900.e10 (2019).

60. A. González-Martín, L. Gómez, J. Lustgarten, E. Mira, S. Mañes, Maximal T Cell–Mediated Antitumor Responses Rely upon CCR5 Expression in Both CD4+ and CD8+ T Cells. *Cancer Res*. **71**, 5455–5466 (2011).

61. A. M. Cooper, IL-17 and anti-bacterial immunity: Protection versus tissue damage. *European Journal of Immunology*. **39**, 649–652 (2009).

62. C. Voigt, P. May, A. Gottschlich, A. Markota, D. Wenk, I. Gerlach, S. Voigt, G. T. Stathopoulos, K. A. M. Arendt, C. Heise, F. Rataj, K.-P. Janssen, M. Königshoff, H. Winter, I. Himsl, W. E. Thasler, M. Schnurr, S. Rothenfußer, S. Endres, S. Kobold, Cancer cells induce interleukin-22 production from memory CD4+ T cells via interleukin-1 to promote tumor growth. *Proceedings of the National Academy of Sciences*. **114**, 12994–12999 (2017).

63. T. Yokoo, K. Kamimura, H. Abe, Y. Kobayashi, T. Kanefuji, K. Ogawa, R. Goto, M. Oda, T. Suda, S. Terai, Liver-targeted hydrodynamic gene therapy: Recent advances in the technique. *World J Gastroenterol*. **22**, 8862–8868 (2016).

64. A. K. Holmer, R. Battat, P. S. Dulai, N. Vande Casteele, N. Nguyen, A. Jain, A. Miralles, J. Neill, H. Le, S. Singh, J. Rivera-Nieves, W. J. Sandborn, B. S. Boland, Biomarkers are associated with clinical and endoscopic outcomes with vedolizumab treatment in Crohn's disease. *Therap Adv Gastroenterol*. **13**, 1756284820971214 (2020).

65. J. Lecuelle, L. Favier, C. Fraisse, A. Lagrange, C. Kaderbhai, R. Boidot, S. Chevrier, P. Joubert, B. Routy, C. Truntzer, F. Ghiringhelli, MER4 endogenous retrovirus correlated with better efficacy of anti-PD1/PD-L1 therapy in non-small cell lung cancer. *J Immunother Cancer*. **10**, e004241 (2022).

66. L. Albiges, S. Negrier, C. Dalban, C. Chevreau, G. Gravis, S. Oudard, B. Laguerre, P. Barthelemy, D. Borchiellini, M. Gross-Goupil, L. Geoffrois, F. Rolland, A. Thiery-Vuillemin, F. Joly, S. Ladoire, F. Tantot, B. Escudier, Safety and efficacy of nivolumab in metastatic renal cell carcinoma (mRCC): Final analysis from the NIVOREN GETUG AFU 26 study. *JCO*. **37**, 542–542 (2019).

67. G. P. Sonpavde, C. N. Sternberg, Y. Loriot, A. Marabelle, J. L. Lee, A. Fléchon, G. Roubaud, D. Pouessel, V. Zagonel, F. Calabro, G. L. Banna, S. J. Shin, F. E. Vera-Badillo, T. Powles, E. Hellmis, P. A. P. Miranda, A. R. Lima, U. Emeribe, S. M. Oh, S. J. Hotte, Primary results of STRONG: An open-label, multicenter, phase 3b study of fixed-dose durvalumab monotherapy in previously treated patients with urinary tract carcinoma. *European Journal of Cancer*. **163**, 55–65 (2022).

68. A. Liesz, E. Suri-Payer, C. Veltkamp, H. Doerr, C. Sommer, S. Rivest, T. Giese, R. Veltkamp, Regulatory T cells are key cerebroprotective immunomodulators in acute experimental stroke. *Nat. Med.* **15**, 192–199 (2009).

69. C. Benakis, D. Brea, S. Caballero, G. Faraco, J. Moore, M. Murphy, G. Sita, G. Racchumi, L. Ling, E. G. Pamer, C. Iadecola, J. Anrather, Commensal microbiota affects ischemic stroke outcome by regulating intestinal γδ T cells. *Nat. Med.* **22**, 516–523 (2016).

70. R. J. Miragaia, T. Gomes, A. Chomka, L. Jardine, A. Riedel, A. N. Hegazy, N. Whibley, A. Tucci, X. Chen, I. Lindeman, G. Emerton, T. Krausgruber, J. Shields, M. Haniffa, F. Powrie, S. A. Teichmann, Single-Cell Transcriptomics of Regulatory T Cells Reveals Trajectories of Tissue Adaptation. *Immunity*. **50**, 493-504.e7 (2019).

71. A. R. Muñoz-Rojas, D. Mathis, Tissue regulatory T cells: regulatory chameleons. *Nat Rev Immunol*. **21**, 597–611 (2021).

72. N. Yosef, A. K. Shalek, J. T. Gaublomme, H. Jin, Y. Lee, A. Awasthi, C. Wu, K. Karwacz, S. Xiao, M. Jorgolli, D. Gennert, R. Satija, A. Shakya, D. Y. Lu, J. J. Trombetta, M. R. Pillai, P. J. Ratcliffe, M. L. Coleman, M. Bix, D. Tantin, H. Park, V. K. Kuchroo, A. Regev, Dynamic regulatory network controlling Th17 cell differentiation. *Nature*. **496**, 461–468 (2013).

73. U. U. Uche, A. R. Piccirillo, S. Kataoka, S. J. Grebinoski, L. M. D'Cruz, L. P. Kane, PIK3IP1/TrIP restricts activation of T cells through inhibition of PI3K/Akt. *J Exp Med*. **215**, 3165–3179 (2018).

74. A. Fischer, S. Zundler, R. Atreya, T. Rath, C. Voskens, S. Hirschmann, R. López-Posadas, A. Watson, C. Becker, G. Schuler, C. Neufert, I. Atreya, M. F. Neurath, Differential effects of α4β7 and GPR15 on homing of effector and regulatory T cells from patients with UC to the inflamed gut in vivo. *Gut*. **65**, 1642–1664 (2016).

75. G. D'Haens, S. Vermeire, H. Vogelsang, M. Allez, P. Desreumaux, A. Van Gossum, W. J. Sandborn, D. C. Baumgart, R. M. Ransohoff, G. M. Comer, A. Ahmad, F. Cataldi, J. Cheng, R. Clare, K. J. Gorelick, A. Kaminski, V. Pradhan, S. Rivers, M. O. Sikpi, Y. Zhang, M. Hassan-Zahraee, W. Reinisch, O. Stuve, Effect of PF-00547659 on Central Nervous System Immune Surveillance and Circulating β7+ T Cells in Crohn's Disease: Report of the TOSCA Study. *J Crohns Colitis*. **12**, 188–196 (2018).

76. G. Calenda, R. Keawvichit, G. Arrode-Brusés, K. Pattanapanyasat, I. Frank, S. N. Byrareddy, J. Arthos, C. Cicala, B. Grasperge, J. L. Blanchard, A. Gettie, K. A. Reimann, A. A. Ansari, E. Martinelli, Integrin α4β7 Blockade Preferentially Impacts CCR6+ Lymphocyte Subsets in Blood and Mucosal Tissues of Naive Rhesus Macaques. *J. Immunol.* **200**, 810–820 (2018).

77. M. I. Love, W. Huber, S. Anders, Moderated estimation of fold change and dispersion for RNA-seq data with DESeq2. *Genome Biol*. **15**, 550 (2014).

78. M. E. Ritchie, B. Phipson, D. Wu, Y. Hu, C. W. Law, W. Shi, G. K. Smyth, limma powers differential expression analyses for RNA-sequencing and microarray studies. *Nucleic Acids Res*. **43**, e47 (2015).

79. H. Lin, S. D. Peddada, Analysis of compositions of microbiomes with bias correction. *Nat Commun*. **11**, 3514 (2020).

80. H. Mallick, A. Rahnavard, L. J. McIver, S. Ma, Y. Zhang, L. H. Nguyen, T. L. Tickle, G. Weingart, B. Ren, E. H. Schwager, S. Chatterjee, K. N. Thompson, J. E. Wilkinson, A. Subramanian, Y. Lu, L. Waldron, J. N. Paulson, E. A. Franzosa, H. C. Bravo, C. Huttenhower, Multivariable association discovery in population-scale meta-omics studies. *PLoS Comput Biol*. **17**, e1009442 (2021).

81. N. Segata, J. Izard, L. Waldron, D. Gevers, L. Miropolsky, W. S. Garrett, C. Huttenhower, Metagenomic biomarker discovery and explanation. *Genome Biol*. **12**, R60 (2011).

82. P. Bankhead, M. B. Loughrey, J. A. Fernández, Y. Dombrowski, D. G. McArt, P. D. Dunne, S. McQuaid, R. T. Gray, L. J. Murray, H. G. Coleman, J. A. James, M. Salto-Tellez, P. W. Hamilton, QuPath: Open source software for digital pathology image analysis. *Sci Rep*. **7**, 16878 (2017).

83. C. Grajeda-Iglesias, S. Durand, R. Daillère, K. Iribarren, F. Lemaitre, L. Derosa, F. Aprahamian, N. Bossut, N. Nirmalathasan, F. Madeo, L. Zitvogel, G. Kroemer, Oral administration of Akkermansia muciniphila elevates systemic antiaging and anticancer metabolites. *Aging (Albany NY)*. **13**, 6375–6405 (2021).

84. S. Durand, C. Grajeda-Iglesias, F. Aprahamian, N. Nirmalathasan, O. Kepp, G. Kroemer, "Chapter 11 - The intracellular metabolome of starving cells" in *Methods in Cell Biology*, O. Kepp, L. Galluzzi, Eds. (Academic Press, 2021; https://www.sciencedirect.com/science/article/pii/S0091679X21000431), vol. 164 of *Monitoring vesicular trafficking in cellular responses to stress - Part A*, pp. 137–156.

Acknowledgments: We would like to particularly thank the animal facility, the Flow cytometry and Pathology Platforms of Gustave Roussy, especially Dr. P. Gonin, L. Touchard, C. Metereau, A. Noel, and O. Bawa. We would like to thank the PREMIS operational team, especially S. Farhane (Project leader), S. Messayke (Pharmacovigilance), L. Bedouda (Clinical Research Associate), R. Chaabane (Clinical Research Associate), C. Mohamed-Djalim (Clinical Research Associate), and all investigators. The Bladder Cohort from IOPREDI ancillary study / STRONG study (NCT03084471) was funded by AstraZeneca. Some figure items were partly generated using Servier Medical Art, provided by Servier, licensed under a Creative Commons Attribution 3.0 unported license. **Funding**: This work was supported by SEERAVE Foundation, European Union Horizon 2020, Project Number 825410 and Project Acronym ONCOBIOME, Institut National du Cancer (INCa), ANR Ileobiome – 19-CE15-0029-01, ANR RHU5 "ANR-21-RHUS-0017" IMMUNOLIFE", MAdCAM INCA_ 16698, ANR-IHU Méditerranée-Infections, Ligue contre le cancer, LABEX OncoImmunology, la direction generale de l'offre de soins (DGOS), SIRIC SOCRATE (INCa/DGOS/INSERM 6043), and PACRI network. G.K. was supported by the Ligue contre le Cancer (équipe labellisée); Agence National de la Recherche (ANR) – Projets blancs; AMMICa US23/CNRS UMS3655; Cancéropôle Ile-de-France; Fondation pour la Recherche Médicale (FRM); Equipex Onco-Pheno-Screen; European Joint Programme on Rare Diseases (EJPRD); European Research Council (ICD-Cancer), European Union Horizon 2020 program Crimson; Institut National du Cancer (INCa); Institut Universitaire de France; LabEx Immuno-Oncology (ANR-18-IDEX-0001); a Cancer Research ASPIRE Award from the Mark Foundation; SIRIC Stratified Oncology Cell DNA Repair and Tumor Immune Elimination (SOCRATE); and SIRIC Cancer Research and Personalized Medicine (CARPEM). This study contributes to the IdEx Université de Paris ANR-18-IDEX-0001. M.F. was funded by SEERAVE Foundation. C.Ra. received a fellowship from Immuntrain within the Marie-Slodowska Curie Training network of the European Union (LMU Klinikum). L.D., B.R., S.Y., and F.X.D. were supported by Philantropia at Gustave Roussy Foundation. I.La was funded by Fondation pour la Recherche Médicale (FRM). This work is supported by the Prism project funded by the Agence Nationale de la Recherche under grant number ANR-18-IBHU-0002. This work was funded by the TriPoD European Research Council Advanced EU (322856) and Recherche Hospitalo-Universitaire iMAP (ANR-16-RHUS-0001) grants to D.K. O.K. was funded by INCA and the DIM Elicit. The PREMIS study was funded by Gustave Roussy fondation & Malakoff Humanis. A.Sc. and N.W. were funded by DFG (German Research Foundation) – Project-ID 403324012 – SFB 1382.
Author contributions: Conceptualization: L.Zi., G.K., C.Ra., and M.F. **Methodology**: M.F., C.Ra., A.L.T., I.La., L.Zh., I.Le., A.Si., F.Gi., S.Y., O.K., A.Sc., N.W., J.S.G., S.K., J.B., L.L., N.Ga., B.Q., E.L.C., L.B., J.P.G., R.D., C.Tr., F.Gh., V.M., D.K., A.M.T., N.S., G.K., and L.Zi. **Software**: M.F., I.La., C.D., K.M., C.Ri., G.V., V.M., D.D., and A.M.T. **Validation**: M.F., C.Ra., C.A.C.S. and L.D. **Formal analysis**: M.F., C.Ra., C.A.C.S., I.La., C.D., M.L., S.D., K.M., S.Y., J.E.F., C.Ri., L.L., G.V., E.L.C., R.D., V.M., D.D., A.M.T., and L.D. **Investigation**: M.F., C.Ra., C.A.C.S., A.L.T., I.La., A.L.M.L.V., L.Zh., C.Th., I.Le., M.M., E.P., R.B., M.D.M.F., S.Z., A.R., M.L., G.F., P.L., A.Si., K.M., C.A.D., M.P.R., M.T.A., J.C., J.B., L.L., R.D., C.Tr., N.C., V.M., L.D., G.K., and L.Zi. **Resources**: A.Si., K.M., C.A.D., F.Gi., M.P.R., S.T., A.Sc., N.W., J.S.G., S.K., E.L.C., L.B., J.P.G., A.J., N.Ge., E.G., N.L., R.K., R.D., B.B., C.Tr., F.Gh., N.C., V.M., D.K., L.A., A.M.T., N.S., F.X.D., A.M., B.R., L.D., G.K., and L.Zi. **Data Curation**: I.La., K.M., G.V., V.M., and A.M.T. **Writing - Original Draft**: L.Zi., G.K., C.Ra., and M.F. **Writing - Review & Editing:** L.Zi., G.K., C.Ra, M.F., C.A.C.S., D.D., A.L.T., M.P.R., O.K., E.G., N.L., V.M., and L.D. **Visualization**: M.F., C.Ra, C.A.C.S., A.L.T., I.La., A.L.M.L.V., R.B., and L.D. **Supervision**: L.Zi., G.K., M.F., C.Ra., L.D., F.Gi., O.K., E.L.C., N.L., D.K., and N.S. **Funding acquisition**: L.Zi., G.K., and L.D. **Competing interests:** L.Zi. founded everImmune and is the SAB president

of everImmune. L.Zi. had grant support from Daichi Sankyo, Kaleido, 9 meters, and Pileje. G.K. holds research contracts with Daiichi Sankyo, Eleor, Kaleido, Lytix Pharma, PharmaMar, Osasuna Therapeutics, Samsara Therapeutics, Sanofi, Tollys, and Vascage. G.K. has consulted for Reithera. G.K. is on the Board of Directors of the Bristol Myers Squibb Foundation France. G.K. is a scientific co-founder of everImmune, Osasuna Therapeutics, Samsara Therapeutics, and Therafast Bio. GK is in the scientific advisory boards of Hevolution, Institut Servier and Longevity Vision Funds. GK is the inventor of patents covering therapeutic targeting of aging, cancer, cystic fibrosis and metabolic disorders. Among these, patents were licensed to Bayer (WO2014020041-A1, WO2014020043-A1), Bristoll-Myers Squibb (WO2008057863-A1), Osasuna Therapeutics (WO2019057742A1), PharmaMar (WO2022049270A1 and WO2022048775-A1), Raptor Pharmaceuticals (EP2664326-A1), Samsara Therapeutics (GB202017553D0), and Therafast Bio (EP3684471A1). R.D filed the "WO2022/268841 A1"patent. O.K. is a scientific cofounder of Samsara Therapeutics. L.D. is member of the SAB of everImmune. L.A. is an advisor or consultant for Astellas, BMS, Ipsen, Janssen, MSD, Pfizer, EISAI, and Roche. Gustave Roussy filed a patent with Registration number EP21305846.4 and Reference B210162EPA/VEM/CPO “Methods for diagnosing a cancer-induced ileopathy and their use for improving cancer treatment by immunotherapy” licensed to everImmune. **Data and materials availability**: The raw data that support the findings of this study are available on request from the corresponding author (L.Zi.). Patient data are not publicly available except to vetted researchers and not to the broader public via a data transfer agreement (DTA). An MTA will be necessary to access to intestinal species from everImmune or Gustave Roussy. Bulk RNA-Seq data (E-MTAB-12787), single-cell Rhapsody RNA-Seq data (E-MTAB-12784), 16S rRNA sequencing data (E-MTAB-12812), 10X single cell RNA and TCR sequencing data (E-MTAB-12846), metagenomics data (bioprojects PRJNA944152 and PRJNA751792), and metabolomics data (Elsevier / Mendeley Data - DOI: 10.17632/4b76mz87r6.1) are all publicly available .

Figure Legends

Fig. 1. Broad-spectrum ABX downregulate MAdCAM-1 expression in the murine ileal vasculature. (**A to D**) Relative transcription (**A**) and protein (**B to D**) levels of *Madcam1* gene product obtained with RT-qPCR (**A**), immunohistochemistry staining of MAdCAM-1 in ileal lamina propria (ILP) venules and high endothelial venules in Peyer's patches in ACS-treated and untreated mice (as indicated above micrograph pictures) (Scale bar: 200 µm, 100 µm, and 40 µm, respectively) (**B**), flow cytometry gating on $CD45^-$ cells of ILP (**C**), or ELISA (**D**) of ileal (A to D) or colonic (A) tissues in C57BL/6 mice after continuous broad-spectrum antibiotics (ACS: ampicillin, colistin, streptomycin) or after a 4- or 12-day spontaneous recolonization (ACS+4d or ACS+12d) following cessation of ACS. Each dot represents one ileum (A to D) or colon (A). N=2 (A) or 3 (B to D). (**E**) Quantitative RT-qPCR of relative *Madcam1* gene expression normalized on the naive specific-pathogen-free (SPF) mice group in ileal mucosae of C57BL/6 mice reared in SPF conditions (no ABX conditioning) which underwent oral gavage with bacteria spp. aligned on the *x*-axis (N=4). (*Akk.*, *Akkermansia muciniphila*; *E. hirae*, *Enterococcus hirae*; *E. clostri*, *Enterocloster clostridioformis*) (**F**) The same experiments as in (C) performing flow cytometric analysis of ILP $CD4^+$ T cell subsets ($\alpha4\beta7^+$ vs $CD25^+$ $FoxP3^+$ Treg cells vs $ROR\gamma t^+$ $CD4^+$ Th17 cells) during continuous ACS or at the ACS+4d phase, each dot representing one ileum. (**G**) Ileal expression levels of *Foxp3* in *Madcam1* gene-deficient mice (left) or phenocopied with an anti-MAdCAM-1 Ab (right) (treated (full dots) or not with anti-PD-1 Ab that did not impact on ileal *Madcam1* expression levels, not shown) without ATB conditioning. Each dot represents the RT-qPCR data of one ileum (n=6 mice per group per experiment). Panel A, E, and G depict a pool of 2-3 independent experiments. Results from a representative experiment are shown in panel B, C, D and F. Comparisons between groups were analyzed using nonparametric Mann–Whitney *U* test (2 groups) or Kruskal–Wallis *H* test (>2 groups) followed by multiple-comparisons test by controlling the FDR. Error bars represent means ± SEM.

Fig. 2. Downregulation of ileal *Madcam1* gene expression in patients taking ABX.

(**A and B)** RT-qPCR-based transcriptional levels of human *MADCAM1* (**A**) and *RORC* genes (**B**) in intestinal biopsies collected during endoscopic intervention in 21 control (ABX-free) patients and 10 ABX-treated patients (**table S2**). Each dot represents one biopsy either from ileum, caecum and colon, a single patient being represented one to three times. (**C**) Spearman correlation between ileal *IL17A* and *MADCAM1* gene expressions in ABX-treated or untreated patients. (**D**) Impact of

fecal microbiota transplantation (FMT) in 3 days-ABX-treated recipient mice using feces from NSCLC patients at diagnosis (prior to PD-1 blockade) (**table S3**) on ileal *Madcam1* gene expression normalized on the SPF (FMT "–") mice group (log10 axis (D, left panel). Each experiment used a different FMT donor, 6 times independenly and comprised 6-10 animals per group. Each dot represents one ileum. Non supervised hierarchical clustering of the taxonomic composition of human donor feces (defined using shotgun MG sequencing), selecting bacteria of high prevalence >25% and clinically relevant (*10*) (D, middle panel) and volcano plot contrasting significantly different stool taxa of FMT-recipient mice, as assessed using 16S rRNA-Seq, selecting bacteria of high prevalence and, according to ileal expression levels of *Madcam1* (right panel). "Norm": normal levels of MAdCAM-1 (in SPF controls). (**E**) Shotgun metagenomics-based determination of the relative abundance of fecal species significantly affected by the ABX uptake in lung cancer patients during ABX versus >60 days after ABX discontinuation in a paired analysis including n=13 individuals (fpkm: Fragments per kilo base of transcript per million mapped fragments (gene expression unit). Comparisons between groups were analyzed using nonparametric Mann–Whitney *U* test (2 groups) or Kruskal–Wallis *H* test (>2 groups) followed by multiple-comparisons test by controlling the FDR. For C, nonparametric Spearman correlation was performed. For volcano plot in D, a linear regression was performed to assess *Madcam1* expression as a function of bacteria prevalence in mouse feces and FDR correction was applied. For E, nonparametric Wilcoxon matched-pairs signed rank test was performed. Error bars represent means ± SEM.

Fig. 3. ABX-induced exodus of enterotropic α4β7$^+$ Tr17 cells towards tumor beds.

(**A**) Flow cytometric analysis of α4β7 expression in PC$^–$ or PC$^+$ CD4$^+$ T cells residing in the tdLNs or tumor bed in Kaede mice UV illuminated in the ileum or the "intestine" (ileum+caecum+mLNs). (**B**) The same as in (A) but in WT mice subjected to CFSE injection in the mLNs and gating on CFSE$^–$ or CFSE$^+$ CD4$^+$ T cells. (**C**) Volcano plot depicting the differential gene transcription in bulk RNA-Seq of α4β7^{hi} versus α4β7$^–$ CD4$^+$ lymphocytes cell-sorted from mLNs in four MCA205 tumor-bearing animals. Volcano plots were generated computing the log2 of fold change ratio (FC) of the mean relative abundances of transcripts in α4β7^{hi} versus α4β7$^–$ CD4$^+$ lymphocytes (*x*-axis) with the co-log10 of *P*-values deriving from Mann–Whitney *U* test for each transcript followed by multiple-comparisons test by controlling the FDR. Blue and orange dots are considered significant ($P<0.05$), whereas back dots are not ($P>0.05$) (**data S1**). (**D to F**)

Representative gating strategy and dot plots in flow cytometric analyses of the IL-17A secreting α4β7^{+} Treg (FoxP3^{+} CD25^{+}) or α4β7^{+} Tconv (FoxP3^{-}) CD4^{+} T cells within CFSE^{+} (originating from the mLNs, green dots) or CFSE^{-} cells (tdLNs resident cells, black dots) reaching the tdLNs during the ACS+4d phase (n=10-16 mice per group) (**D and E**). (**F**) Flow cytometric determination of CFSE^{+} Treg cells reaching the tdLNs (left panel) or the contralateral LN (cLN, right panel) in day 7-established MCA205 bearing WT versus *Madcam1*$^{-/-}$ mice (not treated with ACS), 24 hours after CFSE injection in mLNs. Each dot represents one mouse. (**G**) The same as in (F) but in Kaede tumor-bearing mice treated or not with anti-MAdCAM-1 Ab (day 8 post-tumor inoculation), photoconverted at day 10 where flow cytometry at day 11 could identify Treg-like cells using membrane staining for CD25^{hi}. Each dot represents one mouse. (**H**) Flow cytometric phenotyping of T cells from tdLNs in tumor-bearing mice at day 11 post-MCA205 inoculation, gavaged with *E. clostridioformis* (*E. clostri*) at day 8, photoconverted in the ileum at day 10. The percentages of CXCR6^{+}CXCR3^{-} cells in CD4^{+} T cells expressing high levels of CD25 (Tr17-like, left panel) or CD25^{-} (right panel) in Kaede mice within PC^{+} (originating from the mLNs) or PC^{-} cells (tdLNs resident cells) reaching the tdLNs during the colonization phase with *E. clostridioformis*. Panel A, B, E and H depicts a pool of 3 to 5 independent experiments containing 5 mice per group. Results from a representative experiment is shown in panel C, D, and F. Each dot represents one mouse. Comparisons between groups were analyzed using nonparametric Mann–Whitney *U* test (2 groups) or Kruskal–Wallis *H* test (>2 groups) followed by multiple-comparisons test by controlling the FDR. For PC^{+} vs PC^{-} or CFSE^{+} vs CFSE^{-} comparisons, Wilcoxon matched-pairs signed rank test were performed. Error bars represent mean ± SEM.

Fig. 4. Clonal and functional patterns of emigrating Treg cells according to locations.

(**A**) Single-cell sorting and RNA-Seq in tumor bearers 11 days after MCA205 implantation using 10X Genomics technology to characterize phenotypic traits of CFSE^{+} CD4^{+} and CD8^{+} T cell subsets emigrating from mLNs (CFSE injection at day 10) and reaching tdLNs, cLNs, or tumor beds, or recovered in mLNs after oral gavage with water or *E. clostridioformis* (*E. clostri*) at day 5 and day 7. Determination of CFSE^{+} mLNs cells emigrating from the gut to the tdLNs or tumor beds (upper and lower panels respectively) by flow cytometry, according to oral gavage with *E. clostridioformis*, depicted in proportions of all CFSE^{+} cells. (**B**) Single-cell RNA-Seq and cell clustering by mean of *t*-distributed stochastic neighbor embedding (tSNE) of CFSE^{+} mLNs T cells recovered in mLNs, cLN, tdLNs and tumor bed 24 hours post inoculation of CFSE in mLNs

according to transcriptomics patterns. (**C**) Single-cell TCR sequencing was performed on CFSE-stained lymphocytes sampled from the mLNs, the cLN, the tumor, or the tdLNs. Clones were divided into fractions based on their occurrence in the repertoire (clones with an occurrence of one are represented in gray, and ones with counts higher than one in blue. The cumulative frequency of each fraction was calculated within the repertoire of each sample**.** Cumulative frequencies in FoxP3^{+}CD127^{-} (upper panels) and FoxP3^{-} (lower panels) CD4^{+} T cells according to location are depicted. (**D**) TCRs from mLNs or pooled tumor and tdLNs (tumor/tdLNs) were clustered with DeepTCR, generating clusters of paired TRA-TRB clonotypes with shared specificities. Clusters were assigned as being mLNs (purple), tumor/tdLNs (grey) or shared (yellow) based on the percentage of clonotypes composing them. Proportion of mLNs, tumor/tdLNs and shared clusters in control (water) and *E. clostridioformis*-gavaged mice (left panel), and within Treg and conventional CD4^{+} T cells (middle and right panels). (**E**) Volcano plot of differentially expressed genes in CFSE^{+} FoxP3^{+} CD127^{-} CD4^{+} T cells in tumors versus mLNs (orange versus blue in *x*-axis), in water versus *E. clostridioformis*-treated groups (left and right panels, respectively) (**Data S2**). (**F**) Venn diagram comparing control and *E. clostridioformis*-treated groups for genes upregulated in the tumor (versus mLNs), highlighting in orange, only those upregulated in *E.clostridioformis*-treated mice (**Data S2**). Also refer to **fig. S8A** for detailed CD4^{+} T cell phenotypes and subsets, and **fig. S8B, D** and **E** for CD8^{+} T cell counterparts. Panel A depicts a pool of 2 independent experiments containing 6 mice per group. Sequencing data (B to F) have been performed once.

Fig. 5. Disruption of the MAdCAM-1/ α4β7 axis induced maladaptive responses to anti-PD-1 Abs in mice. (**A**) Tumor growth kinetics of subcutaneous MCA205 (syngeneic of C57BL/6) implanted in wild-type (WT) versus *Itgb7*- or *Madcam1*-deficient mice. (**B to D**) Tumor growth kinetics or whole-body luminescence-based imaging after implantation of subcutaneous (s.c) MCA205 syngeneic of C57BL/6 (**B**), mammary 4T1 syngeneic of BALB/c (**C**) and orthotopic luciferase-expressing lung TC-1-luc cancer syngeneic of C57BL/6 (**D**) in animals treated with isotype control, anti-α4β7 mAb or anti-MAdCAM-1 mAb while receiving anti-PD-1 therapeutic antibodies (or isotype control Abs). For D, ratios between pre- and post-PD-1 blockade with isotype control mAb, anti-α4β7 mAb or anti-MAdCAM-1 mAb were calculated. Mean±SEM of tumor sizes among five to six mice per group overtime in two treatment groups (anti-PD-1 versus

isotype control Ab). (**E**) Flow cytometric analysis of α4β7 expression on $CD4^+$ T cell splenocytes and tumor-infiltrating lymphocytes (TILs) in WT versus *Madcam1*-deficient mice. Each dot represents one mouse. (**F to H**) Intracellular flow cytometric analysis of RORγt expression in $\alpha4\beta7^+$ or total $CD25^+$ $FoxP3^+$ Treg TILs in anti-MAdCAM-1 or isotype control Ab-treated mice (**F**) or in WT MCA205 tumor bearing mice receiving ACS conditioning regimen (four days post-ACS stop (ACS+4d) or twelve days post-ACS stop (ACS+12d) treated or not with anti-PD-1 Abs (**G and H**). (**I**) Flow cytometric analyses of tumor infiltrating cells (TILs) for $CCR5^+$ $CD8^+$ effector T cells in s.c. MCA205 tumor-bearing mice treated with isotype control mAb, anti-α4β7 mAb or anti-MAdCAM-1 mAb in the setting of PD-1 blockade. (**J**) 4T1 WT or 4T1 *Il22ra1*$^{-/-}$ tumor cell lines were inoculated s.c three days after start of ACS antibiotics that were pursued for 4 days. At ACS discontinuation (after 7 days), neutralizing anti-PD-1 and anti-IL-17A Abs (or isotype control Abs) were i.p injected every 3 days for 5 times until day 12. Tumor sizes of s.c. 4T1 WT or 4T1 *Il22ra1*$^{-/-}$ tumors at sacrifice. In each experiment, four or five anti-PD-1 i.p. injections were administered every three days during the ACS+12d phase. Results from a representative experiment are depicted in panel A to D, F and H. Graphs in E, I and J pooled the data of two experiments. Each experiment comprised five to eight mice per group and was performed independently 2-4 times leading to similar conclusions. Each dot represents one mouse. Comparisons between groups were analyzed using nonparametric Mann–Whitney *U* test (2 groups) or Kruskal–Wallis *H* test (>2 groups) followed by multiple-comparisons test by controlling the FDR. Error bars represent mean ± SEM.

Fig. 6. Interception of immunosuppressive T cells by transfection-enforced overexpression of MAdCAM-1 in the liver. Rapid hydrodynamic iv injection of *Madcam1*-encoding cDNA subcloned into a pLIVE plasmid vector ("plasmid+") or vector alone ("plasmid−") into day 5 tumor-bearing mice, preconditioned with ACS for 3-4 days (or water, from day −3 to day +5)) and treated (**G to J**) or not (**A to F**) with 4 i.p inoculations of anti-PD-1 Ab from day 6 to day 14. (**A and B**) Liver expression of *Madcam1* mRNA (**A**) or MAdCAM-1 protein (**B**) (assessed in RT-qPCR (**A**) or immunohistochemistry (IHC) (**B**) according to plasmid inoculation and ACS treatment. One representative micrograph picture is shown for IHC (scale bar: 40 μm) (**B, left**). (**C**) Spearman correlations between liver *Foxp3*/FoxP3 (in RT-qPCR (**left**), in IHC (**right**)) and *Madcam1* mRNA (RT-qPCR) relative expression in plasmid-treated mice. (**D and E**) Flow

cytometric analysis of $\alpha4\beta7^+$ (**D**) or $\alpha4\beta7^-$ (**E**) Treg in water or ACS-treated mice according to *Madcam1*-encoding cDNA plasmid injection (or control vector). Concatenated mean±SEM percentages of stained T cells. (**F**) Spearman correlation between liver *Foxp3* in RT-qPCR after normalization of relative expression (*z*-score), and tumor size at sacrifice (D14). (**G and H**) Liver expression of *Rorc* and *Madcam1* relative gene expression in RT-qPCR according to PD-1 blockade and *Madcam1*-encoding cDNA plasmid injection (or control vector) as well as ACS (or water). (**H**) Spearman correlations between liver *Rorc* and *Madcam1* relative gene expression in RT-qPCR in plasmid-treated mice. (**I and J**) Tumor size in MCA205 bearing-animals treated with anti-PD-1 Abs in water or ACS-treated mice according to *Madcam1*-encoding cDNA plasmid injection (or control vector) (**I, left panel**). Tumor growth kinetics in MCA205 bearing-animals treated with anti-PD-1 Abs with or without ACS in animals inoculated with the vector alone or the *Madcam1*-encoding cDNA plasmid (**I, right panel**). (**J**) Spearman correlations between liver *Madcam1* relative expression in RT-qPCR and tumor size at sacrifice (D19), in plasmid-treated mice. Except for B showing a representative experiment, graphs depict the data pooled from two independent experiments containing 6 to 10 mice per group. Each dot represents one mouse, black and red dots for water or ACS-treated animals respectively. Comparisons between groups were analyzed using nonparametric Mann–Whitney *U* test (2 groups) or Kruskal–Wallis *H* test (>2 groups) followed by multiple-comparisons test for controlling the FDR and nonparametric Spearman correlations. Error bars represent means ± SEM.

Fig. 7. Serum soluble MAdCAM-1 is a robust prognosis parameter in cancer patients.
(**A**) Luminex immunoassay monitoring of serum levels of soluble MAdCAM-1 (sMAdCAM-1) in 299 NSCLC patients belonging to two independent cohorts according to history of recent ABX uptake (**table S5 and S7**). Each dot represents one patient's serum. Error bars represent means ± SEM. (**B to D**) Overall survival (OS) analysis using the Kaplan Meier estimator and Cox regression to assess the prognostic value of serum levels of sMAdCAM-1, split using the median of the NSCLC patient discovery cohort amenable to PD-1 blockade, according to ABX uptake history (**B**). This cut-off determined from the discovery cohort allowed to split the patients in two groups of different prognosis in the validation cohort (**C**). (**D**) Idem as in (C) combining both cohorts of NSCLC and segregating patients according to tumor PD-L1 expression and the cut-off value of sMAdCAM-1 (median of the discovery cohort) (see also **table S5** for patient description, **table S6** for multivariable analysis, and **fig. S10D-E** for PFS). (**E**) The same as in (C) but overall survival

in 212 in second or third line metastatic renal cell carcinoma (RCC) patients amenable to nivolumab. (**F**) The same as in (C) but overall survival in 79 patients diagnosed with metastatic bladder cancer (BC) treated with durvalumab (anti-PD-L1). Kaplan–Meier overall survival (OS) curves were generated and hazard ratios (HRs) are indicated.

Fig. 8. **Serum sMAdCAM-1 is a proxy for gut dysbiosis.**

(**A and B**) Alpha (**A**) and beta (**B**) diversity of the taxonomic content of the intestinal microbiota according to the serum sMAdCAM-1 levels in 95 NSCLC patients. (**A**) MGS Shannon diversity evaluation in shotgun MG sequencing according to the median of sMAdCAM-1 in the whole population composed of 95 NSCLC patients (refer to **table S7** for patient description). The *P*-value was calculated by a Wilcoxon test blocking for cohort. (**B**) Principal-component analysis (PCA) of species level centered log-ratio-transformed relative abundance. The *P*-value was calculated using ADONIS and 999 permutations. (**C**) Differentially abundant species according to sMAdCAM-1 serum levels (< (Low) or ≥ (High) according to median), color coded according to the relative abundance of each species detected by at least three different methods. (**D**) Relative abundances of two distinct species from the genus *Enterocloster*, categorizing the patients according to the median of sMAdCAM-1. Each dot represents each patient's stool. Comparisons between groups were analyzed using the nonparametric Mann–Whitney *U* test (2 groups). Error bars represent means ± SEM.

Supplementary Materials

Figs. S1 to S10

Tables S1 to S9

Data S1 and Data S2

Figure 1

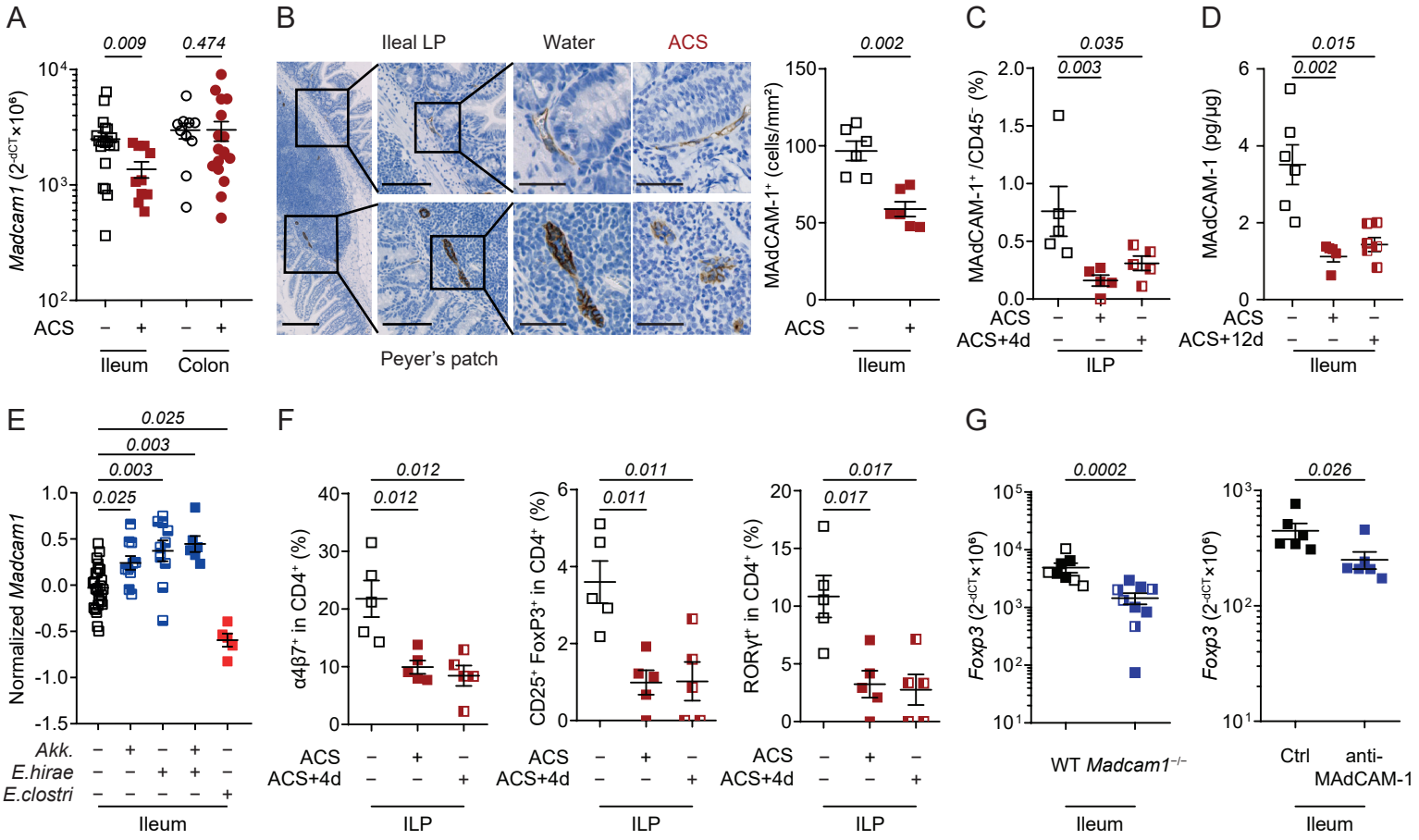
A
B
C
D
Ileal LP
Water
ACS
Peyer's patch
Ileum
Colon
ILP
ACS
ACS+4d
ACS+12d

E
F
G
Akk.
E.hirae
E.clostri
Ileum
ILP
WT Madcam1−/−
Ctrl
anti-MAdCAM-1

Figure 2

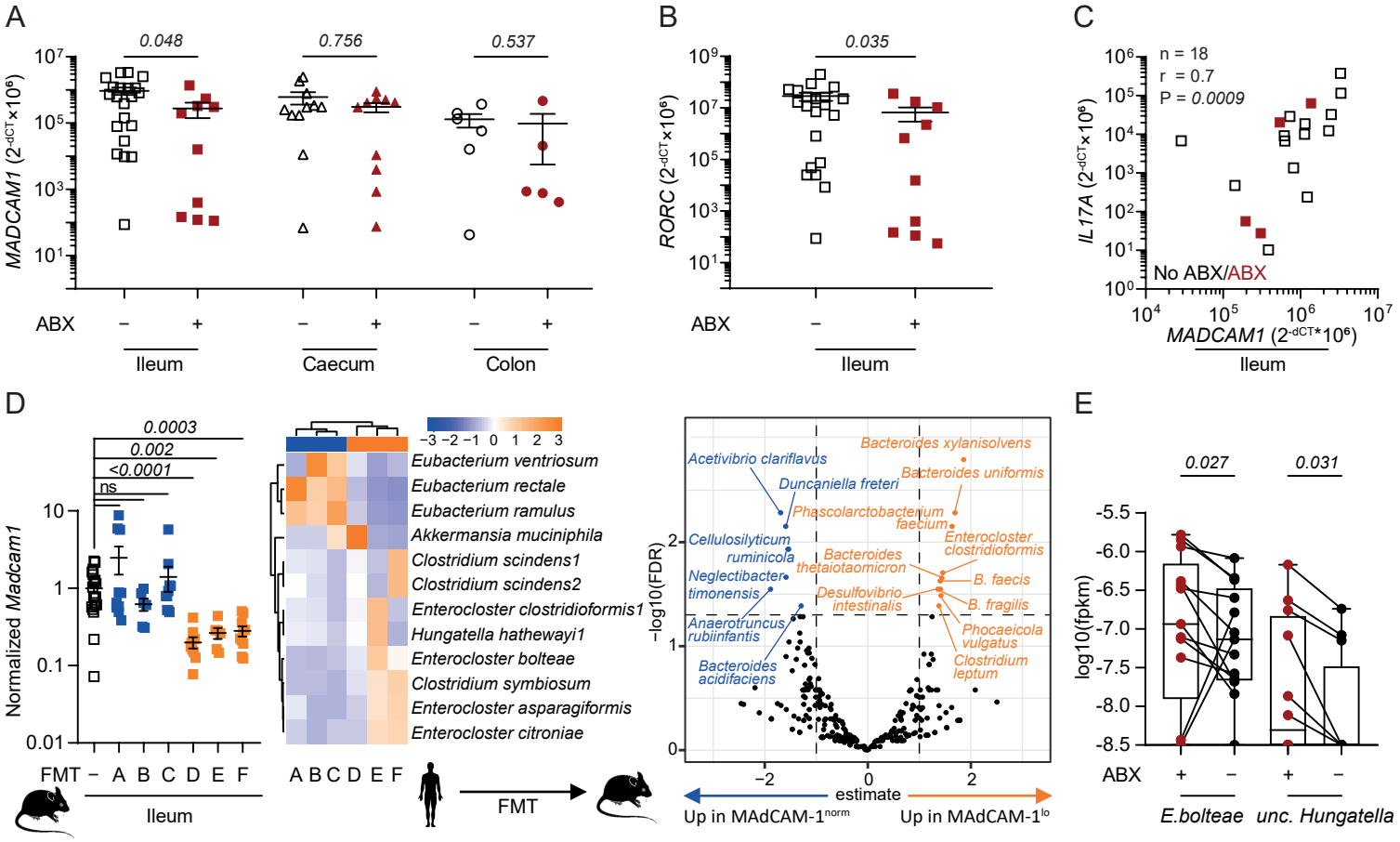
A
0.048
0.756
0.537
MADCAM1 (2-dCT×10⁶)
ABX
Ileum
Caecum
Colon
B
0.035
RORC (2-dCT×10⁶)
Ileum
C
n = 18
r = 0.7
P = 0.0009
IL17A (2-dCT×10⁶)
No ABX/ABX
MADCAM1 (2-dCT*10⁶)
Ileum
D
0.0003
0.002
<0.0001
ns
Normalized Madcam1
FMT
Ileum
Eubacterium ventriosum
Eubacterium rectale
Eubacterium ramulus
Akkermansia muciniphila
Clostridium scindens1
Clostridium scindens2
Enterocloster clostridioformis1
Hungatella hathewayi1
Enterocloster bolteae
Clostridium symbiosum
Enterocloster asparagiformis
Enterocloster citroniae
FMT
Acetivibrio clariflavus
Duncaniella freteri
Phascolarctobacterium faecium
Cellulosilyticum ruminicola
Neglectibacter timonensis
Anaerotruncus rubiinfantis
Bacteroides acidifaciens
Bacteroides xylanisolvens
Bacteroides uniformis
Enterocloster clostridioformis
Bacteroides thetaiotaomicron
B. faecis
Desulfovibrio intestinalis
B. fragilis
Phocaeicola vulgatus
Clostridium leptum
−log10(FDR)
estimate
Up in MAdCAM-1norm
Up in MAdCAM-1lo
E
0.027
0.031
log10(fpkm)
ABX
E.bolteae
unc. Hungatella

Figure 3

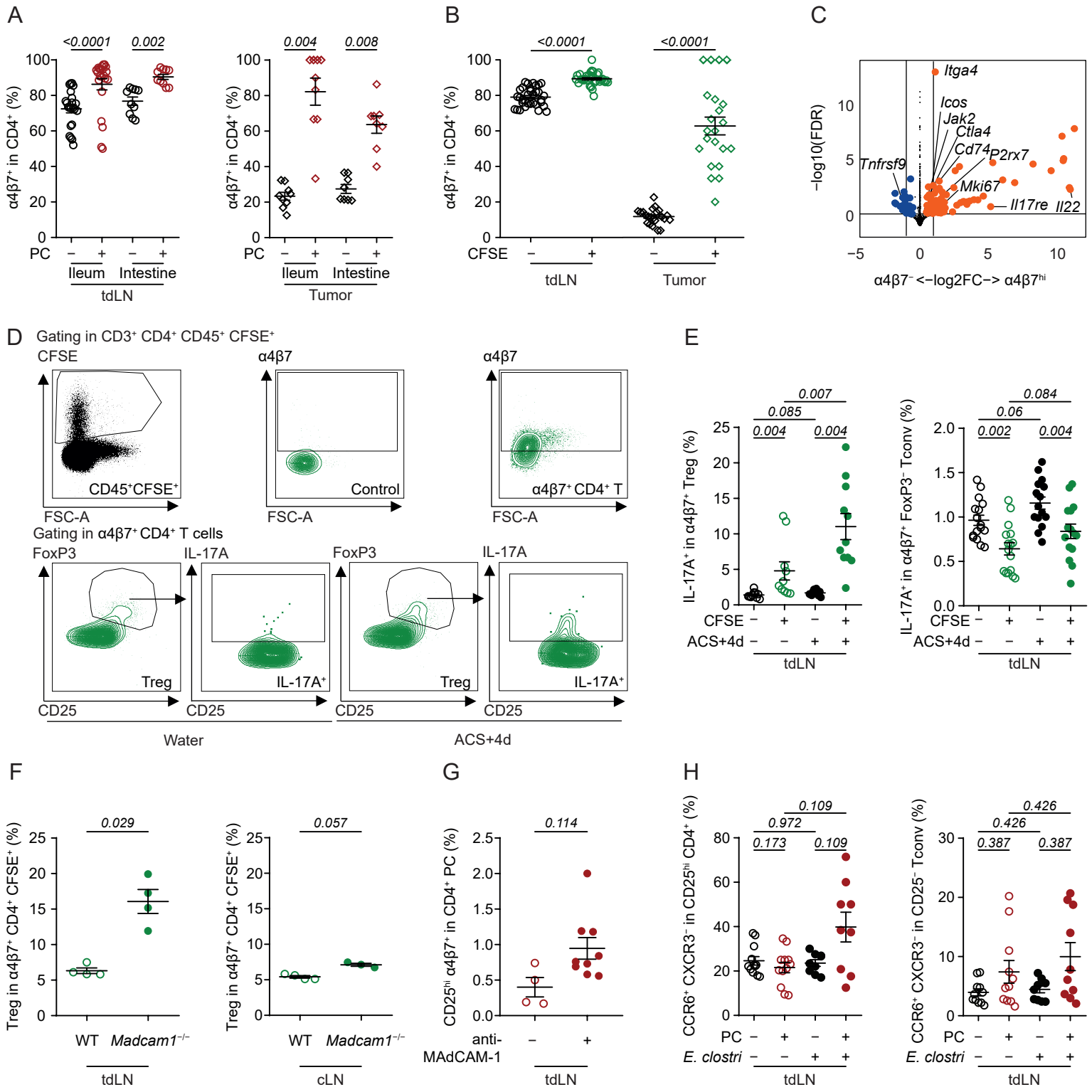
A
<0.0001
0.002
0.004
0.008
α4β7⁺ in CD4⁺ (%)
PC
Ileum
Intestine
tdLN
Tumor
B
<0.0001
<0.0001
CFSE
tdLN
Tumor
C
Itga4
Icos
Jak2
Ctla4
Cd74
P2rx7
Tnfrsf9
Mki67
Il17re
Il22
−log10(FDR)
α4β7⁻ <−log2FC−> α4β7ʰⁱ
D
Gating in CD3⁺ CD4⁺ CD45⁺ CFSE⁺
CFSE
α4β7
CD45⁺CFSE⁺
Control
α4β7⁺ CD4⁺ T
FSC-A
Gating in α4β7⁺ CD4⁺ T cells
FoxP3
IL-17A
Treg
IL-17A⁺
CD25
Water
ACS+4d
E
0.007
0.085
0.004
0.004
0.084
0.06
0.002
0.004
IL-17A⁺ in α4β7⁺ Treg (%)
IL-17A⁺ in α4β7⁺ FoxP3⁻ Tconv (%)
CFSE
ACS+4d
tdLN
F
0.029
0.057
Treg in α4β7⁺ CD4⁺ CFSE⁺ (%)
WT
Madcam1⁻/⁻
tdLN
cLN
G
0.114
CD25ʰⁱ α4β7⁺ in CD4⁺ PC (%)
anti-MAdCAM-1
tdLN
H
0.109
0.972
0.173
0.109
0.426
0.426
0.387
0.387
CCR6⁺ CXCR3⁻ in CD25ʰⁱ CD4⁺ (%)
CCR6⁺ CXCR3⁻ in CD25⁻ Tconv (%)
PC
E. clostri
tdLN

Figure 4

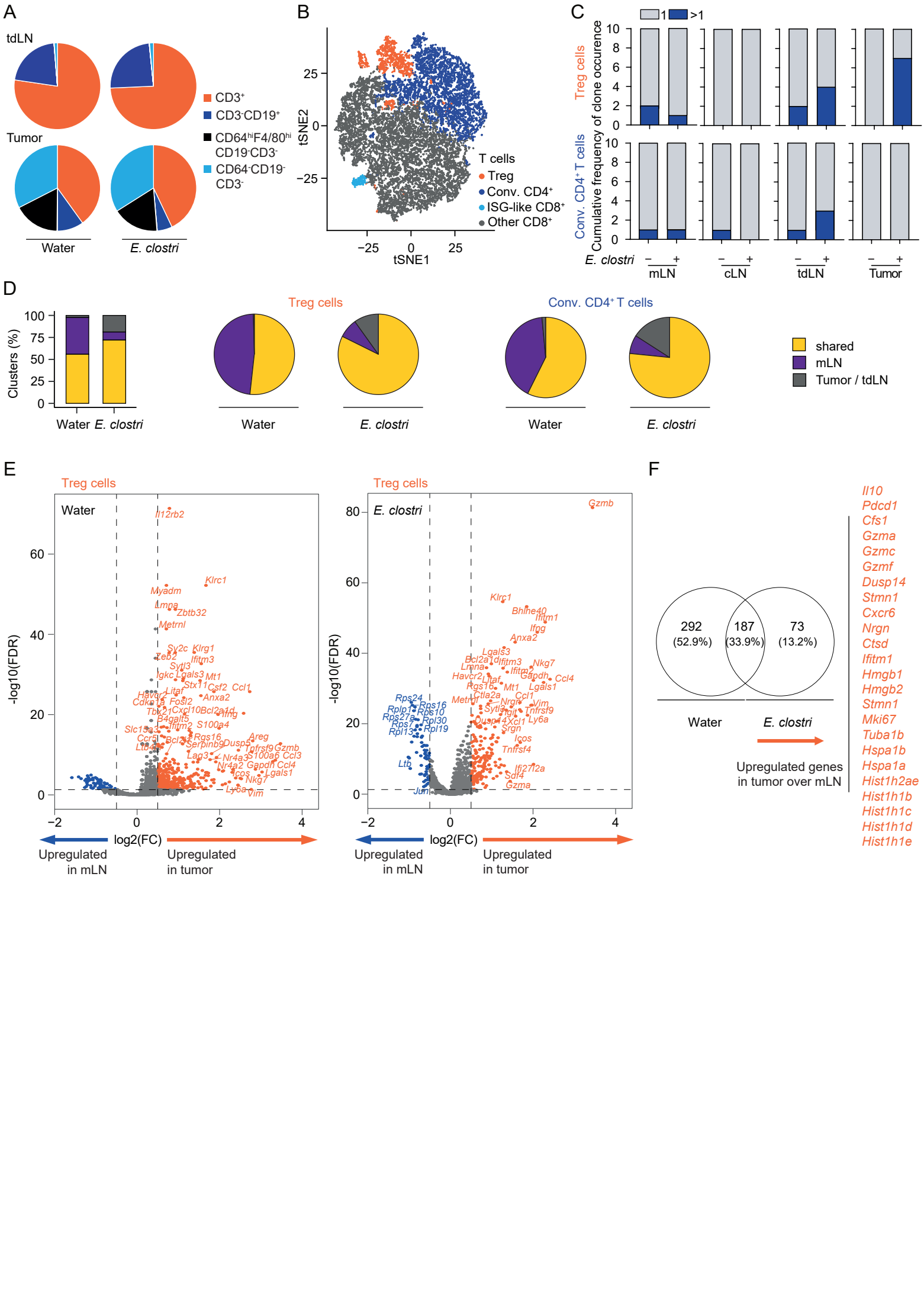
A
tdLN
Tumor
CD3+
CD3-CD19+
CD64hiF4/80hi CD19-CD3-
CD64-CD19- CD3-
Water
E. clostri
B
tSNE2
tSNE1
T cells
Treg
Conv. CD4+
ISG-like CD8+
Other CD8+
C
1
>1
Treg cells
Conv. CD4+ T cells
Cumulative frequency of clone occurence
E. clostri
mLN
cLN
tdLN
Tumor
D
Clusters (%)
Water E. clostri
Treg cells
Conv. CD4+ T cells
shared
mLN
Tumor / tdLN
E
Treg cells
Water
E. clostri
-log10(FDR)
log2(FC)
Upregulated in mLN
Upregulated in tumor
F
292 (52.9%)
187 (33.9%)
73 (13.2%)
Water
E. clostri
Upregulated genes in tumor over mLN
Il10
Pdcd1
Cfs1
Gzma
Gzmc
Gzmf
Dusp14
Stmn1
Cxcr6
Nrgn
Ctsd
Ifitm1
Hmgb1
Hmgb2
Stmn1
Mki67
Tuba1b
Hspa1b
Hspa1a
Hist1h2ae
Hist1h1b
Hist1h1c
Hist1h1d
Hist1h1e

Figure 5

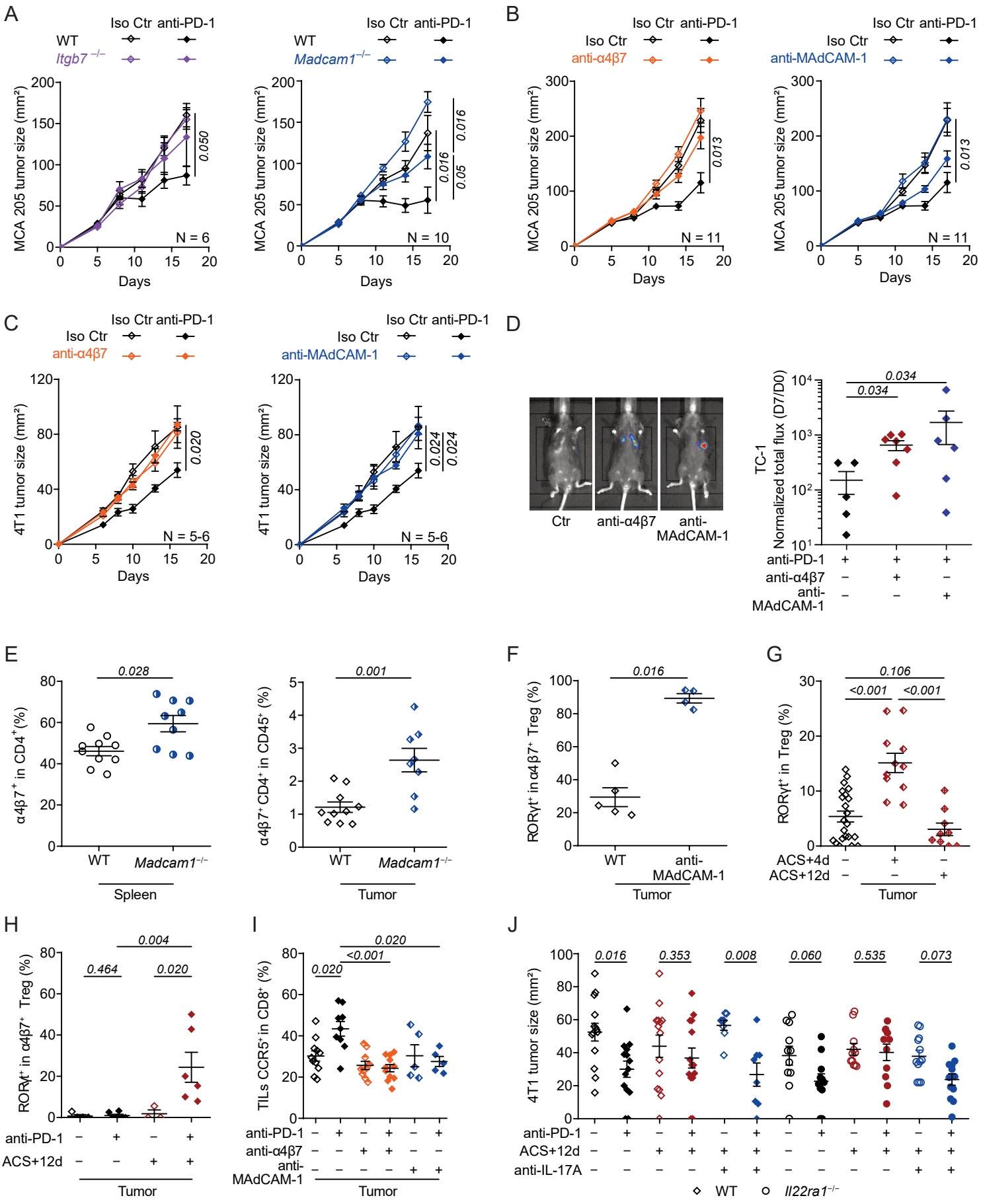
A
Iso Ctr anti-PD-1
WT
Itgb7 −/−
Madcam1−/−
MCA 205 tumor size (mm²)
Days
N = 6
N = 10
0.050
0.016
0.05
0.016
B
Iso Ctr
anti-α4β7
anti-MAdCAM-1
N = 11
0.013
C
4T1 tumor size (mm²)
N = 5-6
0.020
0.024
0.024
D
Ctr
anti-α4β7
anti-MAdCAM-1
TC-1
Normalized total flux (D7/D0)
0.034
0.034
E
α4β7+ in CD4+ (%)
0.028
WT
Madcam1−/−
Spleen
α4β7+ CD4+ in CD45+ (%)
0.001
Tumor
F
RORγt+ in α4β7+ Treg (%)
0.016
anti-MAdCAM-1
G
RORγt+ in Treg (%)
0.106
<0.001
<0.001
ACS+4d
ACS+12d
H
0.004
0.464
0.020
anti-PD-1
ACS+12d
I
TILs CCR5+ in CD8+ (%)
0.020
<0.001
0.020
anti-α4β7
anti-MAdCAM-1
J
0.016
0.353
0.008
0.060
0.535
0.073
anti-IL-17A
WT
Il22ra1−/−

Figure 6

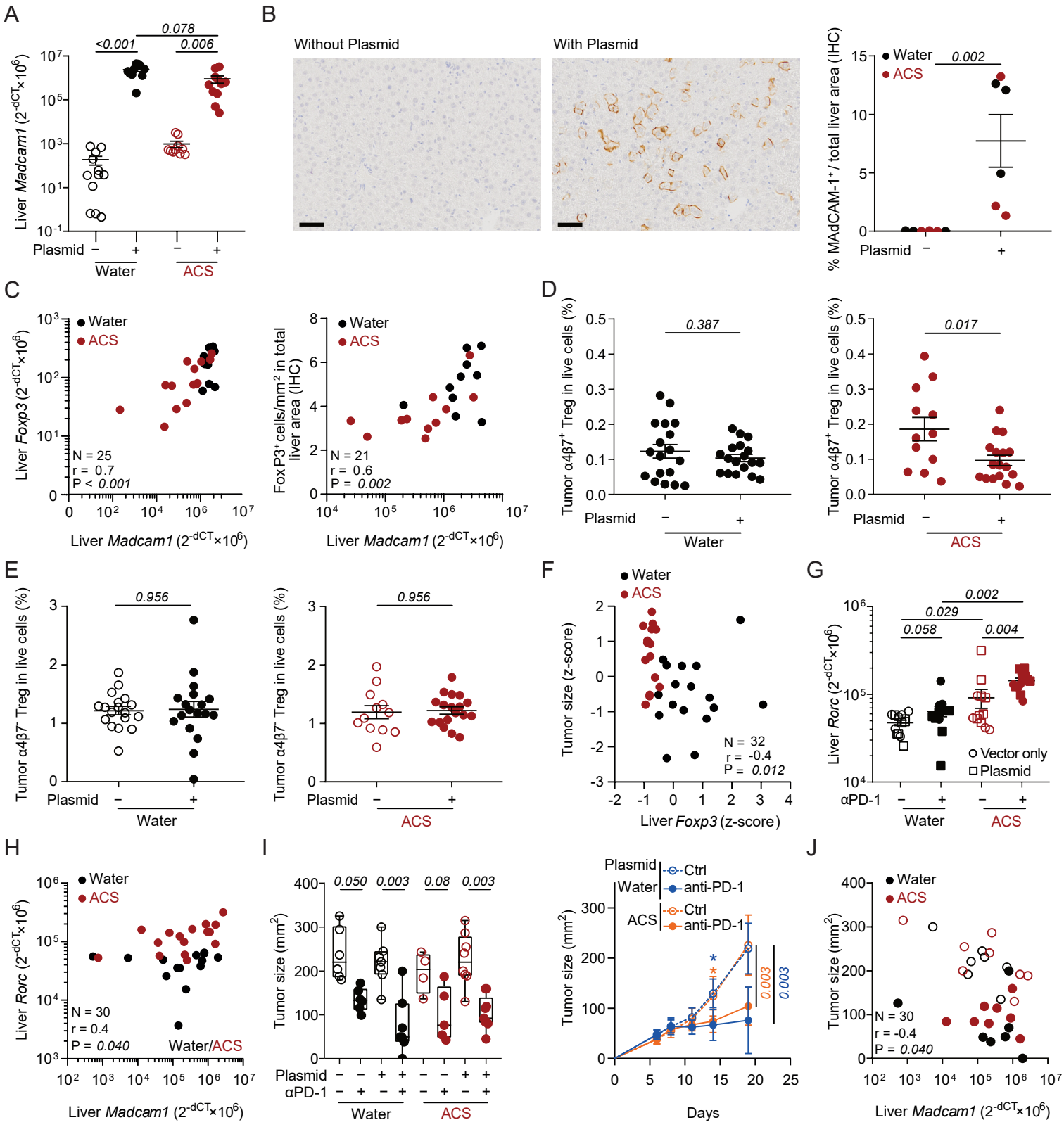
A
B
C
D
E
F
G
H
I
J
Without Plasmid
With Plasmid
Water
ACS
Plasmid
Liver Madcam1 (2-dCT×10^6)
% MAdCAM-1+ / total liver area (IHC)
Liver Foxp3 (2-dCT×10^6)
FoxP3+ cells/mm2 in total liver area (IHC)
Tumor α4β7+ Treg in live cells (%)
Tumor size (z-score)
Liver Foxp3 (z-score)
Liver Rorc (2-dCT×10^6)
Vector only
Plasmid
αPD-1
Tumor size (mm2)
Ctrl
anti-PD-1
Days
N = 25
r = 0.7
P < 0.001
N = 21
r = 0.6
P = 0.002
N = 32
r = -0.4
P = 0.012
N = 30
r = 0.4
P = 0.040
N = 30
r = -0.4
P = 0.040
Water/ACS

Figure 7

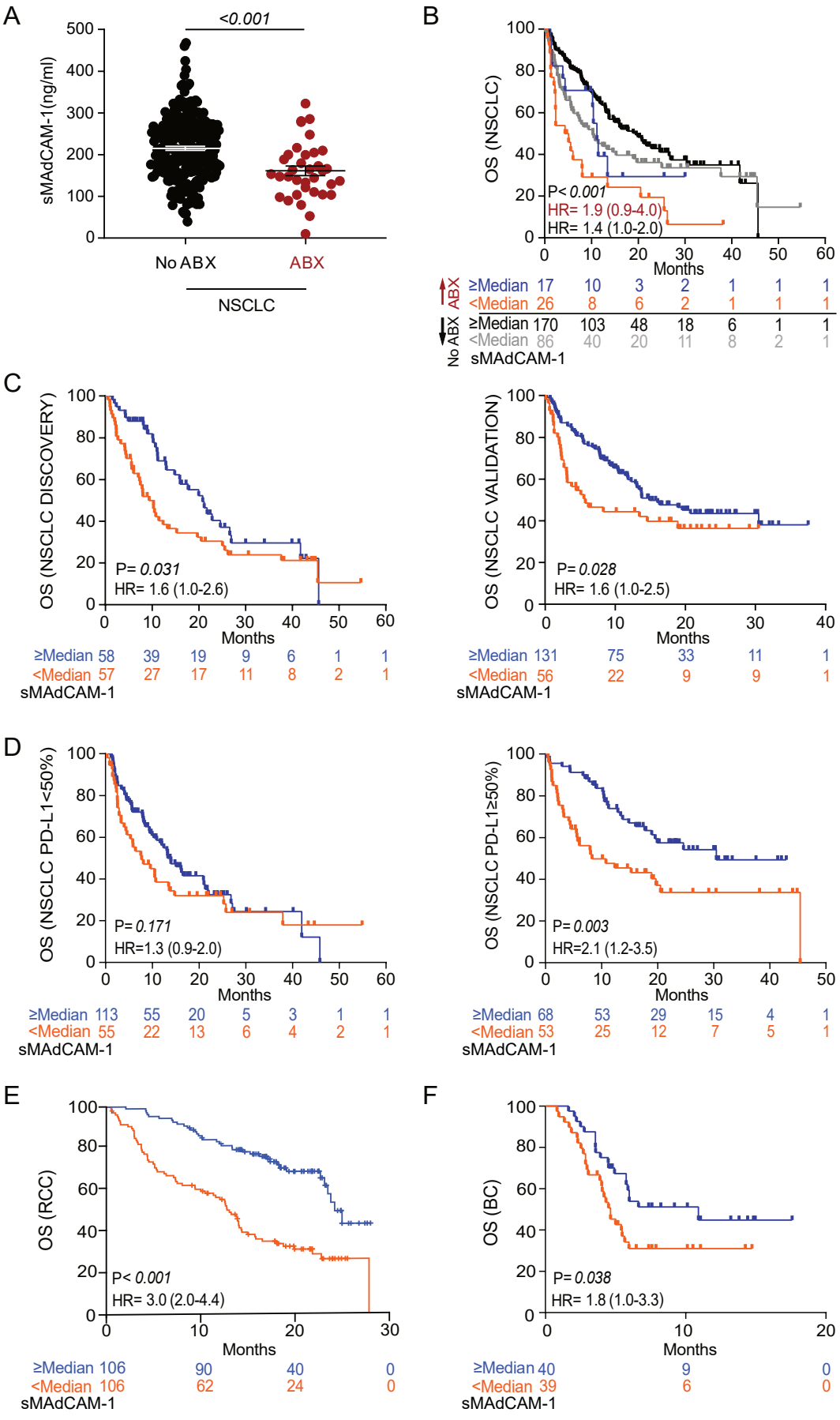
A
<0.001
sMAdCAM-1(ng/ml)
No ABX
ABX
NSCLC
B
OS (NSCLC)
P< 0.001
HR= 1.9 (0.9-4.0)
HR= 1.4 (1.0-2.0)
Months
ABX
≥Median 17 10 3 2 1 1 1
<Median 26 8 6 2 1 1 1
No ABX
≥Median 170 103 48 18 6 1 1
<Median 86 40 20 11 8 2 1
sMAdCAM-1
C
OS (NSCLC DISCOVERY)
P= 0.031
HR= 1.6 (1.0-2.6)
Months
≥Median 58 39 19 9 6 1 1
<Median 57 27 17 11 8 2 1
sMAdCAM-1
OS (NSCLC VALIDATION)
P= 0.028
HR= 1.6 (1.0-2.5)
Months
≥Median 131 75 33 11 1
<Median 56 22 9 9 1
sMAdCAM-1
D
OS (NSCLC PD-L1<50%)
P= 0.171
HR=1.3 (0.9-2.0)
Months
≥Median 113 55 20 5 3 1 1
<Median 55 22 13 6 4 2 1
sMAdCAM-1
OS (NSCLC PD-L1≥50%)
P= 0.003
HR=2.1 (1.2-3.5)
Months
≥Median 68 53 29 15 4 1
<Median 53 25 12 7 5 1
sMAdCAM-1
E
OS (RCC)
P< 0.001
HR= 3.0 (2.0-4.4)
Months
≥Median 106 90 40 0
<Median 106 62 24 0
sMAdCAM-1
F
OS (BC)
P= 0.038
HR= 1.8 (1.0-3.3)
Months
≥Median 40 9 0
<Median 39 6 0
sMAdCAM-1

Figure 8

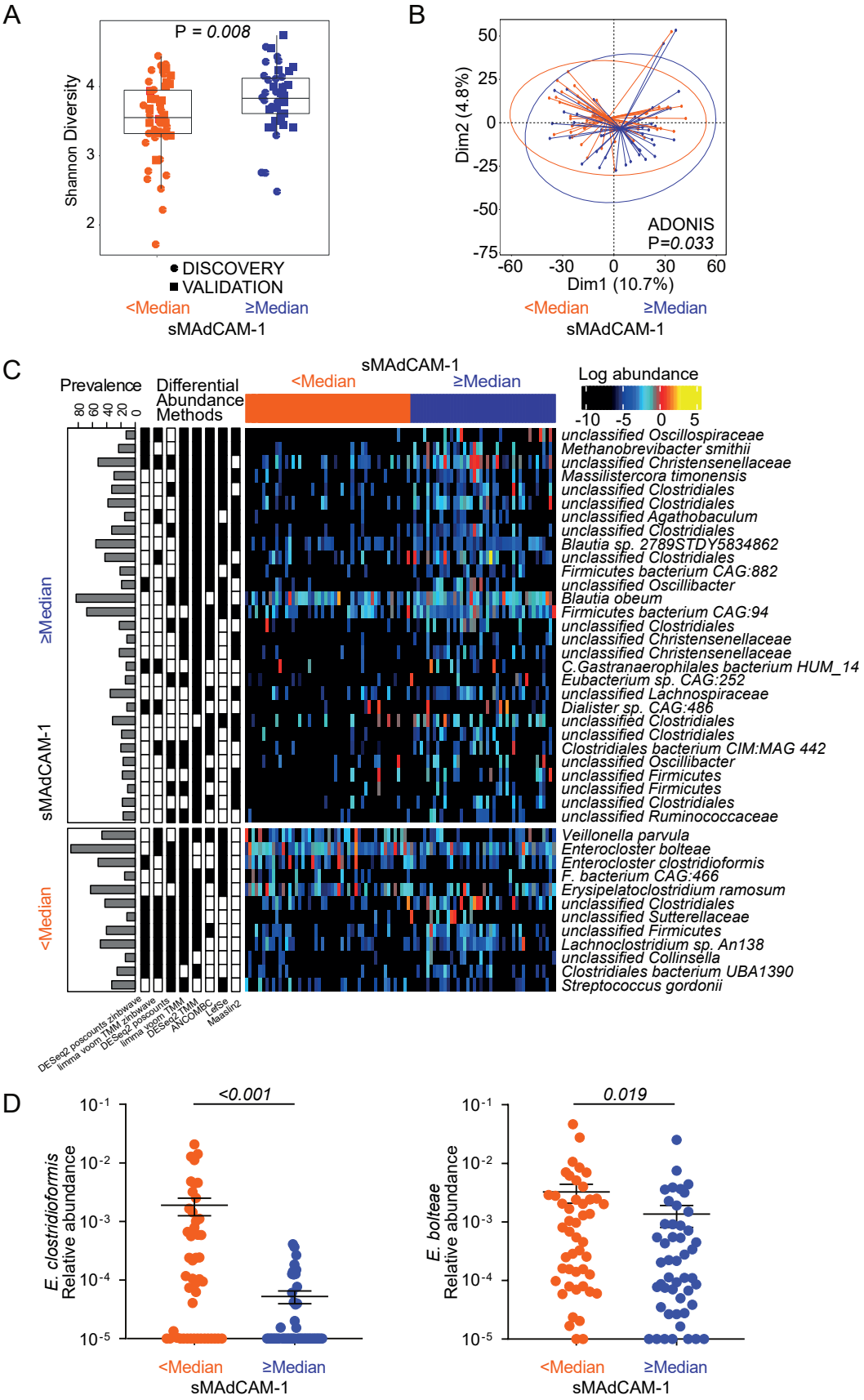
A
P = 0.008
Shannon Diversity
DISCOVERY
VALIDATION
<Median
≥Median
sMAdCAM-1
B
Dim2 (4.8%)
Dim1 (10.7%)
ADONIS
P=0.033
<Median
≥Median
sMAdCAM-1
C
sMAdCAM-1
<Median
≥Median
Prevalence
Differential Abundance Methods
Log abundance
unclassified Oscillospiraceae
Methanobrevibacter smithii
unclassified Christensenellaceae
Massilistercora timonensis
unclassified Clostridiales
unclassified Clostridiales
unclassified Agathobaculum
unclassified Clostridiales
Blautia sp. 2789STDY5834862
unclassified Clostridiales
Firmicutes bacterium CAG:882
unclassified Oscillibacter
Blautia obeum
Firmicutes bacterium CAG:94
unclassified Clostridiales
unclassified Christensenellaceae
unclassified Christensenellaceae
C.Gastranaerophilales bacterium HUM_14
Eubacterium sp. CAG:252
unclassified Lachnospiraceae
Dialister sp. CAG:486
unclassified Clostridiales
unclassified Clostridiales
Clostridiales bacterium CIM:MAG 442
unclassified Oscillibacter
unclassified Firmicutes
unclassified Firmicutes
unclassified Clostridiales
unclassified Ruminococcaceae
Veillonella parvula
Enterocloster bolteae
Enterocloster clostridioformis
F. bacterium CAG:466
Erysipelatoclostridium ramosum
unclassified Clostridiales
unclassified Sutterellaceae
unclassified Firmicutes
Lachnoclostridium sp. An138
unclassified Collinsella
Clostridiales bacterium UBA1390
Streptococcus gordonii
DESeq2 poscounts zinbwave
limma voom TMM zinbwave
DESeq2 poscounts
limma voom TMM
DESeq2 TMM
ANCOMBC
LeSe
Maaslin2
D
<0.001
0.019
E. clostridioformis Relative abundance
E. bolteae Relative abundance
<Median
≥Median
sMAdCAM-1

Science
AAAS

Supplementary Materials for

A microbiota -modulated checkpoint directs immunosuppressive intestinal T cells into cancer

Marine Fidelle[1,2,3]†, Conrad Rauber[1,2,3,4]*†, Carolina Alves Costa Silva[1,2,3]†, Ai-Ling Tian[1,2,5,6], Imran Lahmar[1,2,3], Anne-Laure Mallard de La Varende[1,2,3], Liwei Zhao[1,5,6], Cassandra Thélémaque[1,3], Isabelle Lebhar[1,3], Meriem Messaoudene[7], Eugenie Pizzato[1,3], Roxanne Birebent[1,2,3], Maxime Descartes Mbogning Fonkou[1,3], Silvia Zoppi[1,2,8], Anna Reni[1,2,9], Cécile Dalban[10], Marion Leduc[1,5,6], Gladys Ferrere[1,3,11], Sylvère Durand[1,5,6], Pierre Ly[1,3,12], Aymeric Silvin[1,3], Kevin Mulder[1,2,3], Charles-Antoine Dutertre[1,3], Florent Ginhoux[1,3], Satoru Yonekura[1,2,3], Maria Paula Roberti[1,3,13,14], Maryam Tidjani-Alou[1,3], Safae Terrisse[1,2,3], Jianzhou Chen[1,3], Oliver Kepp[1,5,6], Angela Schippers[15], Norbert Wagner[15], Javier Suárez Gosálvez[16], Sebastian Kobold[16,17], Jean-Eudes Fahrner[1,2,3], Corentin Richard[7], Jacques Bosq[18], Leonardo Lordello[1,3], Giacomo Vitali[19], Nathalie Galleron[19], Benoît Quinquis[19], Emmanuelle Le Chatelier[19], Lucas Blanchard[20], Jean-Philippe Girard[20], Anne Jarry[21], Nadine Gervois[21], Emmanuelle Godefroy[21], Nathalie Labarrière[21,22], Ronald Koschny[4], Romain Daillère[11], Benjamin Besse[1,2], Caroline Truntzer[23], François Ghiringhelli[23], Nicolas Coatnoan[24,25], Vanessa Mhanna[24,25], David Klatzmann[24,25], Damien Drubay[1,26,27], Laurence Albiges[1,2], Andrew Maltez Thomas[28], Nicola Segata[28,29], François-Xavier Danlos[1,2,3,12,30], Aurélien Marabelle[1,2,3,12,30], Bertrand Routy[7,31], Lisa Derosa[1,2,3,12]†, Guido Kroemer[5,6,32]*†, Laurence Zitvogel[1,2,3,12]*†

Corresponding authors: Laurence Zitvogel, laurence.zitvogel@gustaveroussy.fr; Guido Kroemer, kroemer@orange.fr; Conrad Rauber, conrad.rauber@gmx.de

This PDF file includes:

Supplementary Materials

Figs. S1 to S10

Tables S1 to S9

Data S1 and Data S2

Figure S1

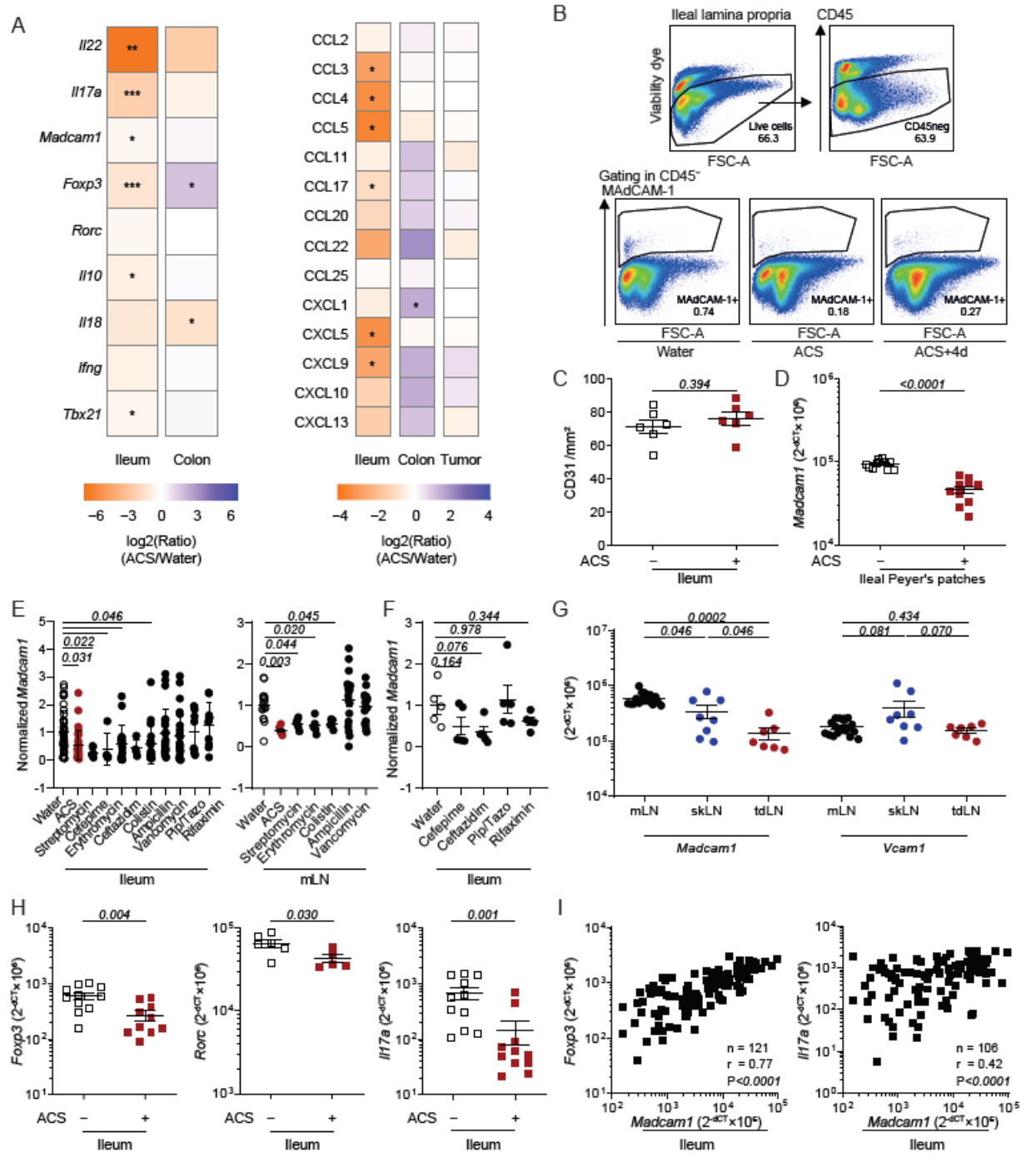

Fig. S1. ACS-induced dysbiosis affects the transcriptional program of immune genes in the intestinal lamina propria. (**A**) Heatmap of log2-fold change ratios between ACS-treated and not treated (water) ileum, colon, as well as tumor beds for cytokines/transcription factors (left panel) and chemokines (right panel) expression profiles in RT-qPCR and ELISA of the tissue lysates. (**B**)

Representative flow cytometric analysis of MAdCAM-1 protein expression in live CD45 negative cells from the LP in water or ACS conditions (ACS: under antibiotics, ACS+4d: after 4 days of ACS discontinuation). (**C**) Evaluation of CD31 expression on ileal HEV by IHC in ACS-treated mice (see also **Fig. 1B**). (**D**) RT-qPCR assessment of the relative expression of *Madcam1* in ileal Peyer's patches (PP) (N=2). (**E**) RT-qPCR evaluation of the impact of 7 days conditioning with various antibiotic regimens or after ACS+4d on relative transcription levels of *Madcam1* gene in ileal tissue (**left**) or in mesenteric lymph nodes (mLN) (**right**). (**F**) Same as in (E) but in another animal facility (from CHUM). (**G**) RT-qPCR assessment of the relative expression of *Madcam1* and *Vcam1* genes in various lymph nodes (LN) (mLN: mesenteric LN, sk: skin LN, td: tumor-draining LN). (**H and I**) RT-qPCR evaluation of murine *Foxp3*, *Rorc* and *Il17a* genes in ileal tissue of mice treated or not with ACS. (H), and Spearman correlations between ileal *Madcam1* and *Foxp3* or *Il17a* expression levels in mice (I). Panel E, H and I depicts a pool of 2-3 independent experiments. Results from a representative experiment are shown in panel A, B, C, F and G. For E, the graph pooled the data from 8 and 3 independent experiments investigating the ileum or mLNs respectively, each comprising 5-6 mice per group. Each dot represents one animal. Comparisons between groups were analyzed using nonparametric Mann–Whitney *U* test (two groups) or Kruskal–Wallis *H* test (>2 groups) followed by multiple-comparisons test by controlling the FDR. For (I), nonparametric Spearman correlations were performed. Error bars represent means ± SEM.

Figure S2

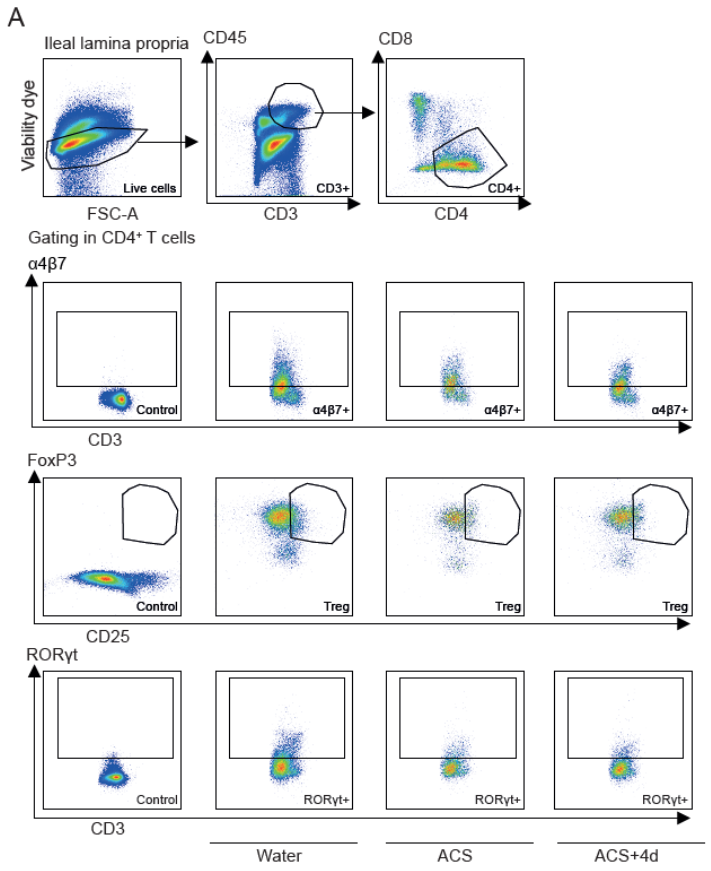

Fig. S2. Representative flow cytometric analysis of Treg and RORγt$^+$ cells in the ileal lamina propria. Representative flow cytometric analysis of T cells of the ileal LP gating on live CD45$^+$ cells, then T cells (CD3, CD4, or CD8). In the CD4$^+$ T cell gate, we analyzed staining with anti-α4β7 Abs, or anti-FoxP3 and CD25, or RORγt in water or ACS conditions (ACS: under antibiotics, ACS+4d: after 4 days of ACS discontinuation). A typical dot plot is shown for each gating.

Figure S3

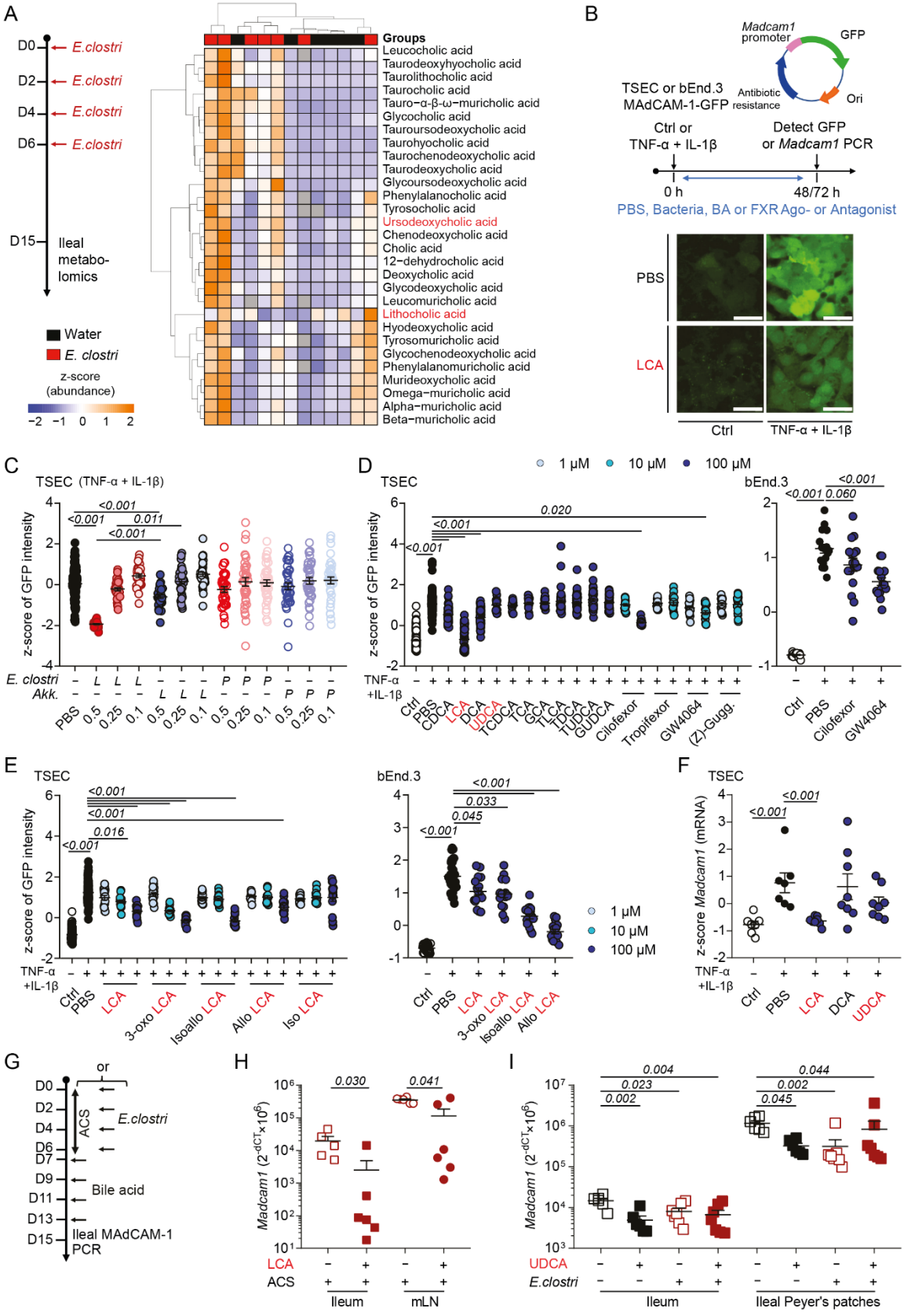
A
D0 E.clostri
D2 E.clostri
D4 E.clostri
D6 E.clostri
D15 Ileal metabo-lomics
Water
E. clostri
z-score (abundance)
−2 −1 0 1 2
Groups
Leucocholic acid
Taurodeoxyhyocholic acid
Taurolithocholic acid
Taurocholic acid
Tauro−α−β−ω−muricholic acid
Glycocholic acid
Tauroursodeoxycholic acid
Taurohyocholic acid
Taurochenodeoxycholic acid
Taurodeoxycholic acid
Glycoursodeoxycholic acid
Phenylalanocholic acid
Tyrosocholic acid
Ursodeoxycholic acid
Chenodeoxycholic acid
Cholic acid
12−dehydrocholic acid
Deoxycholic acid
Glycodeoxycholic acid
Leucomuricholic acid
Lithocholic acid
Hyodeoxycholic acid
Tyrosomuricholic acid
Glycochenodeoxycholic acid
Phenylalanomuricholic acid
Murideoxycholic acid
Omega−muricholic acid
Alpha−muricholic acid
Beta−muricholic acid
B
Madcam1 promoter
GFP
Antibiotic resistance
Ori
TSEC or bEnd.3 MAdCAM-1-GFP
Ctrl or TNF-α + IL-1β
Detect GFP or Madcam1 PCR
0 h
48/72 h
PBS, Bacteria, BA or FXR Ago- or Antagonist
PBS
LCA
Ctrl
TNF-α + IL-1β
C
TSEC (TNF-α + IL-1β)
z-score of GFP intensity
E. clostri
Akk.
PBS 0.5 0.25 0.1 0.5 0.25 0.1 0.5 0.25 0.1 0.5 0.25 0.1
D
1 μM 10 μM 100 μM
TSEC
bEnd.3
TNF-α +IL-1β
Ctrl PBS CDCA LCA DCA UDCA TCDCA TCA GCA TLCA TUDCA GUDCA Cilofexor Tropifexor GW4064 (Z)-Gugg.
Ctrl PBS Cilofexor GW4064
E
TSEC
bEnd.3
Ctrl PBS LCA 3-oxo LCA Isoallo LCA Allo LCA Iso LCA
F
TSEC
z-score Madcam1 (mRNA)
Ctrl PBS LCA DCA UDCA
G
or
D0 D2 D4 D6 D7 D9 D11 D13 D15
ACS
E.clostri
Bile acid
Ileal MAdCAM-1 PCR
H
Madcam1 (2−dCT×10^6)
LCA
ACS
Ileum
mLN
I
Madcam1 (2−dCT×10^6)
UDCA
E.clostri
Ileum
Ileal Peyer's patches

Fig. S3. *E. clostridioformis*-induced perturbation of ileal biliary acids (BA) and downregulation of MAdCAM-1. (**A**) Effects of *E. clostridioformis* on ileal metabolites after iterative oral gavage with the bacterium. Targeted metabolomics-profiling of ileal metabolites unveiled a selective and marked alteration of BA composition at one week (D15) in the *E.clostridioformis* group (*E. clostri*) of mice compared with controls. Following gavage with *E. clostri*, and normalization to medium values for each metabolite, we used a non-supervised hierarchical clustering (Euclidean distance, ward linkage method) of *z*-score-normalized abundances of multiple bile acids (BA) (one representative experiment of n=6-7 mice per group). (**B to E**) High content confocal microscopy screening using TSEC and bEnd.3 cells stably expressing GFP under the control of the MAdCAM-1 promoter (Scale bar: 40 µm) (**B**) and exposed to live (*L*) and pasteurized (*P*) bacteria at various concentrations (0.5, 0.25, and 0.1 dilutions of 1OD) (**C**) or multiple BA (**D**) and isoforms as well as farnesoid X receptor (FXR) agonists and antagonists (**E**) at various concentrations (1, 10, and 100 µM). Results are depicted as *z*-score-normalized fluorescence intensity of GFP of triplicate wells, pooling three independent experiments. (**F**) Quantitative PCR analysis of *Madcam1* gene transcripts in TSEC exposed to inflammatory cytokines plus BA (100 µM) in vitro. Results from 2 independent experiments are pooled. (**G to I**) In vivo effects of BA on *Madcam-1* expression in vivo. (G) Experimental setting of BA (LCA, UDCA) orally gavaged with (H) or without (I) ACS, and with (I) or without (H) *E. clostri* in naïve animals. The results of ileal *Madcam1* expression assessed by RT-qPCR of ileal LP, mLN or PP of a representative experiment are depicted, each dot representing one mouse. Two experiments were independently performed yielding similar results. Comparisons between groups were analyzed using nonparametric Mann–Whitney *U* test (2 groups) or Kruskal–Wallis *H* test (>2 groups) followed by multiple-comparisons test by controlling the FDR. Error bars represent mean ± SEM.

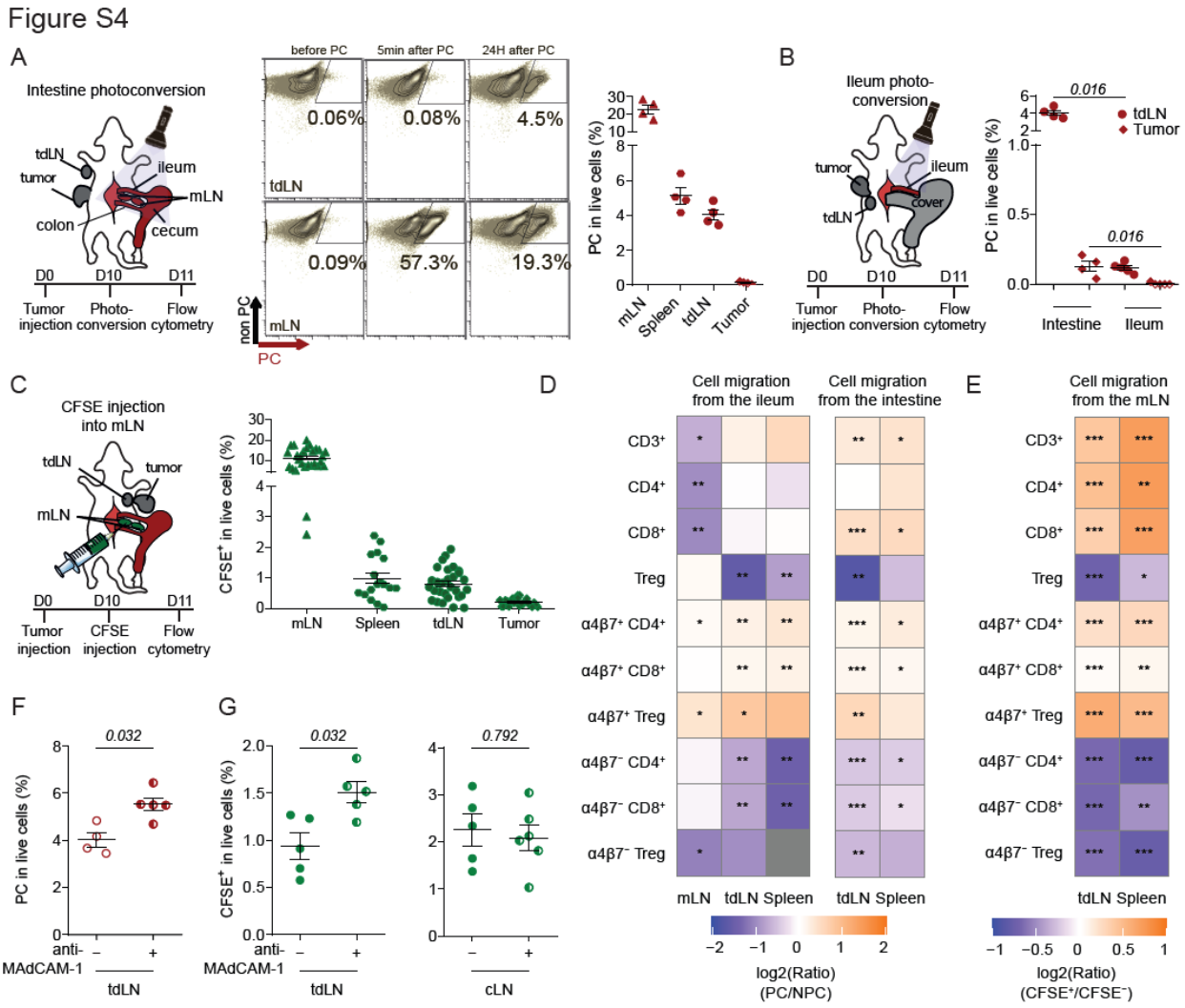

Figure S4. Migratory capacity of enterotropic α4β7 Treg to tdLN and tumors.

(**A**) Schematic overview of the experimental setup of UV-A illumination of the intestine (ileum, caecum, mesenteric lymph nodes (mLNs)) in tumor-bearing Kaede mice (left panel). Flow cytometric gating strategy of photoconverted cells (PC) in tdLN and mLN (right panel) with PC frequencies in target organs before, 5 min after, and 24 hours after laparotomy and UV-A illumination of the intestine compartment (middle panel) as well as detailed percentages of PC cells in mLNs, spleens, tdLNs, and tumor beds at 24 hours, each dot representing one mouse (right panel). A typical experiment out of three yielding similar results is depicted. (**B**) Flow cytometric determination of photoconverted (PC) gut-originating cells in secondary lymphoid organs (mesenteric LN, spleen, tdLNs) and tumors assessed in Kaede mice after UV-A illumination of ileum or "intestine" (ileum+caecum+mLNs). The left panel depicts the graphical schema of the

experimental setting and the right panel shows the percentages of photoconverted (PC) cells in tdLNs and tumor, each dot representing one mouse. A representative experiment out of three is depicted in A and B, comprising 5-6 mice per group. (**C**) Id. as in (A) in CFSE labeled mLNs with detailed percentages of $CFSE^+$ cells in mLNs, spleen, tdLNs and tumor beds at 24 hours, each dot representing one mouse (right panel). The left panel depicts the graphical schema of the experimental setting. The results of four independent experiments were pooled in C, right panel. (**D**) Flow cytometric determination of relative accumulation (log2 Ratio of photoconverted (PC) versus resident (non-photoconverted (NPC)) cells in each cellular subset in various secondary lymphoid organs (SLO) using a color gradient, 24 hours after "intestine" (ileum+caecum+mLN) (right panel) or ileum (left panel) UV-A illumination. (**E**) Same as in (D) for the CFSE-labeled mLNs-origin cell model. The results of three (ileum) and two (intestine) (D) and four (E) independent experiments were pooled. (**F and G**). Effect of the neutralization of MAdCAM-1 using anti-MAdCAM-1 mAb on the recirculation of gut-derived cells towards the tdLN in Kaede (red dots (F)) or in mLNs-CFSE-injected WT mice (green dots (G, left panel)) or towards a contralateral LN (cLN) (green dots (G, right panel)). A representative experiment comprising 4-6 mice per group is depicted in F-G. Comparisons between groups were analyzed using nonparametric Mann–Whitney *U* test (2 groups) followed by multiple-comparisons test by controlling the FDR. Error bars represent mean ± SEM. For D and E, $*P<0.05$, $**P<0.01$, and $***P<0.001$.

Figure S5

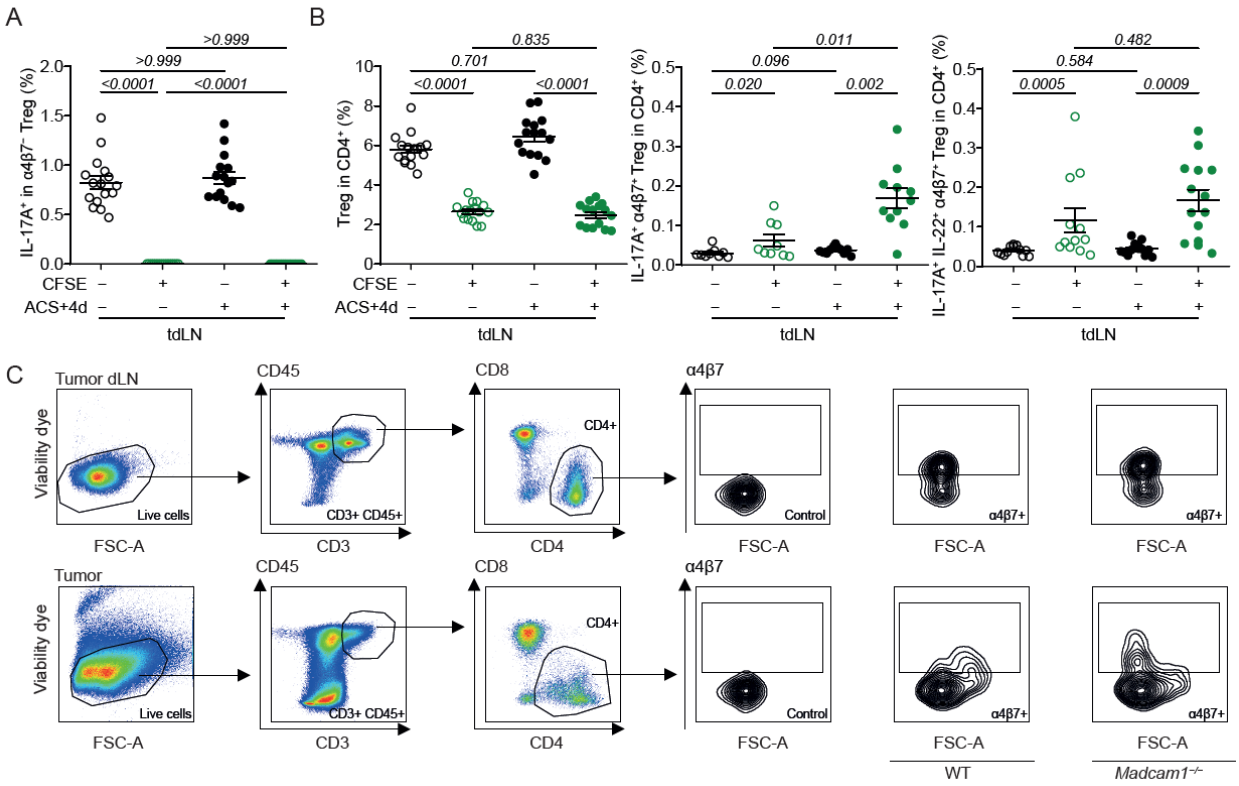

Fig. S5. Tracking enterotropic Tr17 cells during their exodus from mLN to tumor lesions. (**A and B**). Representative flow cytometric evaluation of different $CD4^+$ Treg cell types (varying in the expression of α4β7, IL-17A, IL-22) in tdLNs traced by CFSE labeling in animals treated or not with ASC+4d (i.e., 4 days of spontaneous recolonization post ACS-cessation) and bearing subcutaneous MCA205 and subjected to CFSE injection in the mLN 24 hours before (n=9-16 mice per group). (**C**) Representative gating strategy to analyze $\alpha4\beta7^+$ $CD4^+$ T cells in the tdLN and tumor beds. Live $CD45^+$ $CD4^+$ T cells were then analyzed for the expression of the heterodimer α4β7 in tdLN and MCA205 sarcomas in wildtype of *Madcam1* deficient mice (see also Fig. 3F). Comparisons between groups were analyzed using nonparametric Kruskal–Wallis *H* test (>2 groups) followed by multiple-comparisons test by controlling the FDR. For PC^+ vs PC^- or $CFSE^+$ vs $CFSE^-$ comparisons, Wilcoxon matched-pairs signed rank test were performed. Error bars represent mean ± SEM.

Figure S6

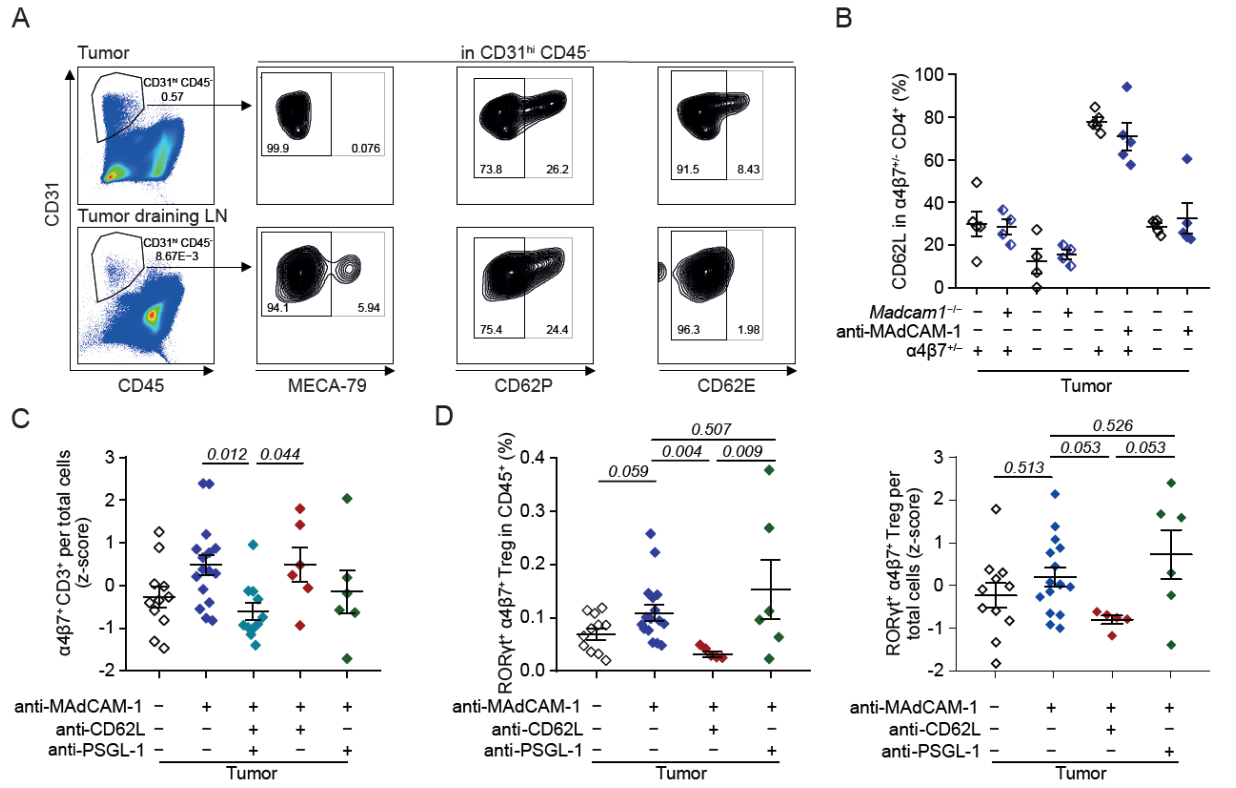

Fig. S6. Role of E/P/L selectins in the accumulation of T cells into tumor-draining LNs and sarcomas during MAdCAM-1 blockade.

(**A and B**) Representative flow cytometric analysis of PNAd (MECA-79), P and E-selectins in CD31^{hi} CD45^{-} cells from MCA205 (upper) or tdLN (lower panel) ((**A**), representative dot plot), as well as CD62L expression in CD4^{+} TILs according to their α4β7 expression and the functionality of MAdCAM-1 (using *Madcam1*$^{+/+}$ or *Madcam1*$^{-/-}$ mice or anti-MAdCAM-1 neutralizing antibodies) (**B**). (**C to E**) Flow cytometric analysis of the effects of blocking CD62L or PSGL-1 during antibody-mediated neutralization of MAdCAM-1 in MCA205 tumor-bearing mice on the accumulation of various cell types (indicated in the Y axis) in tumor beds (**D and E**). Each dot represents one mouse. Results depict absolute numbers *z*-score normalized (**C and D,** right panel) or percentages (**B and D**, left panel). Graphs B, C and D represent results from two independent and pooled experiments of 5-6 mice per group. Comparisons between groups were analyzed using nonparametric Kruskal–Wallis *H* test (>2 groups) followed by multiple-comparisons test by controlling the FDR. Error bars represent mean ± SEM.

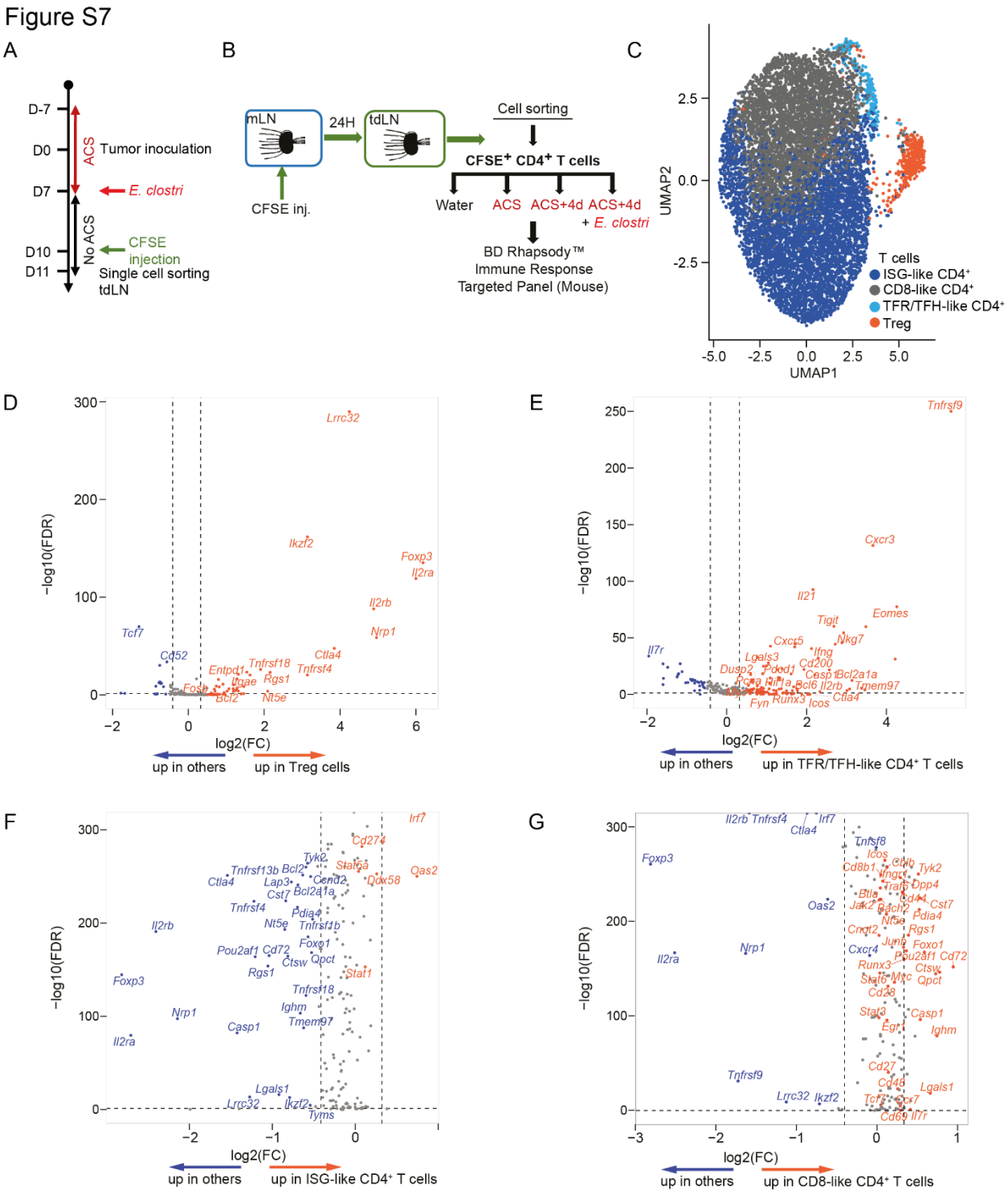

Fig. S7. Characterization of enterotropic CD4⁺ T cells reaching the tdLN after antibiotics. (**A-B**) Experimental setting for the single-cell sorting and RNA sequencing using Rhapsody technology to characterize phenotypic traits of CFSE⁺ CD4⁺ T cell subsets emigrating from mLN and reaching tdLN after discontinuation of ACS ± *E. clostridioformis* (*E. clostri*). (**C**) Uniform

manifold approximation and projection (UMAP) visualization of four clusters of emigrating $CFSE^+$ $CD4^+$ T cells in plate-based full-length single-cell RNA-seq data by unsupervised clustering, overlaying the four groups of mice. (**D to G**) Volcano plots of differential gene expression patterns associated with each specific cell type versus the others clustered in (C) according to log10(FDR) and log2-fold change (FC) ratio. Genes are colored if they passed the thresholds for FDR and log2(FC), significant differences being annotated in orange (upregulated) and blue (downregulated). A representative experiment out of two is depicted.

Figure S8

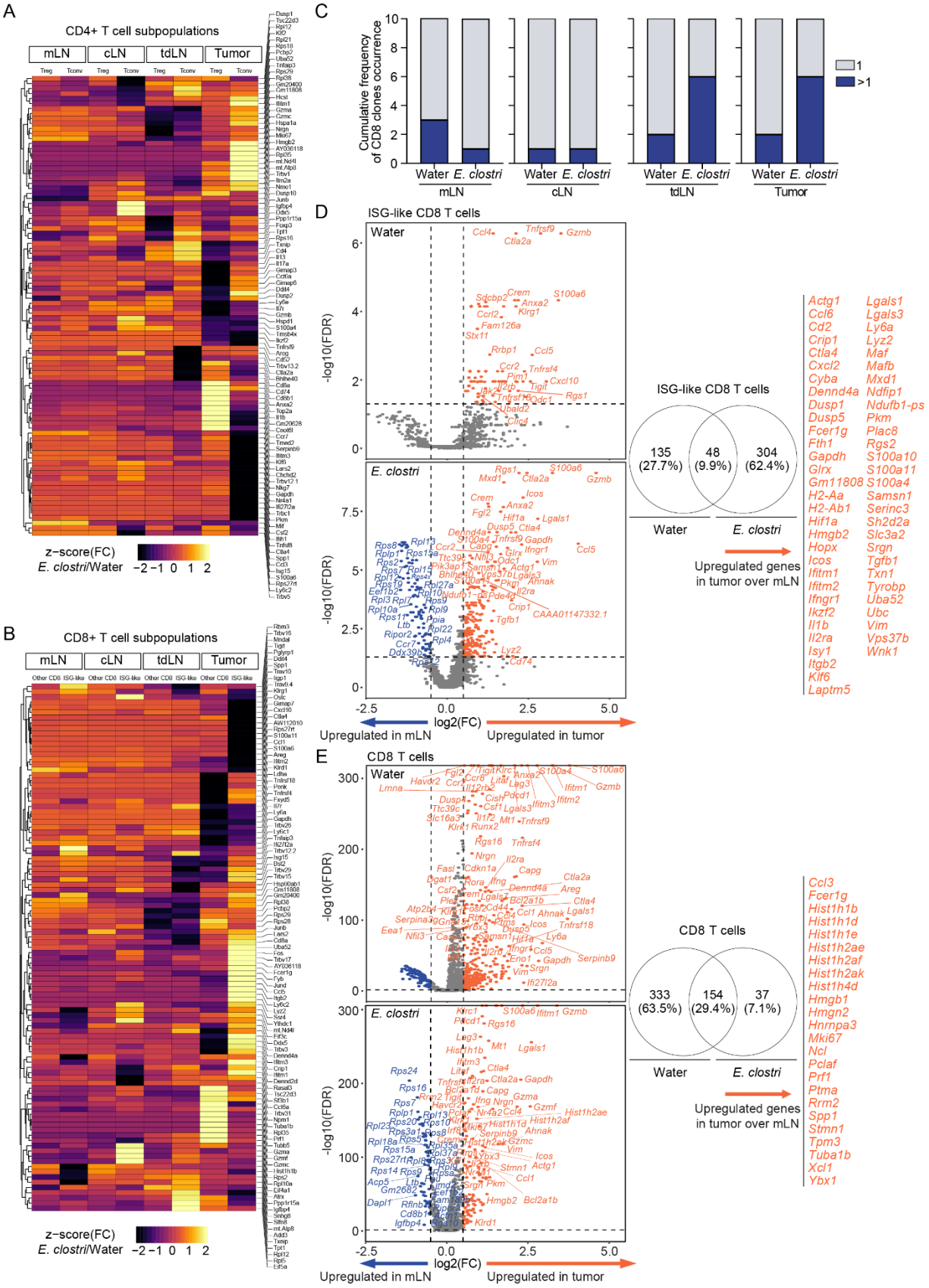
A
CD4+ T cell subpopulations
mLN
cLN
tdLN
Tumor
Treg
Tconv
z−score(FC)
E. clostri/Water −2 −1 0 1 2
B
CD8+ T cell subpopulations
Other CD8
ISG-like
C
Cumulative frequency of CD8 clones occurrence
Water
E. clostri
1
>1
D
ISG-like CD8 T cells
-log10(FDR)
log2(FC)
Upregulated in mLN
Upregulated in tumor
135 (27.7%)
48 (9.9%)
304 (62.4%)
Upregulated genes in tumor over mLN
Actg1 Ccl6 Cd2 Crip1 Ctla4 Cxcl2 Cyba Dennd4a Dusp1 Dusp5 Fcer1g Fth1 Gapdh Glrx Gm11808 H2-Aa H2-Ab1 Hif1a Hmgb2 Hopx Icos Ifitm1 Ifitm2 Ifngr1 Ikzf2 Il1b Il2ra Isy1 Itgb2 Klf6 Laptm5
Lgals1 Lgals3 Ly6a Lyz2 Maf Mafb Mxd1 Ndfip1 Ndufb1-ps Pkm Plac8 Rgs2 S100a10 S100a11 S100a4 Samsn1 Serinc3 Sh2d2a Slc3a2 Srgn Tgfb1 Txn1 Tyrobp Uba52 Ubc Vim Vps37b Wnk1
E
CD8 T cells
333 (63.5%)
154 (29.4%)
37 (7.1%)
Upregulated genes in tumor over mLN
Ccl3 Fcer1g Hist1h1b Hist1h1d Hist1h1e Hist1h2ae Hist1h2af Hist1h2ak Hist1h4d Hmgb1 Hmgn2 Hnrnpa3 Mki67 Ncl Pclaf Prf1 Ptma Rrm2 Spp1 Stmn1 Tpm3 Tuba1b Xcl1 Ybx1

Fig. S8. Gene patterns and clonal expansion of enterotropic CD4$^+$ and CD8$^+$ T cells associated with target locations and gavaging with *E. clostridioformis*. (**A**) Heatmap representing the top 10 upregulated or downregulated genes between water and *E.clostridioformis (E. clostri)*-treated mice for each CD4$^+$ T cell subpopulations (regulatory FoxP3$^+$ CD127$^-$ CD4$^+$ T cells (Treg) or conventional FoxP3$^-$ CD4$^+$ T cells (Tconv) in each organ (mLNs, cLNs, tdLNs and tumor). Genes are arranged in rows and ordered according to unsupervised hierarchical clustering. CD4$^+$ T cell subpopulations are arranged in columns and ordered according to localization and subtypes. Color bars represent the *z*-scores of the fold changes (FC) (*E.clostridioformis* over water) of average expression for each genes. (**B**) Idem as in A. for CD8$^+$ T cell subsets. (**C**) Single-cell TCR sequencing was performed on CFSE-stained CD8$^+$ T lymphocytes sampled from the mLN, the cLN, the tumor and tdLN. Cumulative frequencies of CD8$^+$ cell clonal occurrence according to location are depicted. (**D and E**) Venn diagrams comparing tumor-associated genes in water and *E.clostridioformis*-treated groups for ISG-like CD8$^+$ T cells (**D**) and other CD8$^+$ T cells (**E**). Genes modulated only in *E.clostridioformis*-treated mice are depicted on the right side of each Venn diagram respectively. Genes upregulated or downregulated in *E. clostridioformis*-treated mice are depicted in orange and blue, respectively. A representative experiment out of two is depicted.

Figure S9

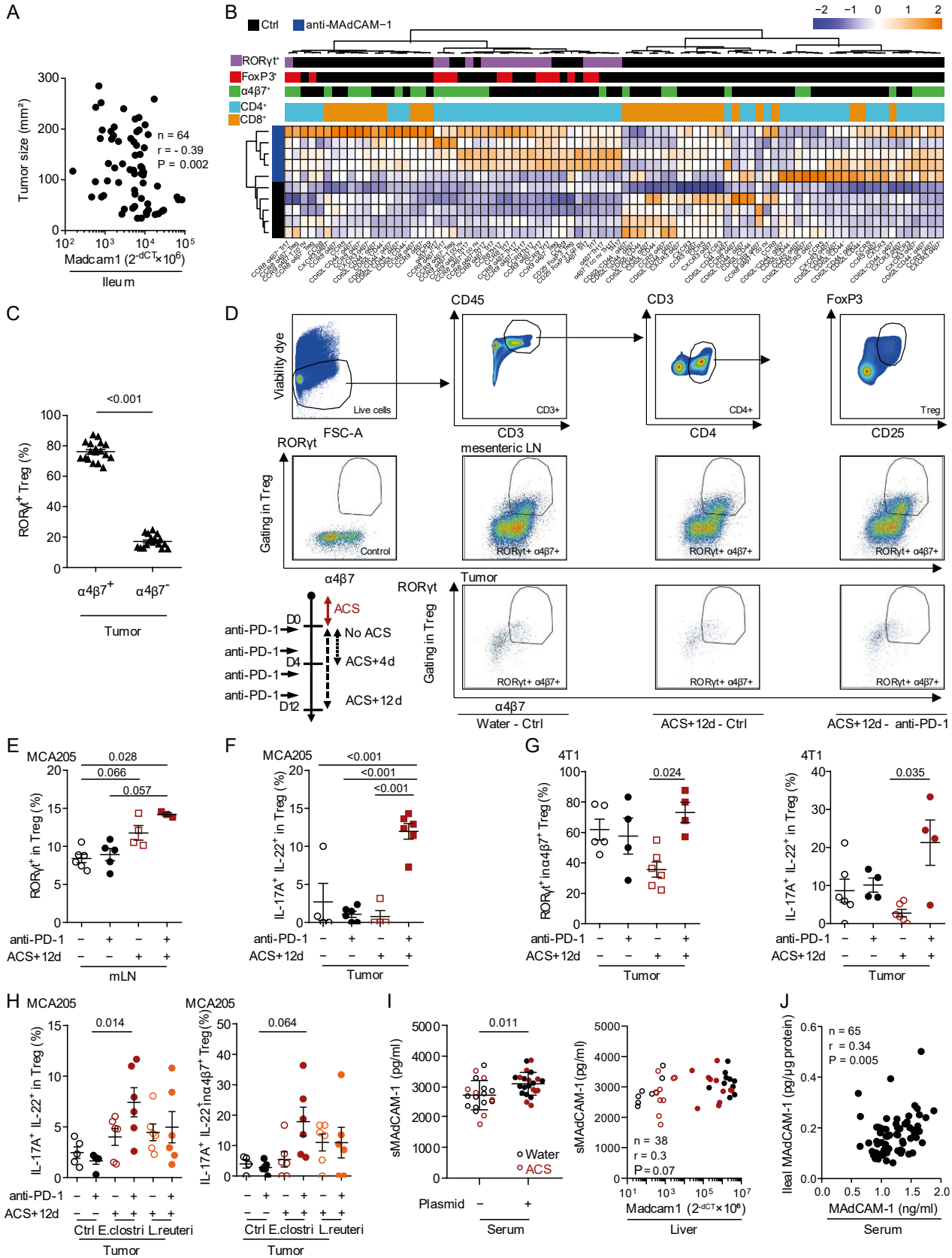
A
Tumor size (mm²)
n = 64
r = - 0.39
P = 0.002
Madcam1 (2^-dCT×10^6)
Ileum
B
Ctrl
anti-MAdCAM-1
RORγt⁺
FoxP3⁺
α4β7⁺
CD4⁺
CD8⁺
C
<0.001
RORγt⁺ Treg (%)
α4β7⁺
α4β7⁻
Tumor
D
Viability dye
Live cells
FSC-A
CD45
CD3+
CD3
CD3
CD4+
CD4
FoxP3
Treg
CD25
RORγt
mesenteric LN
Gating in Treg
Control
RORγt+ α4β7+
α4β7
ACS
D0
anti-PD-1
No ACS
D4
ACS+4d
D12
ACS+12d
Tumor
Water - Ctrl
ACS+12d - Ctrl
ACS+12d - anti-PD-1
E
MCA205
0.028
0.066
0.057
RORγt⁺ in Treg (%)
anti-PD-1
ACS+12d
mLN
F
MCA205
<0.001
<0.001
<0.001
IL-17A⁺ IL-22⁺ in Treg (%)
Tumor
G
4T1
0.024
RORγt⁺ in α4β7⁺ Treg (%)
0.035
H
MCA205
0.014
0.064
Ctrl
E.clostri
L.reuteri
I
0.011
sMAdCAM-1 (pg/ml)
Water
ACS
Plasmid
Serum
n = 38
r = 0.3
P = 0.07
Madcam1 (2^-dCT×10^6)
Liver
J
n = 65
r = 0.34
P = 0.005
Ileal MAdCAM-1 (pg/μg protein)
MAdCAM-1 (ng/ml)
Serum

Fig. S9. Anti-PD-1 mAb aggravates the accumulation of enterotropic α4β7$^+$ Tr17 or IL-22$^+$ Tr17 cells towards tumor lesions caused by ACS-induced dysbiosis. (**A**) Spearman correlations between ileal *Madcam1* and tumor size in MCA205 tumor bearing and untreated mice, gathering the results from 11 experiments. Each dot represents one mouse. (**B**) Non supervised hierarchical clustering (Euclidean distance, ward linkage method) represented in a heatmap showing the relative percentages of various immune CD4$^+$ and CD8$^+$ T cell subsets (determined by flow cytometric analyses of TILs dissociated from established s.c. MCA205) in mice treated with neutralizing anti-MAdCAM-1 mAb or isotype control mAb in a representative experiment. (**C**) Flow cytometric assessment of α4β7$^+$ or α4β7$^-$ among RORγt$^+$ Treg (Tr17) TIL fractions in subcutaneous MCA205 tumors, pooling the data of three independent experiments of 6 mice per group. (**D**) Experimental setting and representative flow cytometry gating strategy of PD-1 blockade during ACS intervals of various durations (ACS+4d or +12d) in tumor bearers. (**E to G**) Flow cytometric assessment of RORγt$^+$ or IL-17A$^+$ IL-22$^+$ cells within Treg in the mLN (**E**) or in subcutaneous MCA205 (**F**) or 4T1 (**G**) tumors treated with anti-PD1 Abs in the setting of ACS. (**H**) Flow cytometric determination of IL-17A$^+$ IL-22$^+$ secreting Treg (**left**) and α4β7$^+$ Treg cells (**right**) in subcutaneous (s.c) MCA205 tumors treated by PD-1 blockade after ACS+12d stop and enforced gut colonization with *E. clostridioformis* or *L. reuteri* bacteria during anti-PD-1-based therapy. Each dot represents one animal at sacrifice, in a representative experiment containing six mice per group. Refer to table S4 for detailed phenotypes. (**I)** Serum sMAdCAM-1 concentrations (assessed by ELISA) at sacrifice (D14, ref to Figure 5A) after hydrodynamic intravenous inoculation of *Madcam1*-encoding cDNA subcloned into a pLIVE vector (**left panel**) in two independent and pooled experiments comprising 5-6 mice per group. Spearman correlation between serum sMAdCAM-1 and liver mRNA levels of *Madcam1* gene assessed by RT-qPCR (**right panel**). Each black or red dot representing one mouse conditioned with water or ACS, respectively. (**J**) Spearman correlation between ileal tissue lysate MAdCAM-1 concentrations (assessed by ELISA) and serum soluble MAdCAM-1 (ELISA) in 65 MCA205 tumor bearers treated or not with anti-PD-1 Abs, in 2 pooled experiments, each dot representing one mouse. Data information: Comparisons between groups were analyzed using nonparametric Mann–Whitney *U* test (2 groups) or Kruskal–Wallis *H* test (>2 groups) followed by multiple-comparisons test by controlling the FDR and nonparametric Spearman correlations were performed. For C, Wilcoxon matched-pairs signed rank test was performed. Error bars represent mean ± SEM.

Figure S10

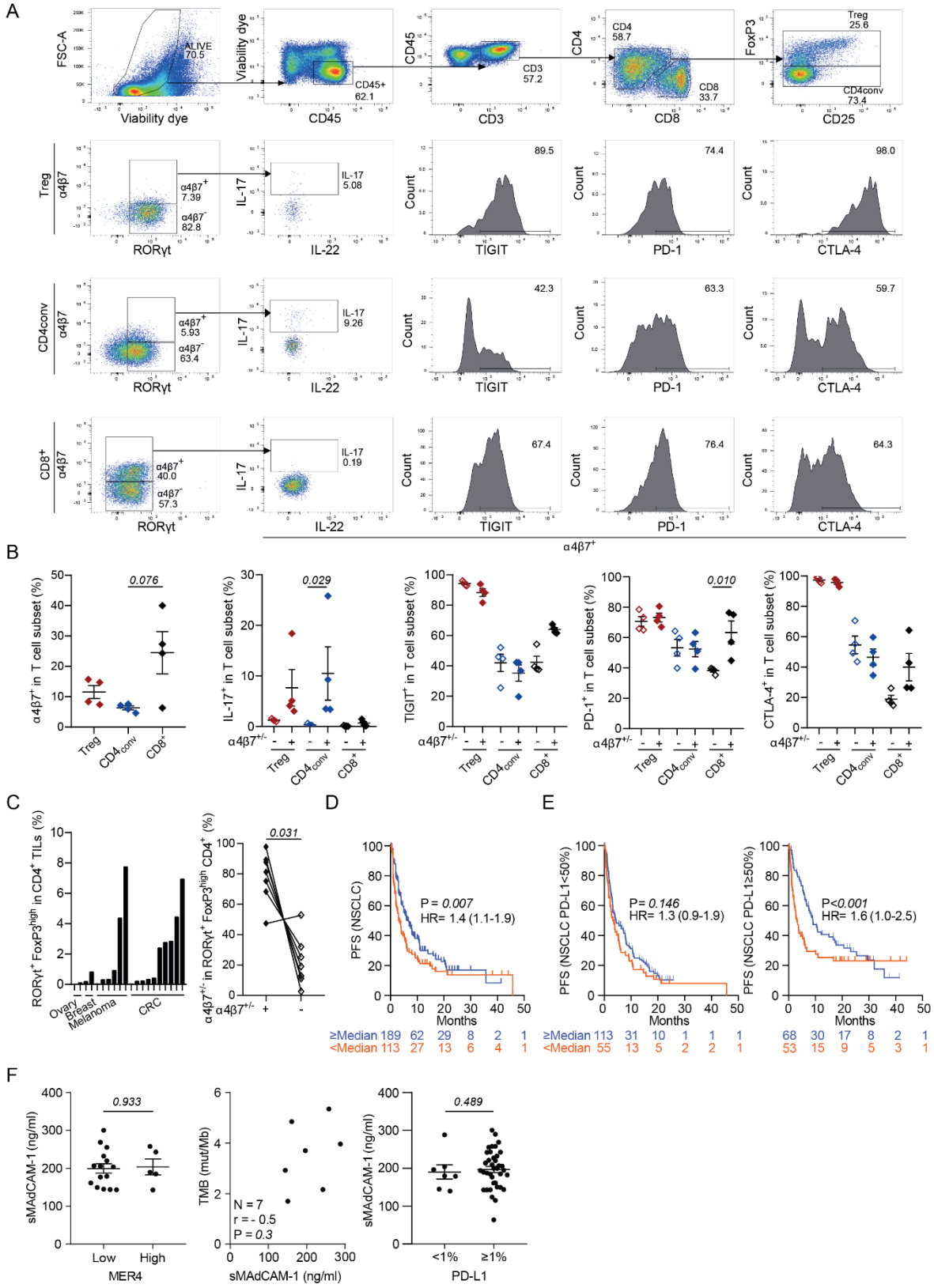
A
FSC-A
ALIVE 70.5
Viability dye
Viability dye
CD45+ 62.1
CD45
CD45
CD3 57.2
CD3
CD4
CD4 58.7
CD8 33.7
CD8
FoxP3
Treg 25.6
CD4conv 73.4
CD25
Treg
α4β7
α4β7+ 7.39
α4β7- 82.8
RORγt
IL-17
IL-17 5.08
IL-22
Count
89.5
TIGIT
74.4
PD-1
98.0
CTLA-4
CD4conv
α4β7+ 5.93
α4β7- 63.4
IL-17 9.26
42.3
63.3
59.7
CD8+
α4β7+ 40.0
α4β7- 57.3
IL-17 0.19
67.4
76.4
64.3
α4β7+
B
α4β7+ in T cell subset (%)
0.076
IL-17+ in T cell subset (%)
0.029
TIGIT+ in T cell subset (%)
PD-1+ in T cell subset (%)
0.010
CTLA-4+ in T cell subset (%)
α4β7+/-
Treg
CD4conv
CD8+
C
RORγt+ FoxP3high in CD4+ TILs (%)
Ovary
Breast
Melanoma
CRC
α4β7+/- in RORγt+ FoxP3high CD4+ (%)
0.031
D
PFS (NSCLC)
P = 0.007
HR= 1.4 (1.1-1.9)
Months
≥Median 189 62 29 8 2 1
<Median 113 27 13 6 4 1
E
PFS (NSCLC PD-L1<50%)
P= 0.146
HR= 1.3 (0.9-1.9)
≥Median 113 31 10 1 1 1
<Median 55 13 5 2 2 1
PFS (NSCLC PD-L1≥50%)
P<0.001
HR= 1.6 (1.0-2.5)
68 30 17 8 2 1
53 15 9 5 3 1
F
sMAdCAM-1 (ng/ml)
0.933
Low
High
MER4
TMB (mut/Mb)
N = 7
r = - 0.5
P = 0.3
sMAdCAM-1 (ng/ml)
0.489
<1%
≥1%
PD-L1

Fig. S10. Serum soluble MAdCAM-1 is an independent predictor of clinical benefit to PD-1 blockade. (**A to C**) Representative flow cytometric analyses of four fresh NSCLC tumor infiltrating lymphocytes (TIL) focusing of various T cell subsets expressing the integrin α4β7. A representative gating strategy is depicted (**A**). The activation/exhaustion markers are shown in percentages for each T cell subset for each tumor represented in one dot (**B**). Same analyses in 20 ex vivo propagated TIL cell lines from ovarian, breast, melanoma, and CRC patients. The graph (**C**) shows the percentages of $FoxP3^{hi}ROR\gamma t^{+}$ $CD4^{+}$ TILs in various cell lines (left panel) and their expression of α4β7 for each tumor with more than 2% of $FoxP3^{hi}ROR\gamma t^{+}$ (right panel). (**D and E**) Serum soluble MAdCAM-1 as a prognostic factor of progression-free survival (PFS) in the NSCLC discovery and validation cohorts, pooled together, treated with anti-PD-1/PD-L1 Abs, using Kaplan Meier estimator and Cox regression (**D**) and according to PD-L1 expression (**E**). Also refer to table S5 for patient description and S6 for multivariate analysis. (**F**) Serum levels of sMAdCAM-1 in NSCLC patients according to tumor expression of endogenous retrovirus MER4 (as determined by tumor RNA sequencing) (left panel). MER4 cut-off value was set up in a subset (n=20) of patients in the cohort from Centre George François Leclerc, Dijon, previously described (*64*). Spearman correlation between TMB and serum sMAdCAM-1 in 12 NSCLC patients (middle panel). Serum levels of sMAdCAM-1 in NSCLC patients according to their tumor expression of PD-L1 as determined by EMA-approved routine immunohistochemistry (right panel), the cut-off value being 1. Comparisons between groups were analyzed using the nonparametric Mann–Whitney *U* test (2 groups).

Antibiotics	Culturomic of ileum contents
ACS + 4d	*Enterobacter cloacae*
	Enterocloster bolteae
	Enterocloster clostridioformis
	Enterococcus faecalis
	Escherichia coli
	Hathewaya limosa
Streptomycin	*Cutibacterium acnes*
	Enterococcus faecalis
Erythromycin	*Enterobacter cloacae*
	Enterocloster clostridioformis
	Escherichia coli
	Klebsiella pneumoniae
Colistin	*Enterobacter cloacae*
	Enterococcus faecalis
	Ligilactobacillus murinus
	Staphylococcus xylosus
Ampicillin	*Enterobacter cloacae*
	Enterococcus faecalis
	Escherichia coli
Vancomycin	*Enterobacter cloacae*
	Enterococcus faecalis
	Escherichia coli
	Ligilactobacillus murinus
	Limosilactobacillus reuteri

Table S1. Ileal microbiota recolonization post –antibiotics.

Category	Age	Gender	Primary diagnosis	ABX characteristics	Ileum	Caecum	Colon
No ABX	32	Female	Colorectal cancer screening	−	+	+	+
No ABX	64	Female	Elective polypectomy	−	+	+	+
No ABX	79	Female	Diverticular bleeding	−	+	+	+
No ABX	37	Male	Colorectal cancer screening	−	+	+	+
No ABX	48	Male	Colorectal cancer screening	−	+	+	−
No ABX	71	Male	Colorectal cancer screening	−	+	+	+
No ABX	71	Male	Colorectal cancer screening	−	+	−	+
No ABX	20	Male	Irritable bowel syndrome	−	+	+	+
No ABX	59	Male	Liver metastases	−	+	+	+
No ABX	18	Male	Abdominal lymphoma	−	+	+	+
No ABX	76	Male	Hepatic metastases	−	+	+	+
No ABX	77	Male	Hepatic metastases	−	+	+	+
No ABX	56	Female	Endometrial cancer	−	+	+	+
No ABX	52	Male	Hepatic metastases	−	+	+	+
No ABX	45	Female	Colorectal cancer screening	−	+	+	+
No ABX	41	Male	Colorectal cancer screening	−	+	+	+
No ABX	36	Male	Colorectal cancer screening	−	+	+	+
No ABX	42	Male	Colorectal cancer screening	−	+	+	+
No ABX	36	Male	Colorectal cancer screening	−	+	+	+
No ABX	43	Female	Colorectal cancer screening	−	+	+	+
No ABX	58	Male	Elective polypectomy	−	+	+	+
ABX	36	Female	Diarrhea	Cefazolin plus metronidazole for 6 weeks; stopped 2 weeks prior	+	+	+
ABX	64	Female	Hepatic metastases	Active ceftriaxone plus metronidazole or 1 week	+	+	+
ABX	81	Female	Control after endoscopic mucosa resection	Cefuroxime plus metronidazole; 2 months prior	+	+	+
ABX	76	Male	Colorectal carcinoma	Active Ceftriaxone for 3 days	+	+	+
ABX	47	Female	Colorectal cancer screening	Active fosfomycine for 3 days	+	+	+
ABX	71	Male	Recurrent gastrointestinal bleeding	Active ceftriaxone for 5 days	+	+	+
ABX	78	Male	Hepatic metasdtases	Active piperacilline	+	+	+
ABX	61	Male	Colorectal cancer screening	Ampicillin for 7 days until 2 weeks prior	+	+	−
ABX	31	Female	Colorectal cancer screening	Ciprofloxacine for 5 days until 2 weeks prior	+	+	+
ABX	87	Male	Hepatic metastases	Active amoxicilline for 5 days	+	+	+

ABX : Antibiotics

Table S2. Description of patients who took ABX before endoscopy.

Patient	FMT	Age	Gender	ECOG PS	Smoking	Histology	Stage	Previous treatment	Treatment	Best_response	Overall survival	ABX before sampling	PD-L1	TMB (mut/Mb)
1	A	72	Male	2	Former	Non squamous	IV	1L Chemotherapy	Immunotherapy	Progressive disease	<12 months	No	<50	Unknown
2	B	45	Male	0	Former	Non squamous	IV	1L Chemotherapy	Immunotherapy	Partial response	≥12 months	No	<50	Unknown
3	C	68	Male	0	Current	Squamous cell	IV	1L Chemotherapy	Immunotherapy	Partial response	≥12 months	No	≥50	0,07
4	D	71	Male	1	Current	Squamous cell	IV	1L Chemotherapy	Immunotherapy	Progressive disease	<12 months	No	<50	Unknown
5	E	58	Male	2	Current	Non squamous	IV	1L Chemotherapy	Immunotherapy	Progressive disease	<12 months	No	Unknown	Unknown
6	F	60	Male	0	Current	Non squamous	IV	1L Chemotherapy	Immunotherapy	Progressive disease	≥12 months	No	<50	Unknown

1L: 1st line

Table S3. Description of patients donating the FMT.

Group	Water		ACS + 12d			ACS + 12d + αPD-1			
					vs Water			vs Water	vs ACS + 12d
Population	N	Mean±SEM (%)	N	Mean±SEM (%)	P-value	N	Mean±SEM (%)	P-value	P-value
α4β7$^+$ CD4$^+$ in CD3$^+$	44	2.2 ± 0.3	21	1.8 ± 0.3	*0.693*	19	1.7 ± 0.3	*0.349*	*0.660*
α4β7$^+$ in CD4$^+$	44	18.9 ± 1.4	21	22.0 ± 1.8	***0.055***	19	24.2 ± 2.2	***0.022***	*0.704*
Treg in α4β7$^+$ CD4$^+$	44	11.7 ± 1.6	21	13.7 + 1.6	*0.321*	19	19.1 ± 2.8	***0.028***	*0.280*
RORγt$^+$ in α4β7$^+$ Treg	44	44.5 ± 5.3	20	34.5 ± 6.8	*0.280*	19	51.1 ± 7.7	*0.389*	*0.099*
IL-17A$^+$ in α4β7$^+$ Tr17	39	33.4 ± 5.1	16	59.0 ± 7.4	***0.008***	19	61.3 ± 7.0	***0.008***	*0.877*

Treg : CD25$^+$ FoxP3$^+$

Tr17: RORγt$^+$ Treg

Table S4. Deconvolution of enterotropic Tr17 subset proportions invading MCA205 and 4T1 tumors.

		NSCLC											RCC				BC			
		Discovery (n=115)	<Median (n=57)	>Median (n=58)	P-value	Validation (n=187)	<Median (n=93)	>Median (n=94)	P-value	Validation2 (n=45)	<Median (n=22)	>Median (n=23)	P-value	All (n=212)	<Median (n=106)	>Median (n=106)	P-value	All (n=79)	<Median (n=39)	>Median (n=40)	P-value
	Median (range)	66 (39-93)	66 (39-93)	65 (39-82)	*0.550 (continuous)*	64 (32-87)	64 (36-87)	64 (32-86)	*0.986*	65 (36-84)	67 (36-84)	63 (39-84)	*0.243*	64 (22-87)	66 (22-87)	61 (31-87)		67 (44-88)	67 (48-84)	67 (44-88)	*0.308*
Age (year)	**<65 yr**	47 (41)	22 (38)	25 (38)		88 (47)	42 (45)	46 (49)		22 (49)	9 (41)	13 (57)		110 (52)	49 (46)	61 (58)		31 (39)	16 (41)	15 (38)	
	≥65 to <75 yr	50 (43)	26 (46)	24 (41)	*0.875*	70 (37)	37 (40)	33 (35)	*0.802*	18 (40)	9 (41)	9 (39)	*0.286*	73 (34)	41 (39)	32 (30)	*0.255*	35 (44)	17 (44)	18 (45)	*0.939*
	≥75 yr	18 (16)	9 (16)	9 (15)		29 (26)	14 (15)	15 (16)		5 (11)	4 (18)	1 (4)		29 (14)	16 (15)	13 (12)		13 (17)	6 (15)	7 (17)	
Sex – no (%)	**Male**	61 (53)	36 (63)	25 (43)	*0.03*	115 (29)	61 (66)	54 (56)	*0.16*	31 (69)	16 (73)	15 (65)	*0.749*	174 (82)	89 (84)	85 (80)	*0.591*	67 (85)	34 (87)	33 (83)	*0.755*
	Female	54 (47)	21 (36)	33 (57)		72 (38)	32 (34)	40 (44)		14 (31)	6 (27)	8 (35)		38 (18)	17 (16)	21 (20)		12 (15)	5 (13)	7 (17)	
BMI, kg/cm^2 – no (%)	**<25**	58 (56)	30 (61)	28 (52)	*0.108*	108 (60)	54 (61)	54 (59)	*0.347*	27 (64)	18 (86)	9 (43)	*0.013*	91 (44)	51 (50)	40 (39)	*0.203*	36 (50)	21 (60)	15 (41)	*0.056*
	[25-30[	31 (30)	16 (33)	15 (28)		55 (30)	29 (33)	26 (28)		13 (31)	3 (14)	10 (48)		78 (38)	33 (32)	45 (43)		22 (31)	6 (17)	16 (43)	
	≥30	14 (14)	3 (6)	11 (20)		18 (10)	6 (6)	12 (13)		2 (5)	–	2 (9)		37 (18)	18 (18)	19 (18)		14 (19)	8 (23)	6 (16)	
	Unknown	12	8	4		6	4	2		3	1	2		6	4	2		7	4	3	
ECOG-PS – no (%)	**0-1**	96 (83)	46 (81)	50 (86)	*0.423*	132 (71)	56 (61)	76 (81)	*0.003*	35 (80)	15 (71)	20 (87)	*0.272*	115 (55)	80 (80)	96 (96)	*0.001*	70 (89)	35 (90)	35 (88)	*0.999*
	2 or more	19 (17)	11 (19)	8 (14)		54 (29)	36 (39)	18 (19)		9 (20)	6 (29)	3 (13)		96 (45)	20 (20)	4 (4)		9 (11)	4 (10)	5 (12)	
	Unknown	–	–	–		1	1	–		1	1	–		1	6	6		–	–	–	
Smoking status — no. (%)	**Never smoked**	8 (7)	3 (5)	5 (9)	*0.48*	11 (6)	8 (9)	3 (3)	*0.12*	3 (7)	1 (5)	2 (9)	*0.999*	–	–	–		17 (22)	4 (10)	5 (12)	*0.999*
	Current/former smoker	107 (93)	54 (95)	53 (91)		174 (94)	84 (91)	90 (97)		39 (93)	19 (95)	20 (91)		–	–	–		62 (78)	35 (90)	35 (88)	
	Unknown					2	1	1		3	2	1		–	–	–		–	–	–	
Tumor histology — no. (%)	**Squamous**	23 (20)	12 (21)	11 (19)	*0.781*	44 (24)	25 (27)	19 (20)	*0.302*	4 (9)	2 (9)	2 (9)	*0.999*	–	–	–		–	–	–	
	Non-squamous	92 (80)	45 (79)	47 (81)		142 (76)	67 (73)	75 (80)		39 (91)	19 (91)	20 (91)		–	–	–		–	–	–	
	Unknown	–	–	–		1	1	–	–	2	1	1		–	–	–		–	–	–	
	Clear cell RCC	–	–	–		–	–	–	–	–	–	–	–	212 (100)	106 (100)	106 (100)		–	–	–	
	UC (transitional cell)	–	–	–		–	–	–	–	–	–	–	–	–	–	–		76 (97)	39 (100)	37 (94)	
	Papillary UC	–	–	–		–	–	–	–	–	–	–	–	–	–	–		1 (1)	–	1 (2)	
	Mixed cell type	–	–	–		–	–	–	–	–	–	–	–	–	–	–		1 (1)	–	1 (2)	
	Undifferentiated carcinoma	–	–	–		–	–	–	–	–	–	–	–	–	–	–		1 (1)	–	1 (2)	
PD-L1 status — no. (%)	**<1%**	29 (25)	16 (31)	13 (23)	*0.39*	55 (30)	25 (28)	30 (33)	*0.013*	7 (15)	4 (18)	3 (13)	*0.737*	88 (81)	37 (80)	51 (81)	*0.001*	–	–	–	
	1–49%	29 (25)	11 (21)	18 (32)		55 (30)	21 (23)	34 (38)		17 (38)	9 (41)	8 (35)		17 (16)	7 (15)	10 (16)		–	–	–	
	≥50%	50 (50)	25 (48)	25 (45)		71 (40)	45 (49)	26 (29)		21 (47)	9 (41)	12 (52)		4 (4)	2 (4)	2 (3)		–	–	–	
	Unknown	7	5	2		6	2	4		–	–	–		103	60	43		–	–	–	
IMDC — no. (%)	**Good**	–	–	–		–	–	–		–	–	–		39 (19)	12 (11)	27 (26)		–	–	–	
	Intermediate	–	–	–		–	–	–		–	–	–		123 (58)	57 (54)	66 (63)		–	–	–	
	Poor	–	–	–		–	–	–		–	–	–		49 (23)	37 (35)	12 (11)		–	–	–	
	Unknown	–	–	–		–	–	–		–	–	–		1	0	1		–	–	–	
PD-L1 status — no. (%)	**< 25%**	–	–	–		–	–	–		–	–	–		–	–	–		34 (60)	19 (65)	15 (54)	
	≥ 25%	–	–	–		–	–	–		–	–	–		–	–	–		23 (40)	10 (35)	13 (46)	*0.424*
	Unknown	–	–	–		–	–	–		–	–	–						22	10	12	
Therapy line — no. (%)	**Neoadjuvant / adjuvant**									–	–	–		0 (0)	0 (0)	0 (0)		–	–	–	
	First line					100 (53)	42 (45)	58 (62)	*0.028*	23 (51)	11 (50)	11 (48)		0 (0)	0 (0)	0 (0)		–	–	–	
	≥ Second line					87 (47)	51 (55)	36 (38)		22 (49)	11 (50)	12 (52)		212 (100)	106 (100)	106 (100)		79 (100)	39 (100)	40 (100)	
Current therapy — no. (%)	**Immunotherapy**	86 (75)	48 (84)	38 (65)	*0.02*	122 (65)	67 (73)	55 (58)	*0.04*	45 (100)	22 (100)	23 (100)		212 (100)	106 (100)	106 (100)		79 (100)	39 (100)	40 (100)	
	Immunotherapy and Chemotherapy	29 (25)	9 (16)	20 (35)		64 (45)	25 (27)	39 (42)		–	–	–		–	–	–		–	–	–	
	Unknown					1	1	–		–	–	–		–	–	–		–	–	–	
Previous therapy — no. (%)	**Chemotherapy**	35 (33)	20 (41)	15 (26)						–	–	–		–	–	–		79 (100)	39 (100)	40 (100)	
	VEGF/VEGFR inhibitors	–	–	–						–	–	–		106 (100)	106 (100)	212 (100)		–	–	–	
	mTOR inhibitors	–	–	–						–	–	–		43 (20)	22 (21)	21 (20)		–	–	–	
	Cytokines	–	–	–						–	–	–		8 (4)	4 (4)	4 (4)					
	Others	–	–	–						–	–	–		13 (6)	4 (4)	9 (9)		–	–	–	
	Unknown	8	8	–						45	22	23		–	–	–		–	–	–	
Antibiotics — no. (%)	**Yes**	21 (18)	14 (25)	7 (12)	*0.08*	22 (12)	17 (19)	5 (5)	*0.005*	–	–	–		31 (15)	17 (16)	14 (14)	*0.7*	5 (6)	1 (3)	4 (11)	*0.2*
	No	94 (82)	43 (75)	51 (82)		162 (88)	74 (81)	88 (95)		–	–	–		176 (85)	89 (84)	87 (86)		72 (94)	38 (97)	34 (89)	
	Unknown	–	–	–		3	2	1		45	22	23		5	0	5		2	–	2	
Antibiotics' class — no. (%)	**β- lactams ± inhibitors**	7 (33)	5 (39)	2 (29)		–	–	–		–	–	–		18 (58)	8 (47)	10 (71)		1 (25)	0 (0)	1 (33)	
	Cephalosporins	3 (14)	2 (14)	1 (14)		–	–	–		–	–	–		5 (16)	4 (24)	1 (7)		2 (50)	0 (0)	2 (67)	
	Fluoroquinolones	2 (9)	2 (14)	–		–	–	–		–	–	–		8 (26)	4 (24)	4 (29)		1 (25)	1 (100)	0 (0)	
	Quinolones	3 (14)	–	2 (29)		–	–	–		–	–	–		1 (3)	1 (6)	0 (0)		0 (0)	0 (0)	0 (0)	
	Nitroimidazoles	1 (5)	1 (7)	–		–	–	–		–	–	–		3 (10)	1 (6)	2 (14)		0 (0)	0 (0)	0 (0)	
	Macrolides	2 (9)	1 (7)	1 (14)		–	–	–		–	–	–		1 (3)	1 (6)	0 (0)		0 (0)	0 (0)	0 (0)	
	Others	5 (24)	4 (29)	1 (14)		–	–	–		–	–	–		3 (10)	2 (12)	1 (7)		0 (0)	0 (0)	0 (0)	
	Unknown	–	–	–		–	–	–		–	–	–		–	–	–		1	0	1	

RCC: Renal Cell Carcinoma, BC: Bladder Cancer, IMDC: International Metastatic Database Consortium risk model for metastatic renal cell carcinoma, NSCLC: non small cell lung cancer

Table S5. Patient characteristics.

Variable		No. of patients	HR (95% CI)	P-value
Age		347	0.99 (0.98-1.01)	*0.434*
Gender				
	Female	140	reference	
	Male	207	0.98 (0.70-1.38)	*0.9*
PD-L1 status				
	<1%	92	reference	
	1-49%	100	0.94 (0.61-1.45)	*0.787*
	≥50%	142	0.63 (0.41-0.96)	*0.033*
ECOG-PS				
	0	93	reference	
	1	170	1.61 (1.04-2.51)	*0.033*
	≥2	82	2.72 (1.65-4.50)	*<0.001*
Therapy line				
	1st	187	reference	
	≥2nd	124	1.59 (1.13-2.23)	*0.008*
Previous ABX				
	No	256	reference	
	Yes	43	1.56 (0.96-2.53)	*0.07*
sMAdCAM-1				
	< Median	127	reference	
	≥ Median	220	0.69 (0.49-0.97)	*0.035*

HR: Hazard ratios; CI: Confidence interval;
ECOG-PS: ECOG performance status; ABX: antibiotics

Events: 144; Global P-value (Log-Rank): 3.7559e-06
AIC: 1395.8; Concordance Index: 0.66

Table S6. Hazard ratios of the multivariable Cox model for the Overall survival (OS) analysis of the pooled Discovery and Validation NSCLC cohorts.

Age-yr (%)	<65	38 (40)
	≥65	57 (60)
Gender (%)	Male	49 (52)
	Female	46 (48)
Histology (%)	Squamous	12 (13)
	Non-squamous	54 (57)
	Unknown	29 (31)
ECOG performance status (%)	0-1	81 (85)
	≥2	14 (15)
Stage (%)	II-III	14 (15)
	IV	81 (85)
Line (%)	1	60 (63)
	≥2	35 (37)
Antibiotics use (%)	No	84 (88)
	Yes	11 (12)
Overall-survival (%)	<12	39 (41)
	≥12	39 (41)
	Unknown	17 (18)

Table S7. NSCLC cohort description for MG investigations.

Antibody	Clone	RRID	Source	Concentration (per million cells in 100 µl)
CD3ε	145-2C11	AB_2629687	BioLegend	1µl
CD3ε	145-2C11	AB_893317	BioLegend	1µl
CD4	RM4-5	AB_493374	BioLegend	1µl
CD4	RM4-5	AB_312729	BioLegend	1µl
CD8α	53-6.7	AB_2564027	BioLegend	0.5µl
CD25	PC61	AB_2563060	BioLegend	1µl
CD44	IM7	AB_493713	BioLegend	1µl
CD45	30-F11	AB_893339	BioLegend	1µl
CD45	30-F11	AB_493715	BioLegend	1µl
CD45	30-F11	AB_493535	BioLegend	1µl
CD62L	MEL-14	AB_313093	BioLegend	1µl
CD127	A7R34	AB_10897948	BioLegend	1µl
FoxP3	FJK-16s	AB_1210557	Thermofisher	1µl
RORγt	B2D	AB_2784671	Thermofisher	1µl
CXCR3	CXCR3-173/ S18001A	AB_2814078	BioLegend	1µl
CCR5	HM-CCR5/ REA354	AB_2801746	Miltenyi	2µl
CCR6	29-2L17	AB_2562513	BioLegend	1µl
CCR9	CW-1.2	AB_2889490	Miltenyi	2µl
α4β7/LPAM-1	DATK32/ REA457	AB_2811331	Miltenyi	2µl
MAdCAM-1	MECA-367	AB_2629562	BioLegend	1µl
IL-17A	eBio17B7	AB_11220280	Thermofisher	1µl
IL-22	1H8PWSR	AB_10598646	Thermofisher	1µl
CD31	390	AB_830757	BioLegend	1µl
PNAd	MECA-79	AB_10804391	Thermofisher	1µl
CD62P	RB40.34	AB_2917917	BD	0.5µl
CD62E	10E9.6	AB_2742835	BD	0.5µl
CD64	X54-5/7.1	AB_2629778	BioLegend	1µl
CD19	6D5	AB_439718	BioLegend	1µl
F4/80	BM8	AB_893493	BioLegend	1µl

Table S8. List of antibodies used to stain murine cells.

Antibody	Clone	RRID	Source	Concentration (µl per 100µl)
CD8	SK1	AB_1645481	BD	1µl
TIGIT	741182	AB_2872307	BD	2µl
CD25	BC96	AB_2563807	BioLegend	1µl
PD1	EH12.1	AB_2738425	BD	1.5µl
CD3	UCHT1	AB_2744387	BD	1µl
CD4	SK3	AB_2870220	BD	1µl
CD45	HI30	AB_2870179	BD	1µl
FOXP3	PCH101	AB_1724125	Thermofisher	2µl
IL-17	eBio64DEC17	AB_10596502	Thermofisher	2.5µl
RORgt	AFKJS-9	AB_2848500	Thermofisher	2.5µl
IL-22	2G12A41	AB_2571931	BioLegend	2.5µl
CTLA4	BIN3	AB_396176	BD	2.5µl
α4β7/LPAM-1	Hu117	MAB10078R-100UG	R&D	2.5µl

Table S9. List of antibodies used to stain human cells.